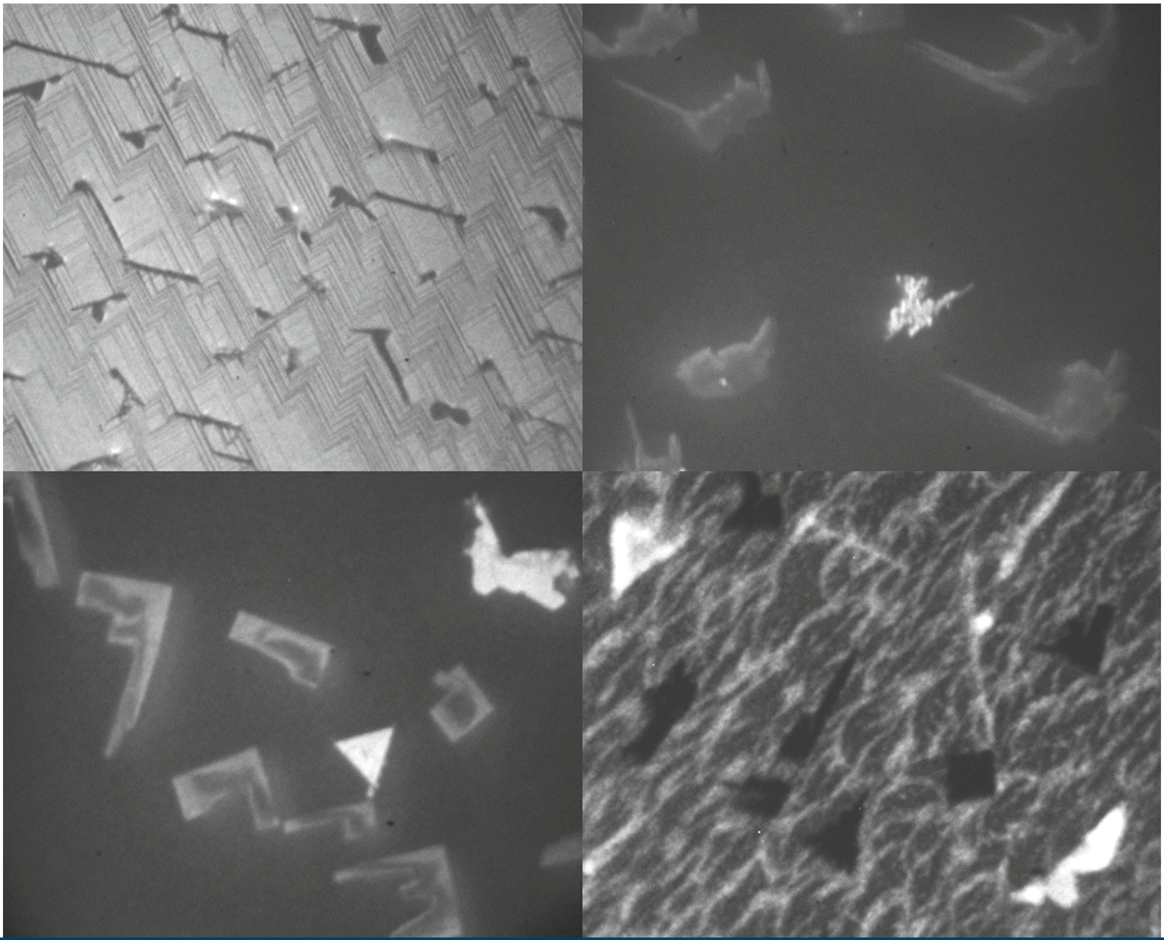

Reduction properties of a model ceria catalyst at the microscopic scale

Johanna Maria Hackl

Energie & Umwelt / Energy & Environment
Band / Volume 407
ISBN 978-3-95806-294-8

Mitglied der Helmholtz-Gemeinschaft

JÜLICH
Forschungszentrum

Schriften des Forschungszentrums Jülich
Reihe Energie & Umwelt / Energy & Environment Band / Volume 407

Forschungszentrum Jülich GmbH
Peter Grünberg Institut (PGI)
Elektronische Eigenschaften (PGI-6)

Reduction properties of a model ceria catalyst at the microscopic scale

Johanna Maria Hackl

Schriften des Forschungszentrums Jülich
Reihe Energie & Umwelt / Energy & Environment Band / Volume 407

ISSN 1866-1793 ISBN 978-3-95806-294-8

Bibliografische Information der Deutschen Nationalbibliothek.
Die Deutsche Nationalbibliothek verzeichnet diese Publikation in der
Deutschen Nationalbibliografie; detaillierte Bibliografische Daten
sind im Internet über http://dnb.d-nb.de abrufbar.

Herausgeber und Vertrieb: Forschungszentrum Jülich GmbH
Zentralbibliothek, Verlag
52425 Jülich
Tel.: +49 2461 61-5368
Fax: +49 2461 61-6103
zb-publikation@fz-juelich.de
www.fz-juelich.de/zb

Umschlaggestaltung: Grafische Medien, Forschungszentrum Jülich GmbH

Druck: Grafische Medien, Forschungszentrum Jülich GmbH

Copyright: Forschungszentrum Jülich 2018

Schriften des Forschungszentrums Jülich
Reihe Energie & Umwelt / Energy & Environment, Band / Volume 407

D 464 (Diss., Duisburg, Univ., 2017)

ISSN 1866-1793
ISBN 978-3-95806-294-8

Vollständig frei verfügbar über das Publikationsportal des Forschungszentrums Jülich (JuSER)
unter www.fz-juelich.de/zb/openaccess.

This is an Open Access publication distributed under the terms of the Creative Commons Attribution License 4.0,
which permits unrestricted use, distribution, and reproduction in any medium, provided the original work is properly cited.

Zusammenfassung

Ceroxid ist ein Seltenerdoxid mit vielfältigen katalytischen Eigenschaften, die für viele industrielle Anwendungen genutzt werden. Das katalytische Verhalten von Ceroxid basiert auf seiner Fähigkeit, Sauerstoff aufzunehmen und wieder freizusetzen, indem es seinen Oxidationszustand reversibel zwischen Ce^{4+} und Ce^{3+} wechselt. Das Thema dieser Dissertation ist die Untersuchung epitaktischer, mikroskopischer, wenige Monolagen dicker Ceroxidinseln mit (111) und (100) Terminierungen der Kristalloberflächen, präpariert auf Kupfereinkristallen. Diese Ceroxidinseln dienen als Modellsystem für katalytische Oxidations- und Reduktionsreaktionen. Die Entstehung von CeO_2 Inseln beider Oberflächenorientierungen und deren unterschiedliches Reduktionsverhalten wurden gleichzeitig, in-situ und in Echtzeit sowie unter identischen Bedingungen mit niederenergetischer Elektronenmikroskopie und Photoemissionsmikroskopie beobachtet.

Experimente zum Reduktionsverhalten von CeO_2 (111) und (100) orientierten Inseln wurden mit zwei verschieden Vorgehensweisen durchgeführt: Die Reduktion in einer Wasserstoffatmosphäre und die Reduktion durch Deposition von metallischem Cer auf die ursprünglich präparierten Inseln. Dabei stellte sich heraus, dass in beiden Fällen die (100) orientierten Inseln stärker reduziert wurden als die (111) Inseln. Die Analyse der Reduktionskinetik für die Ceroxidreduktion in Wasserstoff zeigte eine insgesamt höhere Reduzierbarkeit der (100) terminierten Ceroxidoberfläche. Diese höhere Reduzierbarkeit wird nicht durch einen Unterschied in der Kinetik für die zwei Oberflächenterminierungen sondern durch einen Unterschied in der Thermodynamik verursacht. Dies zeigt, dass die Oberflächenorientierung von Ceroxid einen starken Einfluss auf seine katalytischen Eigenschaften hat, was mit Vorhersagen durch Berechnungen mittels Dichtefunktionaltheorie übereinstimmt.

Ein Reduktionsexperiment in Wasserstoffatmosphäre wurde ebenfalls für eine Kombination aus Platin und Ceroxid, die durch die Deposition von Platin auf CeO_2 (111) und (100) Inseln hergestellt wurde, durchgeführt. Die beobachtete Entstehung stark reduzierter Ceroxidstrukturen an den Rändern der ursprünglichen Inseln ist ein Hinweis auf die Mischung von Platin und Ceroxid und die Bildung von katalytisch aktiven Zentren in diesen Strukturen. Für die (100) Inseln wurde die Bildung der stark reduzierten Strukturen in höherem Ausmaß beobachtet, was erneut das unterschiedliche Verhalten dieser beiden Oberflächenorientierungen von Ceroxid zeigt.

Abstract

Cerium oxide is a rare earth metal oxide with versatile catalytic properties used for many industrial applications. The catalytic behavior of cerium oxide is based on its ability to store and release oxygen by reversibly changing its oxidation state between Ce^{4+} and Ce^{3+}. The topic of this thesis is the examination of epitaxial, micrometer-sized, a few monolayers thick cerium oxide islands with (111) and (100) crystal surface terminations, prepared on copper single crystalline substrates. These cerium oxide islands serve as model systems for catalytic oxidation and reduction reactions. The formation of CeO_2 islands of both surface orientations and their different reduction behaviors were observed simultaneously, in-situ, in real-time and under identical conditions with low energy and photoemission electron microscopy and X-ray absorption spectroscopy.

Experiments on the reduction behavior of CeO_2 (111) and (100) oriented islands were performed using two different approaches: the reduction in a hydrogen atmosphere and the reduction by deposition of metallic cerium in vacuum on top of the originally prepared islands. It was found that the (100) oriented islands became more reduced than the (111) islands in both cases. Analyzing the reduction kinetics of the cerium oxide reduction in hydrogen showed an overall higher reducibillity of the (100) terminated cerium oxide surface, which is not caused by a difference in kinetics between the two surface terminations but by a difference in thermodynamics. This demonstrates that the surface orientation of cerium oxide has a strong effect on its catalytic properties, which is in agreement with predictions by density functional theory calculations.

A reduction experiment in hydrogen atmosphere was also performed on a platinum/cerium oxide system, which was prepared by the deposition of Pt on top of CeO_2 (111) and (100) islands. The observed formation of highly reduced cerium oxide structures decorating the original islands indicated a mixture of platinum and cerium oxide and the formation of active centers for catalysis in these areas. For the (100) islands, the formation of the highly reduced structures was observed to a greater degree, again showing a behavioral difference between the two cerium oxide surface orientations.

Contents

Introduction

The global, continuously increasing demand for energy combined with the limited resources of fossil energy carriers and climate change are one of the largest technological and societal challenges of the present time and the near future. For this reason extensive efforts have been made to advance the use of renewable energy sources, such as wind and solar power. However, the amount of electrical energy generated by these means is subject to fluctuations depending on weather conditions and the time of the day. Even if the capacities are established to theoretically replace fossil energy carriers by renewable energy sources, these fluctuations can make renewable energy unavailable for extended stretches of time. Therefore, technologies for energy storage are an essential requirement to guarantee a stable energy supply. One option is to store electrical energy in batteries. Another option is to store energy in the form of hydrogen, which can be produced by water splitting or the water-gas shift reaction. The hydrogen can be used directly in fuel cells or be bound in hydrocarbons to produce synthetic fuels. In this case, chemical reactions convert hydrogen and carbon from carbon monoxide or carbon dioxide to liquid hydrocarbons or alcohols [1, 2]. The high energy density of synthetic fuels is a key advantage for mobile and transport applications. Moreover, the existing infrastructures are already adapted to hydrocarbon based fuels, which makes the technological transition easier.

The energy efficiency of these reactions, and thereby the efficiency of the energy storage mechanism, can be substantially increased by catalysts. The function of catalysts is to reduce the energy barriers between different transition states during chemical reactions and by this they increase the reaction rates and decrease the needed energy input [3]. These catalytic functions are not only needed for the production of hydrogen and synthetic fuels, but are just as relevant for products of the chemical industry in general. Heterogeneous catalytic reactions, where the reactants and the catalysts are not in the same phase, are a crucial part of industrial chemistry [4]. Usually, the reactants are liquid or gaseous while the catalyst is a solid, with a combination of rare earth oxides and transition metals as a typical composition. The most prominent example is the use of cerium oxide together with noble metals in the three-way catalyst, which is used for the conversion of toxic automotive exhaust pollutants.

In order to selectively control the energy barrier of a reaction with a catalyst, all steps of the reaction and the exact function of the catalyst have to be known. The accurate description of active sites in heterogeneous catalysis is still a topic of extensive research, due to the vast complexity of industrially used catalysts. These are often powder-like crystalline nanoparticles with a multitude of different surface orientations and structural variations. This prevents the interpretation of individual structural features and makes it difficult to identify active sites on the catalyst, which are energetically favorable for the reactions. Simplified model systems are therefore used to reduce the systems complexity and examine a catalyst's function on a smaller scale. These model systems consist of only few elements and well defined surfaces, so that specific structural features can be isolated and analyzed experimentally [5].

The topic of this work is the examination of epitaxial, micrometer-sized, a few monolayers thin cerium oxide islands with (111) and (100) crystal surface terminations, prepared on copper single crystal substrates. These cerium oxide islands on copper substrates form crystalline and well ordered model systems, suitable for the investigation of the properties and behavior of their respective surface terminations. The thesis is structured as follows:

- Chapter 1 provides an introduction to the properties of cerium oxide, foremost its oxygen storage capacity, and several important industrial applications. The cerium dioxide crystal structure and its three low-index surface orientations (111), (110) and (100) terminations are described. The oxygen vacancy creation on these three surface terminations is discussed by comparing results of density functional theory calculations and experiments with nanoparticles available in the literature. The chapter finishes with an introduction of cerium oxide model catalysts.

- In chapter 2, the experimental setup and methods are presented. The descriptions include the design, functions and measurement modes of the used low energy and photoelectron emission microscope, the generation of synchrotron radiation and the methods used for sample preparation.

- The preparation of the copper crystal structures, the growth of cerium oxide islands with (111) and (100) surface orientations and their characterization are described in chapter 3.

- Observations of the reduction of (111) and (100) terminated cerium oxide islands on a copper (111) substrate in a hydrogen atmosphere are shown in chapter 4. This is followed by a comparison of the reduction levels, the reduction kinetics and the energetics of the two surface terminations.

- The reduction of similar cerium oxide (111) and (100) islands on copper (111) by deposition of metallic cerium on top is presented as an alternative reduction experiment in chapter 5.

- Chapter 6 is about the deposition of Pt onto cerium oxide (111) and (100) islands, and the reduction of these combined structures in a hydrogen atmosphere.

- The topic of chapter 7 is the effect of crystal defects of the copper substrates on the cerium oxide growth. Copper crystal defects induce the growth of very distinctive cerium oxide structures, which are displayed and discussed.

The main objective of this work is a direct comparison of the (111) and (100) cerium oxide surface orientations in-situ, in real-time and under identical conditions. The methods of low energy and photoemission electron microscopy and X-ray absorption spectroscopy are utilized to observe the formation of cerium oxide islands of both surface terminations and their different reduction behavior. The cerium oxide islands serve as model systems to draw conclusions on the differences in kinetics and thermodynamics of the (111) and (100) terminations. The conclusions of this work help to expand the understanding of the effects, induced by employing different cerium oxide surfaces in catalytic applications.

1 Basic aspects

1.1 Cerium oxide

The rare earth element cerium in combination with oxygen has the common oxidation states of Ce^{4+} and Ce^{3+}, with the respective oxide compositions of CeO_2 and Ce_2O_3. Subject of this work are the oxidation and reduction of thin cerium oxide films with stoichiometries of CeO_{2-x} (with $0 \leq x \leq 0.5$) between these two compositions. The precise stoichiometry will be specified when necessary. In an oxygen atmosphere, CeO_2 crystallizes in the fluorite structure: a face-centred cubic unit cell (fcc), named after the mineral form of calcium fluoride [6]. This crystal structure and its low-index surfaces will be described in detail in section 1.3. The dioxide CeO_2 is also called ceria. Cerium oxide and cerium oxide-based mixed oxides have the ability to store and release oxygen by changing the formal oxidation state of cerium reversibly between Ce^{4+} and Ce^{3+} [6, 7]. Under oxygen deficient conditions, cerium oxide is reduced and releases oxygen while creating oxygen vacancies. Under oxygen rich conditions, oxygen vacancies are healed, the cerium oxide is reoxidized and thereby stores oxygen. This described mechanism is called oxygen storage capacity (OSC) and is essential for the wide use of cerium oxide in applications like three way catalysts, fuel cells and the production of hydrogen and hydrocarbons [8, 9].

1.2 Cerium oxide applications

There is a multitude of applications for cerium oxide and ceria-based materials. Here a few selected applications will be introduced. These are: Exhaust conversion, fuel cells and the water-gas shift reaction. Other well known applications not covered below include: Steam reforming, used to produce hydrogen and hydrocarbons, the oxidation of volatile organic compounds, dehalogenation, used for the oxidation of hydrogen chloride, hydrogenation of alkynes to olefins, photocatalysis and thermochemical water splitting.

1.2.1 Conversion of exhaust gases

Three way catalysts: The most widely used and established application of materials based on CeO_2 is in automotive three way catalysts (TWCs). TWCs convert pollutants resulting from the combustion of fuel in internal combustion engines. The function of the TWC is to convert all three main pollutants at the same time: The oxidation of carbon monoxide (CO) by $2\,CO + O_2 \rightarrow 2\,CO_2$, the oxidation of unburned hydrocarbons, for example methane (CH_4), by $CH_4 + 2\,O_2 \rightarrow CO_2 + 2\,H_2O$ and the reduction of nitrogen oxides (NO_x) by $2\,CO + 2\,NO \rightarrow 2\,CO_2 + N_2$ [10]. TWCs are usually built to consist of a monolithic support with a honeycomb structure. A coating of the catalytic material covers the inner surfaces of the channels in the honeycomb structure. The catalytic material is composed of a thermally stable support: generally doped Al_2O_3, noble metals as the active phase: Pt, Pd and Rh are commonly used, and a CeO_2-based promoter: mostly $Ce_xZr_{1-x}O_2$ [10]. The pollutants can only be converted efficiently in a narrow window of the air-to-fuel (A/F) ratio. Because the combustion fluctuates frequently, depending on the operating output power, the gas-phase expelled by the engine quickly changes between lean (high A/F ratio) and rich (low A/F ratio) conditions [8]. CeO_2 increases the operation range of the TWC by functioning as an oxygen buffer. Reduced cerium oxide CeO_{2-x} gathers oxygen by reducing NO_x, and CeO_2 provides oxygen for the CO and HC oxidation. The OSC of cerium oxide determines how far the operation window of the TWC can be expanded.

Catalyst for diesel engine exhaust gas conversion: In addition to CO, HC and NO_x, soot is a main pollutant in diesel engines. Ceria is one of the best suited materials for catalytic soot combustion [11]. The ceria catalysts are doped with Zr, La or Pr for thermal stability. There are two types of ceria catalyzed soot combustion: The active oxygen mechanism, where oxygen is directly transferred between ceria and the gas-phase oxygen, and the NO_2-assisted mechanism, where ceria catalyzes the oxidation of NO to NO_2 at higher temperatures. In the first case, highly reactive oxygen species are formed, which oxidize soot very efficiently. In the second case, NO_2, which is more oxidizing than O_2, induces the soot combustion. Ceria catalysts using the second mechanism are as effective or even more effective for soot combustion than Pt catalysts [11].

1.2.2 Fuel cells

Solid oxide fuel cells: Solid oxide fuel cells (SOFCs) contain three main components: An anode, where the fuel oxidation reaction takes place, a cathode, where the oxygen reduction reaction happens and an electrolyte between the anode and the cathode. Fig. 1.1 shows the working principle of an oxygen ion conductive SOFC (the other option is a proton conductive SOFC).

On the anode side, the input gas, consisting of H_2O and H_2, provides H_2 as fuel and at the output H_2O is expelled. On the cathode side, an input supplies O_2 in the form of air, while the output expels N_2. The H_2 molecules are dissociated at the anode by a catalyst, forming two protons and releasing two electrons. The electrons are transported to the anode surface, through the external circuit and to the cathode. O_2 molecules from the air are dissociated by a catalyst at the anode and form oxygen ions combined with electrons from the anode. The oxygen ions move to the cathode/electrolyte interface and into the electrolyte, they travel within the electrolyte to the anode/electrolyte interface and then further to the anode. At the anode the oxygen ions produce water with the protons in form of steam. Using a mixture of H_2O and H_2 as fuel, improves the spacial hydrogen distribution in the anode before the hydrogen oxidation reaction. The produced water vapor flows to the anode surface and diffuses into the exhaust gas. The electrical power generated in the cell is used via the external electrical circuit. Because of the migration resistances of the ions and electrons, heat is also produced. As result SOFCs generate power and heat [12].

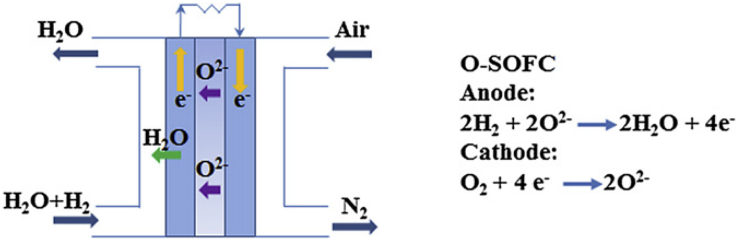

Fig. 1.1: Work schematic of oxygen ion conductive SOFC, from [12].

In SOFCs, ceria can generally be used in three ways: 1. Doped ceria can be used as an electrolyte, 2. When an yttria-stabilized zirconia (YSZ) electrolyte is used, CeO_2 can be a barrier to prevent interaction between the cathodes and the electrolyte, 3. Both for anodes and cathodes, CeO_2 can be added as a catalyst [8]. Ceria-based composites are used as electrolytes, because CeO_2 is ionically conductive and electronically insulating [13]. Common ceria dopants are Gd, Sm, Y, and Ca [12]. When doped ceria is used as an anode, doping with trivalent elements is a common way of performance improvement. For example, the cell performance is improved with a Gd-doped ceria anode, because the doping increases the oxygen vacancy concentration [14].

Proton exchange membrane fuel cells: In proton exchange membrane fuel cells (PEMFCs), ceria-based composites are used as well, but not as commonly as in the SOFCs. Ceria-based composites in connection with PEMFCs are mostly used in reforming processes to produce hydrogen, needed as fuel for PEMFCs [15]. In addition to that, the performance of Pt/C catalysts, used for the cathodes of PEMFCs, can be enhanced by a modification with CeO_2 [16].

1.2.3 Water-gas shift reaction

Hydrogen can be produced from carbon monoxide and water by the water-gas-shift reaction (WGSR): $CO + H_2O \rightarrow H_2 + CO_2$ [17]. The WGS is an essential industrial reaction needed for processes like the Fischer-Tropsch synthesis, methanol synthesis, or hydroformylation, to balance the $H_2/CO/CO_2$ ratios required for operation. For the synthesis of ammonia, hydrogenation reactions, or for the use in fuel cells, H_2 has to be cleaned from CO, which would otherwise poison the catalysts. For this purpose, the WGS reaction is used together with the preferential oxidation of CO,

using O_2 in the presence of surplus H_2 [8].
There are several ceria-based catalysts used for the WGS reaction: Pt/CeO_2, $Pt/Ce_xZr_{1-x}O_2$, Cu/CeO_2 and Au/CeO_2 are some of them. Among these, Au/CeO_2 is considered to be one of the most promising catalysts for H_2 purification. The high performance of the Au/CeO_2 catalyst is attributed to the direct contribution of the metal-oxide interface to the catalytic process, with gold nanoparticles in contact with oxygen vacancies forming the active sites for the WGSR [18]. For Cu/CeO_2 catalysts, Cu is often present in the form of CuO. As shown in [19], several CuO/CeO_2 catalysts were produced and tried for the WGSR, concluding that the amount of surface oxygen vacancies has a large effect on the activity.

1.3 Cerium oxide crystal surfaces

1.3.1 Crystal structure

The fluorite crystal structure (space group *Fm3m*) of the fully oxidized CeO_2 is shown in Fig. 1.2, where white spheres represent oxygen and black spheres represent cerium atoms. A face-centered cubic (fcc) lattice, with a lattice constant of 5.41 Å, is formed by the Ce-cations, while the O-anions form a simple cubic lattice within the cubic unit cell. The Ce-cations each have eight O nearest neighbors and the O-anions are each tetrahedrally coordinated by four Ce nearest neighbors [6]. In its stable form, the fully reduced Ce_2O_3 has a hexagonal crystal structure (space group *P3ml*). Intermediate compositions of CeO_{2-x} (with $0 \leq x \leq 0.5$) are known to have structures strongly related to the fluorite structure, where the Ce remains close to fcc positions. The oxygen vacancies formed by the reduction can be randomly distributed or ordered. This depends on the temperature and the composition [6]. The reduction limit for cubic structures based on the fluorite lattice is the cubic bixbyite structure for c-Ce_2O_3 (space group *Ia3*) [20].

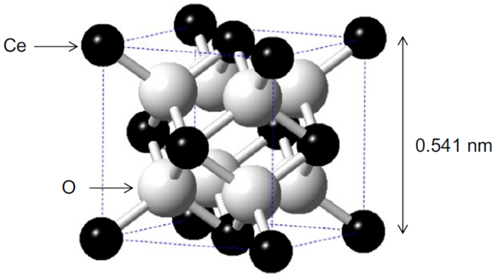

Fig. 1.2: Unite cell of CeO_2 fuorite structure, from [7].

The three low-index surface orientations of CeO_2, namely (110), (111) and (100), are of high importance both for this work and in catalytic applications. All three surfaces can be described by the three types of ionic crystal surfaces established by Tasker [21]. Figure 1.3 shows the low-index surfaces of CeO_2 depicted as unreconstructed Tasker type surfaces, with (110) as a type 1 in a), (111) as a type 2 in b) and (100) as a type 3 surface in c). For CeO_2 (110), each plane has a stoichiometric balance between anions and cations, resulting in a neutral charge and making it a type 1 surface. For CeO_2 (111), every plane has a non-zero charge, but these charges are balanced out by the repetition of units consisting of three planes. Therefore, the total dipole moment perpendicular to the surface is zero and the (111) surface is a type 2. Type 1 and 2 surfaces are expected to have low surface energies and to relax very moderately in comparison to their simple bulk truncation. For CeO_2 (100), the planes are charged alternately and units consisting of two planes are repeated. This results in a dipole moment perpendicular to the surface and the creation of a type 3 surface. In this case, the energy needed to create the surface (surface energy) is nearly infinite, and significant reconstructions compared to the bulk truncation are necessary [7].

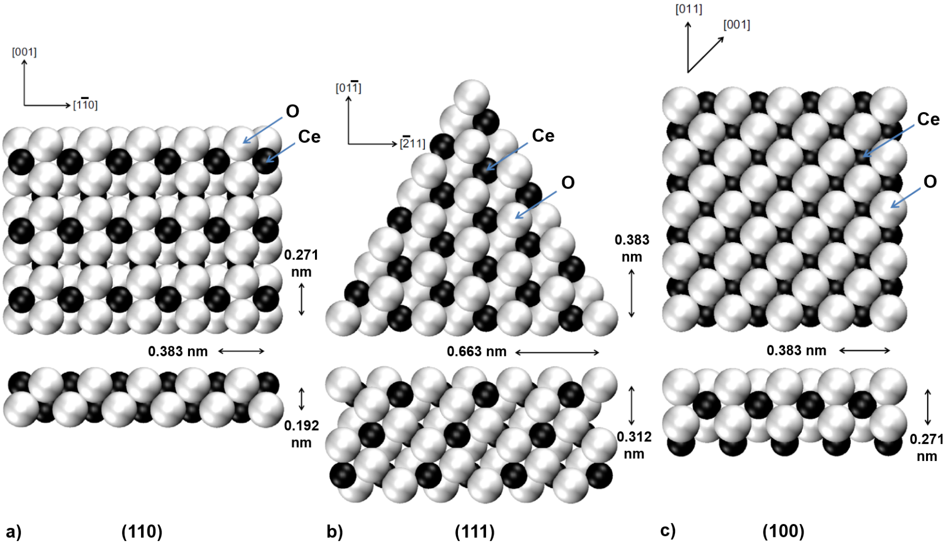

Fig. 1.3: CeO_2 low-index surfaces, depicted without reconstructions: a) (110), b) (111) and c) (100), adapted from [7].

Computational studies regarding the structure and stability of the CeO_2 low-index surfaces have established that their surface stability runs in the following order: (111) $>$ (110) $>$ (100) [22, 23, 24]. The structure shown in Fig. 1.3 b) for CeO_2 (111) has been confirmed by experiments with LEED (low energy electron diffraction), STM (scanning tunneling microscopy), AFM (atomic-force microscopy) and ISS (ion scattering spectroscopy) [25, 26, 27]. In addition, according to the ion scattering experiment, the (111) surface is considered to be terminated by O [27]. Scanning force microscopy revealed O-Ce-O triple layer steps with a height of 3.1 Å, which correspond to the side-view in Fig. 1.3 b) at the bottom [28]. For CeO_2 (110), LEED, RHEED (reflection high energy electron diffraction) and STM studies showed a (2 x 1) reconstruction [29]. The characterization of the CeO_2 (100) surface structure is not conclusive so far. Both (1 x 1) patterns and other surface reconstructions, including (2 x 2) and ($\sqrt{2}$ x $\sqrt{2}$) R45°, have been observed with LEED and STM [30, 31]. The question of the surface termination of CeO_2 (100) is also not yet fully answered. So far it seems like the (100) surface is not terminated by a solid layer of Ce or O as portrayed in Fig. 1.3 c), but can have regions of Ce, O and mixed Ce-O terminations [7, 32].

1.3.2 Oxygen vacancy creation in cerium oxide

The reduction of cerium oxide from Ce^{4+} to Ce^{3+} ions is of great relevance for all applications making use of the cerium oxide OSC. This reduction takes place through the formation of oxygen vacancies. After the creation of an oxygen vacancy on a cerium oxide surface or in the bulk, two electrons are left behind. These two electrons localize in two Ce atoms, changing their oxidation state from Ce^{4+} to Ce^{3+} [33]. The presence of oxygen vacancies is important, because they present reactive sites and enable oxygen vacancy migration. For reactions like the CO oxidation or the NO_x reduction, the oxygen vacancy formation of ceria correlates with its catalytic activity, and the oxygen vacancy formation energies can be used to predict the efficacy of catalytic reactions on ceria [34]. Therefore, it is of interest to know the energy needed to create oxygen vacancies for different ceria surfaces and for the bulk. The oxygen vacancy creation reaction can be expressed as [35]:

$$O_O^{\times} + 2\,Ce_{Ce}^{\times} \rightarrow V_O^{\bullet\bullet} + 2\,Ce_{Ce}^{\prime} + \frac{1}{2}O_2 \tag{1.1}$$

Here the Kröger-Vink notation [36] is used, and $Ce_{Ce}^{\times}$ describes a cerium ion at a cerium lattice site, with neutral charge, $O_O^{\times}$ describes an oxygen ion at an oxygen lattice site, with neutral charge, $Ce_{Ce}^{\prime}$ describes a cerium ion at a cerium lattice site, with single negative charge, and $V_O^{\bullet\bullet}$ describes an oxygen vacancy, with double positive charge.

Nolan et al. [35, 37] used density functional theory (DFT) to calculate the surface energies and the oxygen vacancy creation energies for the CeO_2 (111), (110), and (100) surfaces. DFT is a computational, quantum mechanical modeling method used to investigate the ground state of many-electron systems, particularly molecules and solids, based on the spatially dependent electron density. The resulting surface energies are 0.68 J/m^2 for (111), 1.01 J/m^2 for (110) and 1.41 J/m^2 for (100). The results for the oxygen vacancy creation energies are 3.39 eV for the bulk, 2.60 eV for (111), 1.99 eV for (110) and 2.27 eV for (100). Therefore, the surface energies for the three orientations increase as $(111) < (110) < (100)$ and the surface vacancy creation energy decreases as $(111) > (110) > (100)$. These two orders were also found in earlier simulations by Conesa et al. [22]. (100) and (110) surfaces are less thermodynamically stable than the (111) surface and thereby less likely to form the surface termination. All three surface orientations exhibit lower oxygen vacancy creation energies than the bulk. For catalytic applications benefiting from an easier oxygen vacancy formation, it is therefore desirable to increase the surface area in general. However, a preferred formation of (100) and (110) terminated surfaces would be ideal, since the vacancy creation energies for them are still lower than for the more stable (111) orientation.

1.3.3 Use of cerium oxide nanoparticles, nanorods and nanocubes

Nanostructuring can be used to prepare ceria materials with defined size, shape and morphology. Ceria nanoparticles and nanostructures, prepared by precipitation and hydrothermal synthesis, can be designed to predominantly form the less stable (100) and (110) surfaces. The primarily exposed surfaces are considered to be (111) for nanopolyhedra, (100) for nanocubes and both (100) and (110) for nanorods [38]. Examples for these ceria nanostructures can be seen in Fig. 1.4.

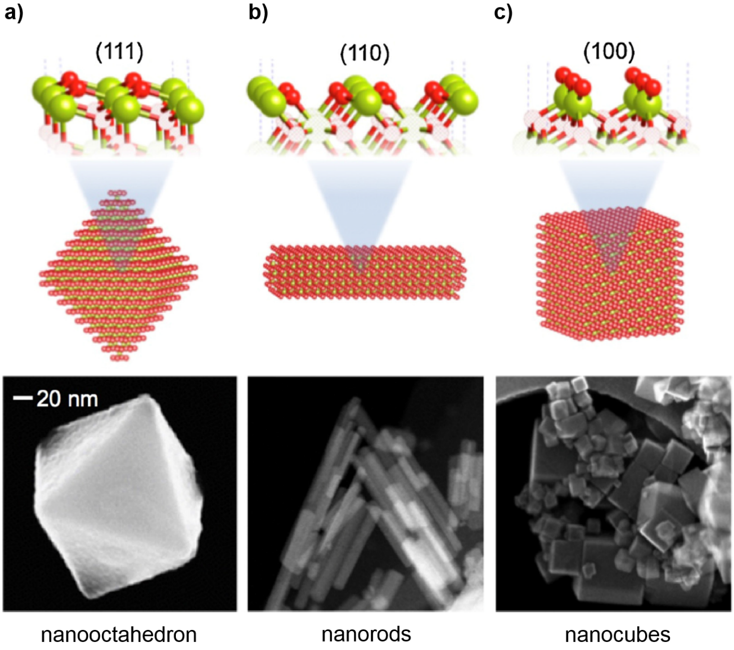

Fig. 1.4: Microscopic models and micrographs of ceria nanostructures: a) Nanooctahedron (here representative for nanopolyhedra) with (111), b) nanorods with (110) and c) nanocubes with (100) surface terminations, from [39].

For the examination of the influence of the CeO_2 nanoparticles' morphology on the catalytic oxidation of CO, irregularly shaped ceria nanoparticles were compared to single crystalline CeO_2 nanorods. Even though the irregular nanoparticles, consisting mainly of (111) surfaces, were smaller in size and had the higher surface areas, the activity of the nanorods, consisting of (100) and (110) surfaces, was determined to be three times higher. This increased activity was attributed to the exposure of the (100) and (110) surfaces [40].

In a later study, CeO_2 nanocubes (enclosed by six (100) surfaces) and octahedron-like nanopolyhedra (enclosed primarily by (111) surfaces and only few (100) surfaces) were both tested for CO oxidation and C_2H_2 hydrogenation [41]. The nanocubes performed better in the oxidation reaction and the polyhedra showed the higher hydrogenation activity. This adverse effect is explained by the easier formation of oxygen vacancies on the (100) surfaces. While the CO oxidation reaction benefits from the released oxygen, the presence of oxygen vacancies has a detrimental effect on the C_2H_2 hydrogenation, because the hydrogenation reaction needs surface oxygen atoms to stabilize reactive intermediates [42]. The ceria nanocubes and polyhedra were aged by a high temperature calcination in the same study. The effect of the aging procedure was the formation of (110) facets on the nanocubes and an increase of (100) facets on the polyhedra. In both cases, the OCS was increased by the aging, affecting the performance for CO oxidation positively and the C_2H_2 hydrogenation activity negatively. These changes can be seen in Fig. 1.5. This two-step experiment shows that the ceria surface orientation has an effect on the readiness to form oxygen vacancies and on the ceria OSC, which are both increased for the (100) and (110) surfaces compared to the (111) surface.

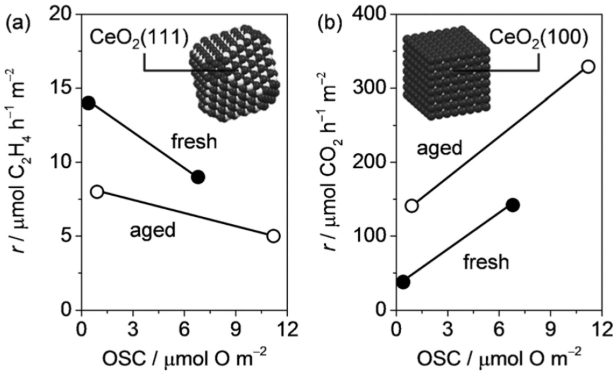

Fig. 1.5: CeO_2 reaction rates as a function of OSC: a) C_2H_2 hydrogenation with octahedron-like nanoparticles, b) CO oxidation with nanocubes, from [41].

Other examples of nanostructured particles, exposing the (100) and (110) surfaces and demonstrating the increase of OSC, can be found in [43, 44, 45].

1.4 Cerium oxide thin films and islands as model systems

Because CeO_2-based real-life applications are very complex, model systems are commonly used for simplification and thereby help with the understanding of various catalytic phenomena. This approach is also used for many other metal oxides [8]. The preparation and study of thin films makes it possible to adjust the structural properties and the stoichiometry by the choice of the substrate and growth method. Thin cerium oxide films or islands with an exclusive surface orientation

allow their separate examination in order to determine differences between the surface orientations. This is not possible for the experiments on nanoparticles discussed in subsection 1.3.3, where measurements always average over a large number of nanoparticles with more than one surface orientation each [41].
Model systems, which consist of thin epitaxial CeO_2 or CeO_{2-x} (111) films or islands, with a film thickness between some Å and several nm, have been widely used in combination with a variety of metal substrates:

- Cerium oxide nanoparticles on Au (111) were used to examine the efficacy of a Ce_{2-x}/Au (111) catalyst in the water-gas shift reaction [18]. It was shown that Au (111), which is not catalytically active in the WGS reaction on its own, becomes highly active whith a coverage of 20 to 30 % of cerium oxide. This was attributed to the direct participation of cerium oxide oxygen vacancies in the dissociation of water.

- Gold nanoparticles have been deposited on CeO_2 (111) films to study their structure with STM in CO, O_2 and CO + O_2 environments at pressures up to 20 mbar at 300 K [46]. The Au nanoparticles were shown to be stable in O_2 up to 10 mbar. In a CO atmosphere gold sintering occurred above 1 mbar and in CO + O_2 already above 10^{-3} mbar. This was interpreted as a connection between the structural stability of the Au/ceria system and its reactivity in the CO oxidation reaction.

- Tri-layers of Pd/CeO_{2-x}(111)/Rh(111) have been prepared with various CeO_{2-x} stoichiometries and have been monitored with X-ray photoelectron spectroscopy (XPS) during their modification by CO adsorption [47]. CO was observed to adsorb only in the presence of Pd, independently of the CeO_{2-x} stoichiometry. In that case, the CO adsorption did not change the CeO_{2-x} stoichiometry.

- CeO_2 (111) films have been grown on Cu (111) by Ce molecular beam deposition in an oxygen atmosphere and were examined by LEED and XPS [48]. The CeO_2 (111) films were found to grow initially in the form of epitaxial islands before forming complete epitaxial ceria overlayers. Such a continuous CeO_2 (111) film on Cu (111) was later reduced by the deposition of metallic Ce and was transformed into a c-Ce_2O_3 film [49].

- Low energy electron microscopy (LEEM) and X-ray photoemission electron microscopy (X-PEEM) were employed in several works to examine the reduction and oxidation behavior of the ceria (111) surface. The reduction of CeO_2 (111) islands on Ru (0001) in an H_2 environment was observed with PEEM and X-ray absorption spectroscopy [50, 51]. The CeO_2 (111) islands were reduced over many hours in an H_2 pressure of 2×10^{-6} mbar at 700 K and reached a stoichiometry of $CeO_{1.68}$. Ultrathin (0.5 ML) CeO_2 (111) islands prepared on Rh (111) and Pt (111) substrates were reduced by high intensity X-rays and reoxidized in an O_2 pressure of 2×10^{-6} mbar. Both processes were observed with LEEM and X-PEEM [52].

Due to the polarity of the CeO_2 (100) termination, epitaxial CeO_2 (100) surfaces are more difficult to prepare than the more stable (111) surface. Therefore, significantly fewer studies have been done on the former orientation, although promising catalytic activity was displayed for nanoparticles and nanostructures such as nanocubes and nanorods. Recent studies have presented the possibility to grow (111) and (100) oriented CeO_2 islands both on Ru (0001) [53] and Cu (111) [31, 54]. The islands can have dimensions between tenths of nm and a few µm. It has been shown by Höcker et al. that the ratio of (100) and (111) ceria terminated islands grown on Cu (111) can be controlled by adjusting the surface oxygen chemical potential [30], making it possible to grow either type of orientation separately or to grow a mixture of both. A schematic representation of the two growth modes for the (111) and (100) surface orientations is displayed in Fig. 1.6.

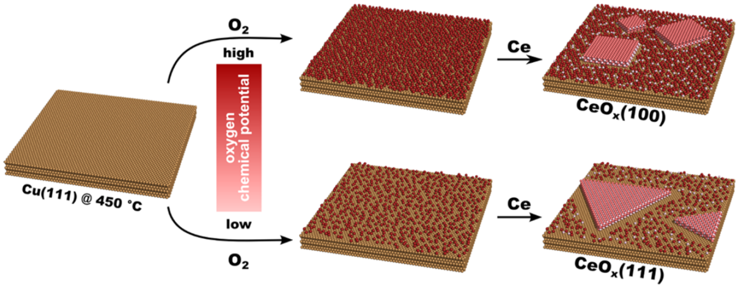

Fig. 1.6: Growth of CeO_2 (100) or (111) islands on Cu (111) depending on the oxygen chemical potential, from [30].

The growth method used in this work and described in detail in chapter 3, where exclusive (111) and (100) CeO_2 surfaces are prepared on Cu (111), is based on the recipe from [30]. LEEM, µ-LEED, X-PEEM and microscopic XAS (X-ray absorption spectroscopy) measurements then reveal the structural and chemical properties of (111) and (100) cerium oxide surfaces during reduction and provide microscopic information on the reduction process. Because islands of both orientations are grown in parallel and directly next to each other, their reduction can be examined at the same time and under identical conditions. Unlike for other model system studies, which include only one surface orientation per sample, a direct comparison of the reduction behavior of the (111) and (100) cerium oxide surfaces becomes possible by this method.

It should be noted, however, that all the systems discussed in this section are extreme model systems with respect to catalysis. This is the case because the gas pressures in a realistic catalytic reaction are orders of magnitude higher than those in a surface science experiment.

2 Experimental methods and setup

All experiments presented in this work were conducted using an AC FE-LEEM P90 instrument, an aberration corrected low energy electron microscope (LEEM) and photoemission electron microscope (PEEM) commercialized by the SPECS GmbH. This LEEM/PEEM instrument is installed as an end-station of the FZ Jülich beamline UE56/ 1-SGM at the synchrotron light source BESSY II in Berlin. Fig. 2.1 shows a photograph of the microscope at its current location.

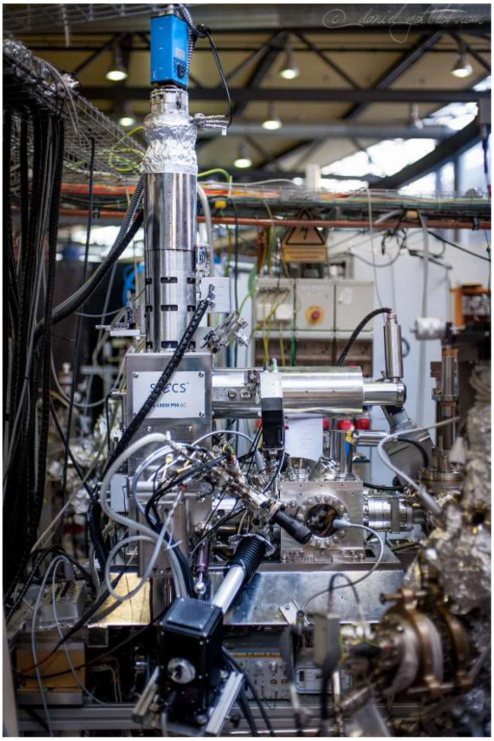

Fig. 2.1: SPECS LEEM/PEEM instrument with aberration correction, photograph from [55].

In this chapter, an overview of the LEEM/PEEM instrument's optics and functions will be given. The imaging and measurement methods of UV-PEEM, X-PEEM, μ-XAS, LEEM and μ-LEED, which were used for this study, will be explained, followed by a description of synchrotron light generation, the beamline and the techniques used for sample preparation.

2.1 The low energy and photoemission electron microscope

The setup used for the experiments described and discussed in the following chapters is a LEEM/PEEM combination microscope, developed by R. M. Tromp (IBM). Because LEEM and PEEM have similar requirements regarding the electron optics, they can be realized in one instrument. An overview of the instrument's electron optics and other configurations will be given in the following. They are explained in greater detail in [56]. The precise alignment procedure necessary for operation is described in [57]. A schematic illustration of the electron path through the microscope is displayed in Fig. 2.2.

At the current position of the microscope, two different photon sources can be used to illuminate the sample for measurements in PEEM mode: a mercury discharge UV-Lamp (UV-PEEM) and synchrotron X-ray radiation (X-PEEM). For both, the photon incident angle is about 25°. The image is formed mainly by the secondary electron cascade caused by exited photoelectrons. In LEEM mode, a collimated electron beam is produced by an electron gun and focused on the sample with a 90° incident angle. Electrons reflected or diffracted from the sample form the image.
In both cases, electrons leaving the sample with an energy E_0 are accelerated towards the objective lens (OL) by a negative potential up to $U = -15$ kV, applied to the sample. The electrons enter the objective lens with the drift energy:

$$E = E_0 + eU, \tag{2.1}$$

Increasing the applied sample potential reduces the electrons' relative energy spread $\Delta E/E$ and improves the microscope's spatial resolution by reducing the influence of small flaws in the electron optics along the electron path.
The electric field produced by the applied potential between the sample and the objective lens is called an immersion field. The concept of electronic immersion microscopy was founded by E. Brüche in 1933 [58, 59]. Today this concept is used with a cathode lens [60, 61], consisting of the sample as a cathode, the grounded front of the objective lens as an extractor and the objective lens. The possible imaging errors of cathode lenses are described in-depth in [62]. Imaging errors like defocus, incorrect tilts and astigmatisms can be corrected by the proper setup and alignment of the microscope. On the other hand, spherical and chromatic aberrations can only be corrected by specific aberration correction additions to the setup.
The objective lens is passed twice by the electrons in LEEM mode: the first time by the incident electrons on the way to the sample and the second time by the imaging electrons reflected from the sample. Two magnetic prism arrays function as 90° magnetic beam separators. The first prism (prism 1) serves to separate the incoming and the reflected electrons for LEEM. The second prism (prism 2) separates the incoming and reflected images of the aberration correction branch. In both cases, the prisms work as 1:1 transfer lenses, only deflecting the electron path by 90°.
The electron source for LEEM is a cold-cathode field-emission electron gun and the emitted electron beam is focused through the gun lens (GL) and the condensor lens (CL). For the electron emitter, the same high voltage potential as for the sample is used. In prism 1, the electron beam gets turned by 90° and is directed into the

objective branch. The negative sample potential slows down the electrons as they approach the sample surface. A difference in potentials between sample and emitter can be set in the range of ± 300 eV. Depending on this difference in potentials, the electrons can be reflected before reaching the sample surface or interact with it.

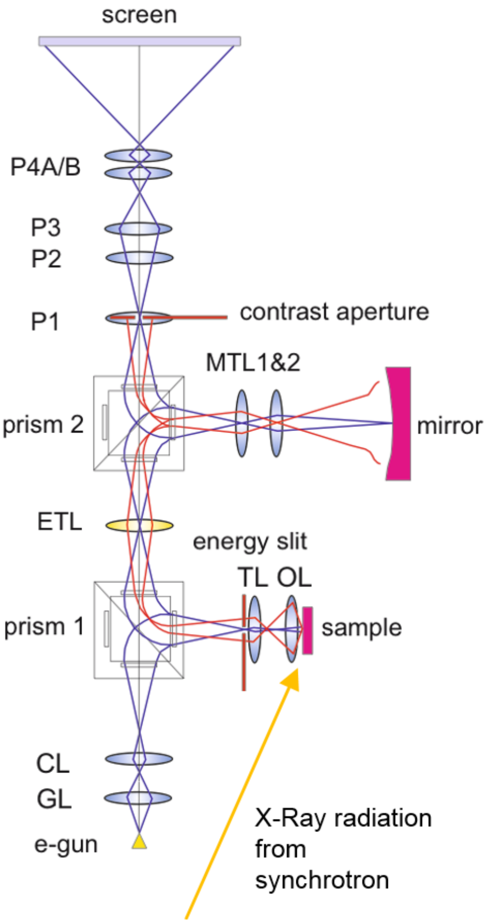

Fig. 2.2: Schematic diagram of the electron path through the LEEM/PEEM instrument with aberration correction (blue lines indicate the field rays and red lines the axial rays), adapted from [56].

The electrons emitted from the sample in LEEM or in PEEM mode create an image of the sample surface and leave the objective lens at the drift energy from equation 2.1. The image is magnified by the objective lens and the following transfer lens (TL). The electrons are deflected by 90° in prism 1. The electric transfer lens (ETL) passes the image from prism 1 to prism 2 without any other effect. This is the only electrostatic lens in the setup, all other lenses are electromagnetic.

Prism 2 directs the electrons to and back from the electrostatic electron mirror, which corrects spherical and chromatic aberrations caused by the objective lens. The electron mirror is designed as a tetrode consisting of four electrodes with

increasing potential. The mirror is used in a setting that produces aberrations directly opposite to the aberrations of the objective lens and by this removes the original aberrations. The experimental determination and calculation of the needed settings is explained elaborately in [63].
The projective lenses P1 to P4 after prism 2 magnify the image. Alongside the real space image, a diffraction image is passed through the microscope. The projective lens P2 can be used to switch between real space and diffraction imaging. By the projective lenses the electron optical image is projected onto a multi-channel plate with a phosphor screen. The image recording is done with a slow scan CCD camera.

In addition to the lenses and the two prisms, electrostatic deflectors and stigmators aid in guiding the electron path through the microscope as desired. Several apertures, that act as area selectors, can be placed in the diagonals of the two prisms and the electron mirror branch to improve the image and help with the image adjustment.
The sample is mounted in a sample stage moved by piezo-drives in five axes. Using the sample stage, the distance between the sample and the objective lens can be set to the correct position for the objective lens focus. The sample tilt can also be corrected, so that the sample surface is normal to the optical axis, which is necessary to prevent imaging errors. The stage is used used for translations movement on the sample. An azimuthal rotation - a sixth independent axis - is controlled by a stepping motor.
The best resolutions achieved with this microscope as a beamline end-station are 5 nm for LEEM and 34 nm for X-PEEM [63].

2.2 Imaging and measurement methods

2.2.1 Photoemission

Imaging with PEEM, as applied for this work, is based on the principle of photoemission. The photoemission process describes the interaction of photons with matter, resulting in the emission of photoelectrons, due to an energy transfer from the photons to the illuminated matter. This effect, called the photoelectric effect, was explained by Einstein in 1905 [64].
The energy relation of the photoelectric effect connects the energy of the incident photon $E_{\mathrm{ph}} = h\nu = \hbar\omega$ with the kinetic energy E_{kin} of the emitted electron, the binding energy of the electron, and the material's work function Φ, which is the potential barrier of a solid:

$$\hbar\omega = E_{\mathrm{kin}} + E_{\mathrm{bin}} + \Phi \tag{2.2}$$

The transition probability w for an electron to be excited from an initial state i with wave function Ψ_i to a final state f with wave function Ψ_f is given by Fermi's golden rule [65, 66]:

$$w_{fi} = \frac{2\pi}{\hbar} |\langle \Psi_f | H^{\mathrm{int}} | \Psi_i \rangle|^2 \, \delta(E_f - E_i - \hbar\omega) \tag{2.3}$$

and determined by the transition matrix element:

$$M_{fi} = \langle \Psi_f | H^{\text{int}} | \Psi_i \rangle \tag{2.4}$$

where H^{int} is a small perturbation due to incident photons. In equation 2.3, $E_f - E_i$ is the energy difference between the states $\langle \Psi_f |$ and $| \Psi_i \rangle$ and the δ-function secures the energy preservation.

With the vector potential $\mathbf{A}$ of the external electric field accounting for the effect of the incident photons, the momentum operator $\mathbf{p}$, the speed of light c, the electron charge e and the electron rest mass m the perturbation H^{int} can be expressed as:

$$H^{\text{int}} = \frac{e}{mc} \mathbf{A} \cdot \mathbf{p} \tag{2.5}$$

The vector potential $\mathbf{A}$ can be described in form of a planar wave:

$$\mathbf{A}(\omega t) = A_0 \, \boldsymbol{\sigma} \, \mathrm{e}^{i(\omega t - \mathbf{q} \cdot \mathbf{r})} \tag{2.6}$$

where $\boldsymbol{\sigma}$ is the photon polarization, $\mathbf{q}$ is the photon momentum and $\mathbf{r}$ is the coordinate. When the photon wavelength is large compared to the atomic distance ($\lambda >> r_0$), $\mathbf{A}$ can be assumed to be constant, which is called the dipole approximation [67]. This leads to $\mathrm{e}^{i(\omega t - \mathbf{q} \cdot \mathbf{r})} \sim 1$ in equation 2.6. With the dipole approximation the transition matrix element is simplified to:

$$M_{fi} \propto \langle \Psi_f | \boldsymbol{\sigma} \cdot \mathbf{p} | \Psi_i \rangle \tag{2.7}$$

Selection rules describing allowed and forbidden transitions between initial and final states can the obtained from the transition matrix, when the wave function symmetries are considered. The selection rules evaluate the transition possibility based on the quantum numbers $|n, l, m_l, s, m_s\rangle$. Wave-functions of atomic core levels can be described by a radial part, spherical harmonics and a spin part [68]:

$$|\Psi\rangle = |R(r)\rangle |Y_{l,m_l}(\theta, \phi)\rangle |X(s)\rangle \tag{2.8}$$

The transition matrix element M_{fi} in equation 2.7 is only non zero for specific values of l and m_l resulting in the dipole selection rules for photo-excitation:

$$\Delta L = \pm 1 \quad \text{and} \quad \Delta m_L = 0, \pm 1 \quad \Rightarrow \quad M_{fi} \neq 0 \tag{2.9}$$

for the total angular quantum number L and the total magnetic quantum number m_L. For the inclusion of spin-orbit coupling, the combined angular quantum number $J = L + S$ with the spin quantum number S needs to be used [68]. The photoelectron current produced by photo excitation is therefore proportional to the sum of the transition probabilities in equation 2.3 over all allowed transitions.

The description of the photoemission process is often divided into three parts by using the so called three-step model [67]. These three parts are:

1. The excitation of an electron in the solid caused by incident photons.

2. The excited electron's propagation through the solid.

3. The escape of the photoelectron from the solid into the vacuum.

Therefore, besides the photoexcitation process discussed above, the produced photelectron current also depends on the inelastic mean free path of electrons in the solid material and the surface potential barrier, which is connected to the material's work function.

2.2.2 The electron inelastic mean free path

Electrons traveling through a material encounter elastic and inelastic scattering, which changes their momentum and energy. Inelastic scattering events lead to a loss in the electrons' kinetic energy. When electrons travel a distance x from their point of origin, their primary intensity I_0 is dampened as a function of x. The loss in intensity is given by [69]:

$$I(x) = I_0\,\mathrm{e}^{-x/\lambda_{\mathrm{IMFP}}} \tag{2.10}$$

The inelastic mean free path λ_{IMFP} is defined as the characteristic distance that electrons can travel through a material, until an intensity decay by a factor of $1/\mathrm{e}$ is reached. Measurement techniques using electrons have a probing depth determined by the IMFP, which depends on the kinetic energy of the electrons and the density and electronic properties of the material. The general dependency of the IMFP on the electron energy, can be seen in Fig. 2.3, which shows IMPFs calculated by the TPP2M method [70] for 41 different materials in an energy range from 10 to 20000 eV. The shape of the curves in Fig. 2.3 reflects the so called universal curve. The minimum electron IMFPs lie in an energy range between 50 and 100 eV. For lower and higher electron energies, the IMFP increases.

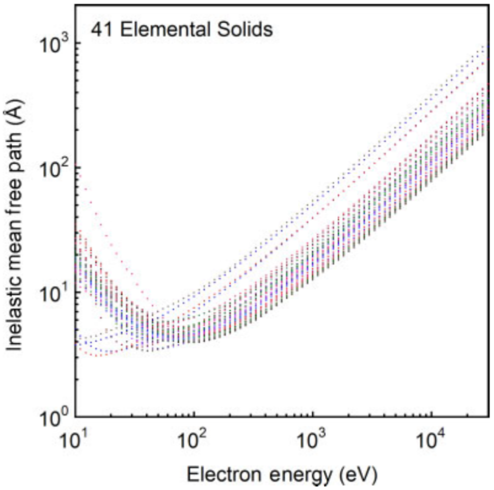

Fig. 2.3: The universal curve for electron IMFPs calculated for 41 elemental solids, indicated by different colors, from [71].

However, determining the probing depth with equation 2.10 by directly using the IMFP only works well for experiments measuring primary electrons, which only experience elastic scattering. For experiments measuring secondary electrons, the detection of scattered electrons generally increases the probing depth, which is then in the order of nanometers [72]. This is discussed in more detail in section 3.2.4, where the intensity damping of secondary electrons is used to determine the thickness of prepared cerium oxide layers.

2.2.3 UV-PEEM (UV-light photoemission electron microscopy)

The imaging mode for PEEM with the mercury-discharge UV-Lamp as light source is also called threshold PEEM. Generally the kinetic energy of electrons, exited by photons with an energy of $h\nu$, is spread over a broad spectrum. The electron energy spectrum comprises primary photoelectrons with a kinetic energy of $E_{\text{kin}} = h\nu - E_{\text{bin}} - \Phi$ (following from equation 2.2) and secondary electrons with lower energies due to energy loss by inelastic scattering.

In the case of threshold photoemission, the photon energy is is comparable to the sample's work function. Electrons are only emitted from the sample, if the excitation photon energy is higher than the sample's work function. This means that the electrons are exited only from a narrow window around the Fermi level, which strongly reduces the electron energy distribution [73]. A schematic electron spectrum for threshold PEEM, showing the electron yield over the electrons' kinetic energy, is displayed in Fig. 2.4 a). The narrow energy width of the emitted electrons leads to a strong dependence of the resulting electron yield, and thereby the intensities in the PEEM image, on the surface work function.

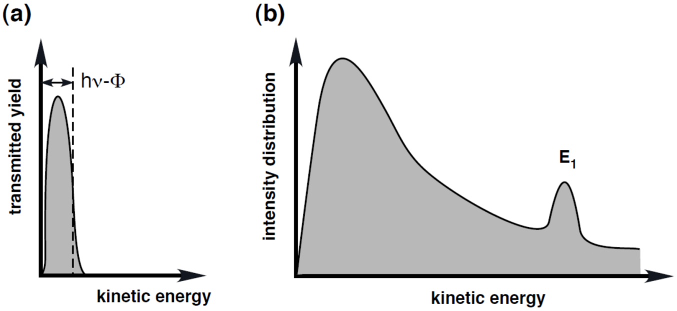

Fig. 2.4: Schematic electron spectra: a) for UV-PEEM with threshold photoemission, b) for X-PEEM with high photon energy (X-ray) excitation, from [73].

The used mercury-discharge lamp is a broad band photon source with its most prominent spectral line at a photon energy of 4.9 eV. Work functions of different materials can typically vary between 2 and 5 eV, and for some materials different exposed crystal surface terminations can change the work function by a few 0.1 eV [73]. Therefore, a sample surface consisting of different materials or different crystal orientations of the same material, will show different image intensities which form a contrast pattern. The usefulness of this contrast mechanism will be revealed in Fig. 6.1 in chapter 6, where different ceria surface terminations are compared. Monolayers of adsorbates can also alter the work function of a surface and lead to a change in contrast.

A second contrast mechanism becomes visible, if the sample has topological structures. This contrast is induced by local distortions of the electric field between the sample and the objective lens, causing deviations from the ideal cylindrical symmetry of the accelerating field. The trajectories of electrons passing through these local field deviations can be spread out or compressed, depending on the shapes of the topological structures. This causes areas with lower or higher intensities in the resulting image. This effect is illustrated in Fig. 2.5.
It should be noted that topological contrast mechanisms exist not only for UV-PEEM, but also for the other imaging methods (X-PEEM and LEEM) discussed in this section and that the contrast mechanisms for each imaging method are superimposed.

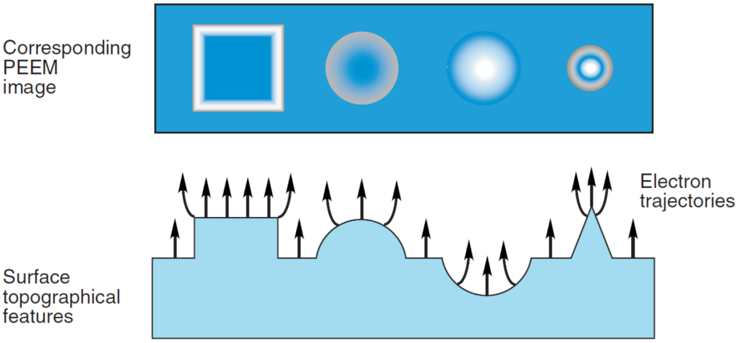

Fig. 2.5: Topological contrast in PEEM imaging, caused by topology induced electrostatic field distortions, from [74].

2.2.4 X-PEEM (X-ray photoemission electron microscopy) with secondary electrons

PEEM imaging with secondary electrons excited by soft X-rays with variable energy is one of the main imaging mechanisms used in this work. The photon energy is set to a characteristic absorption energy of the examined element. This causes the element specific excitation of core level electrons into unoccupied states, with a hole remaining in the core level. For soft X-ray absorption, the core hole is refilled with the highest probability by an Auger process. This leads to the emission of high energy Auger electrons. As the Auger electrons move through the solid they scatter inelastically in the sample. The scattering events cause a cascade of secondary electrons which are emitted above the vacuum level and create the PEEM image [73].

The core hole decay and Auger electron generation, which initiate the secondary electron cascade, determine its electron energy distribution. Therefore, the chemical information is passed on to the secondary electron yield, in the form of the measured intensity at the selected absorption photon energy. In other words, the secondary electron intensity is proportional to the X-ray absorption. When the photon energy is set to an absorption edge of a selected element, the created X-PEEM image laterally resolves the distribution of the element on the sample, with the areas containing the element appearing bright.

The much wider spectrum of electron kinetic energies for excitation with X-rays is shown in Fig. 2.4 b), compared to the narrow energy width for UV-light excitation. The broad electron energy distribution, peaking at low kinetic energies, belongs to the secondary electrons. At higher kinetic energy, the small peak indicated by E_1 belongs to primary photoelectrons or Auger electrons, which are present together with the secondary electrons in the total electron yield (TEY). In the case of the experiments described here, the image is created by secondary electrons measured in partial electron yield (PEY). The measurement of the PEY instead of the TEY is caused by the electron optics of the microscope, which functions as a band pass filter. Due to this band pass characteristics, the main contribution comes from low-energy electrons in a $\sim 10-15$ eV wide window. The yield strongly increases towards low energies (Fig. 2.4 actually underestimates this increase) and therefore the PEEM signal very closely mimics the TEY. The expression PEY is more appropriate for the detection of energy filtered electrons in a narrow energy window.

The low kinetic energy cutoff of the secondary electrons (or the secondary electron onset) shown in Fig. 2.4 b) can be used to probe the work function of the sample [75]. This is done with the combination of detecting energy filtered electrons and changing the sample potential in a precise small-stepped manner. By scanning through the electron energy spectrum, the energy position of the low kinetic energy cutoff can be determined. The absolute value of the sample work function can be determined with a well-calibrated energy analyzer (for example, a hemispherical analyzer), which yields an absolute energy scale. In the case of the used instrument, however, the energy scale is only relative, because the energy slit and the contrast aperture, which form the entrance and exit slits of the magnetic energy filter, are positioned manually and arbitrarily. Therefore, only relative differences in the work function of a sample can be determined.

For X-ray absorption spectroscopy (XAS), the photon energy is scanned with small steps over an absorption edge of an element present in the sample. Measuring the PEY at each step reveals the shape of the absorption peaks. By recording an X-PEEM image at every energy step, it is possible to gather a separate spectrum of every image-point of the imaged area. With this method, called μ-XAS, X-ray absorption spectroscopy is combined with microscopic information. An example for the use of the X-PEEM imaging and μ-XAS combination can be seen in Fig. 3.11 in chapter 3, where absorption spectra are obtained from micro-sized ceria islands in order to determine their stoichiometry.

2.2.5 LEEM (low energy electron microscopy), LEED (low energy electron diffraction) and micro-LEED

For LEEM imaging, the sample is illuminated with a collimated electron beam at a normal incidence angle and the elastically back-scattered electrons form the image. The electrons emitted by the electron gun are accelerated close to the same potential as the sample. As the electrons approach the sample, they are slowed down in the sample potential to an energy of a few eV (generally < 100 eV). The potential difference between the incident electrons and the sample can be adjusted by changing the sample potential. This difference in potential is also referred to as the LEEM start energy in the following chapters. If the sample potential is slightly larger than the electron energy, the electrons are reflected shortly before they arrive at the sample surface. In this imaging mode, called mirror electron mode LEEM (MEM-LEEM), the electrons are very sensitive to local variations of the electric field at the surface. These local variations can be caused by the surface topography, variations of the surface work function or differences in surface conductivity [76, 77]. When the sample potential is decreased below the MEM-LEEM level, the incident electrons penetrate the sample surface and interact with it by scattering and diffraction. The produced real-space LEEM image then contains information of a few sample layers, with the probing depth depending on the LEEM start energy. Main imaging contrast mechanisms are local lateral differences of the diffraction, and interference effects caused by the reflection of electrons at atomic steps or areas with different film thicknesses [76]. In addition, different regions of the sample can show variations in their electron reflectivity values, influenced by the elements on the surface [78] and the surface structure [79].
For the used microscope, the area illuminated by the electron beam in LEEM is an oval with axis lengths of 12 and 8 μm.

The imaging mode can be changed from real-space LEEM imaging to the reciprocal space. Then the LEED pattern of the sample region illuminated with the electron beam is displayed. The LEED pattern, formed by diffraction spots, is used to determine the crystallographic structure of the sample at this very location. The diffraction spots are created by electrons elastically scattered on the crystal lattice, which leads to constructive interference following Bragg's law:

$$2d \sin \Theta = n\lambda \tag{2.11}$$

with the lattice constant d, the scattering angle Θ, an integer number n and the de Broglie wavelength λ of the incident electrons. A geometrical model for diffraction based on Bragg's law is shown in Fig. 2.6. The formed diffraction pattern depicts a Fourier transformation of the surface crystal structure into the reciprocal space.

The LEED patterns obtained from the diffraction plane of the LEEM instrument are comparable to the ones from conventional LEED systems, with a few differences. The LEED patterns in LEEM show the central (00) spot, which is usually hidden by the electron gun for conventional LEED systems. Unlike for standard LEED systems, the scale of the reciprocal image is constant, independent of the used start

energy. A disadvantage of using the diffraction plane of this microscope is the limited acceptance angle of the electron mirror in the aberration correction branch. This limits the use of LEED to low start energies, because the LEED patterns begin to distort for start energies above 17 eV.
On the other hand, the combination of LEEM and LEED makes the measurement of μ-LEED possible. In this LEED, mode a small aperture is inserted into the electron beam before it reaches the sample, which reduces the illuminated area on the sample. An area as small as 200 nm can be selected in the real-space LEEM image and used to obtain a LEED pattern. If a sample surface has different surface orientations on a microscopic level, these can be determined with μ-LEED. The combination of LEEM imaging and μ-LEED is used in this work to determine the different surface orientations of ceria islands, as can be seen in Fig. 3.9 in chapter 3.

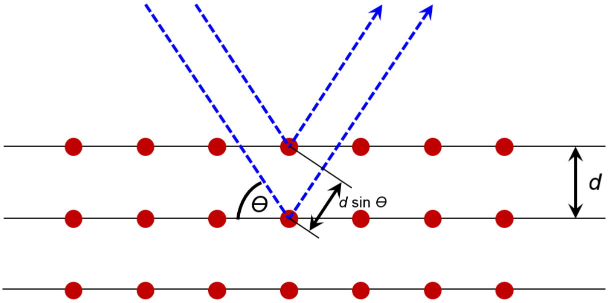

Fig. 2.6: Geometrical model for Bragg diffraction.

2.3 Synchrotron radiation photon source

Synchrotron facilities are used as high intensity photon sources with tunable wavelengths, ranging from infrared light to soft and hard X-rays. The synchrotron light can be used for X-ray photoelectron spectroscopy, X-ray absorption spectroscopy, scattering and diffraction experiments, X-ray photoemission electron microscopy, X-ray transmission microscopy and many other techniques. In a synchrotron, electrons or positrons are accelerated to relativistic energies and magnetic fields keep the electrons on their circular orbit. When the electrons pass bending magnets or insertion devices like undulators, they emit synchrotron radiation. The radiation is then transported to the experiments by beamlines [80].

An accelerated charged particle, in this case an electron, emits electromagnetic radiation, as known from classical electrodynamics [81]. A particle moving with a velocity v on a circular orbit with a radius R is kept on its orbit by an acceleration, directed inwards, perpendicular to the velocity. For highly relativistic electrons on a circular trajectory, with a velocity of $v \approx c$ ($\beta = v/c \approx 1$), the power P emitted by an electron is given by:

$$P = \frac{2e^2c}{3R^2}\left(\frac{E}{m_0c^2}\right)^4 \tag{2.12}$$

Here e is the electron charge, c is the speed of light, E is the electron's energy, and m_0 the electron's rest mass. For $\beta \ll 1$, the radiation emission has a dipole character. But for $\beta \approx 1$, the emitted radiation forms a narrow cone with an opening angle Θ around the electron motion direction. The opening angle is described by $\Theta = 1/(2\gamma)$ with $\gamma = \sqrt{1/(1-v^2/c^2)}$, and the spectral distribution of the emitted frequencies is a continuum, limited by $\omega = 3v\gamma^3/(2R)$ [81]. This is the effect used for the generation of synchrotron light.

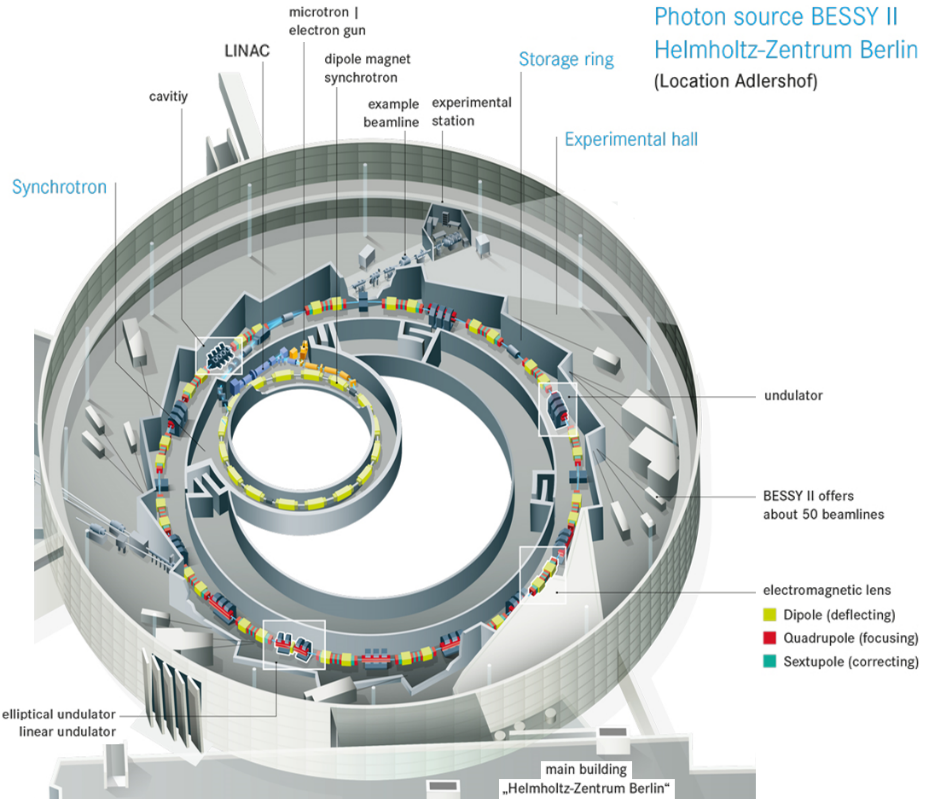

Fig. 2.7: Schematic view of BESSY II including injection gun, booster ring, storage ring, magnets, undulators and beamlines, adapted from [82].

The experiments in this work were conducted at the 3rd generation synchroton facility BESSY II. A schematic top view of BESSY II and its ~50 beamlines can be seen in Fig. 2.7. First, the electrons are accelerated in the linac (linear particle accelerator) and the booster synchrotron ring and then injected into the storage ring. The electron orbit in the storage ring has a circumference of 240 m and is controlled by 32 deflecting magnets, consisting of dipoles, quadrupoles and sextupoles. In realitiy, synchrotrons and storage rings are not ideally circular, but comprise polygons with bending magnets at the corners. Insertion devices are built into the straight passages between the magnets; undulators are commonly used. Undulators consist of periodical arrays of magnet pairs with alternating magnetic field directions, which bring the electrons onto a sinusoidal trajectory. The radiation emitted inside the undulator undergoes constructive and destructive interference. This generates monochromatic radiation with a narrow energy width and a high peak intensity around one wavelength and its harmonics [80]:

$$n\lambda = \frac{\lambda_\mathrm{u}}{2\gamma^2} \cdot \left(1 + \frac{1}{2}K + \gamma^2\Theta_\mathrm{u}^2\right), \quad n = 1, 2, 3, \ldots \tag{2.13}$$

with the period of the magnet pairs λ_u and the observation angle with respect to the undulator axis Θ_u. Due to the deflection parameter

$$K = 0.934\,\lambda_\mathrm{u}[\mathrm{cm}] \cdot B[\mathrm{T}] \tag{2.14}$$

the energy/wavelength of the radiaton generated by the undulator can be changed by altering the magnetic field B. A geometrical change of the undulator magnet arrays can also change the radiation polarization.

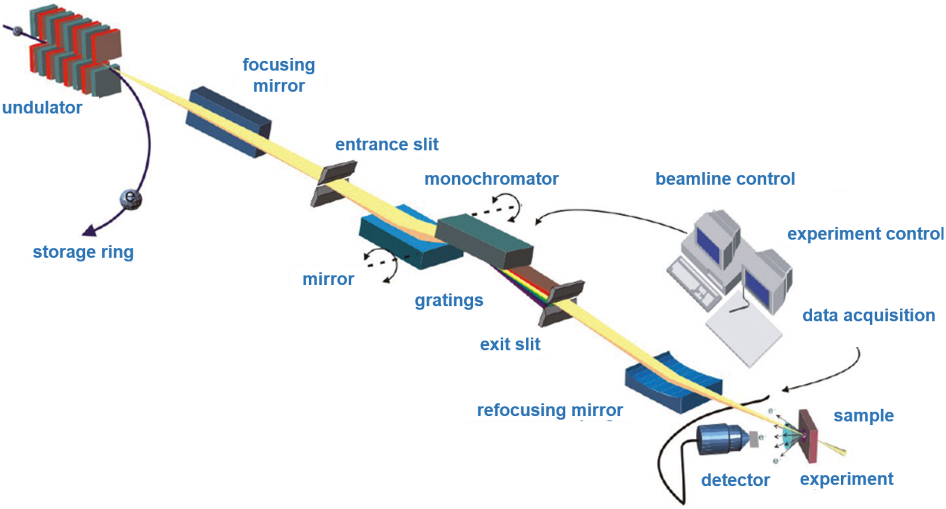

Fig. 2.8: Schematic of typical beamline setup, adapted from [82].

The FZ Jülich beamline UE56/ 1-SGM is an undulator beamline with a energy range of 55 - 1500 eV and a variable polarization. The built in undulator is of the Apple II type [83] and the period of its magnet pairs is $\lambda_\mathrm{u} = 56\,\mathrm{cm}$. The beamline is equipped with horizontal and vertical focusing mirrors, an entrance and exit silt and a monochromator with five spherical gratings. A schematic of the optical components and setup of an undulator beamline at BESSY II can be seen in Fig 2.8. Other than depicted in the schematic, the beamline UE56/ 1-SGM has two focusing and refocusing mirrors, with a horizontal and vertical mirror each in the Kirkpatrick–Baez mirror geometry [84]. Besides transporting the synchrotron light to the experiment, it further monochromatizes the light and focuses it onto a spot size of 40 µm × 70 µm on the sample.

2.4 Sample preparation methods

2.4.1 Used substrates

The substrates used for the experiments are Cu (111) and Cu (100) single crystals grown, cut and polished by the MaTeck GmbH. The maximum miscut angle is < 0.1° and the surface roughness is < 30 nm for a new crystal. A photograph of a new Cu (111) crystal is shown in Fig. 2.9. The copper crystals are cut into a hat shape, because the shape is ideal for a secure, flat and strain-free mounting on the used sample holder. The sample diameter is 8.5 mm and the polished diameter is 6.5 mm. The sample thickness is 1.2 mm in the polished area in the center and 1 mm at the rim.

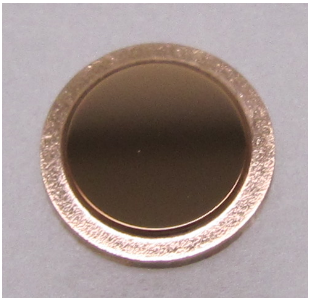

Fig. 2.9: Photograph of new Cu (111) single crystal with hat shape cut.

2.4.2 Vacuum layout and preparation chamber

A schematic of the vacuum layout can be seen in Fig. 2.10, showing the access of the load lock, the microscope and the preparation chamber via the transfer chamber. Under operative conditions, the base pressure of the microscope is 5×10^{-10} to 1×10^{-9} mbar. The preparation chamber, which can be used for sample cleaning and preparation without exposure to air before measurements, has a base pressure of 9×10^{-11} mbar.

The copper crystals are cleaned in the preparation chamber, which has a five-axis manipulator with electron-beam heating. A pyrometer (250-1400 °C) is used to measure the temperature (also used in the microscope). Furthermore, the preparation chamber is equipped with an Ar^+-ion beam sputtering gun and two gas inlets for Ar and O_2. These are used for the multiple cycles of sputtering, annealing and annealing in O_2 atmosphere, which are needed to obtain a clean and smooth crystal surface, as described in detail in subsection 3.1.1.

A system for Auger electron spectroscopy (AES) by STAIB instruments is also available. With AES, the chemical composition of a sample surface can be determined, using the electrons emitted due to the Auger process [85]. In the Auger process, a core-level electron is removed by an incident electron. An electron from an outer shell fills the core hole. The binding energy difference between the outer shell and the core shell is transferred to the Auger electron which is then emitted. For the AES system described here, an incident electron beam of 3 - 5 keV is used. The electrons are detected by a channeltron after traveling through a single pass cylindrical mirror energy analyzer. A lock-in amplifier improves the signal-to-noise ratio and provides spectra in a derivative mode. For the sample preparation, AES is used to detect contamination of the Cu crystals, for example with carbon. AES is also used to verify the presence of elements, which do not have usable edges for XAS, like the platinum deposited on top of the cerium oxide in chapter 6.

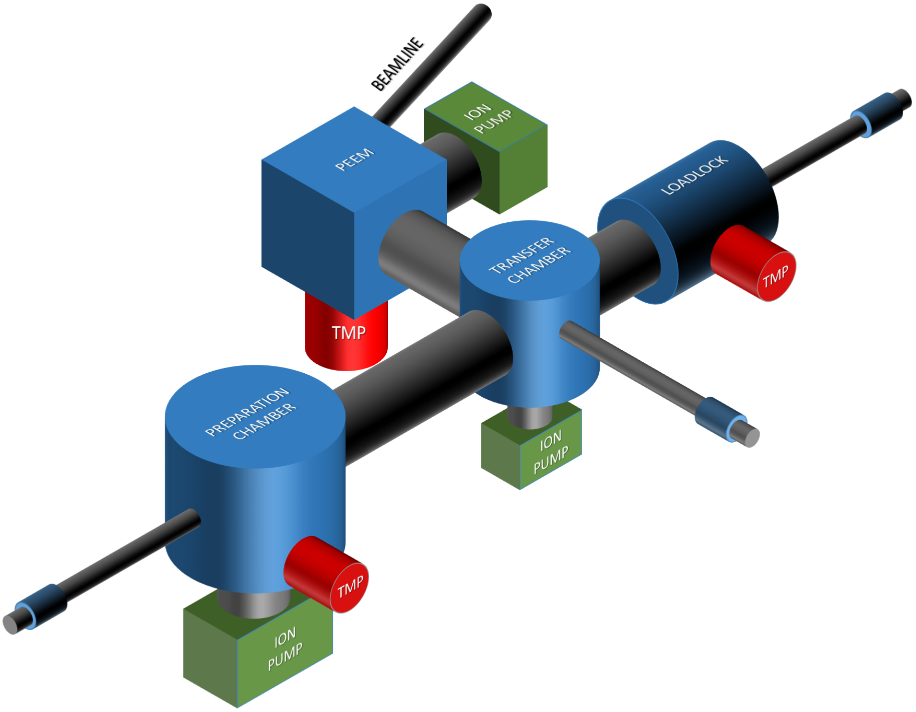

Fig. 2.10: Schematic of the vacuum layout of the used experimental setup, showing vacuum chambers in blue, turbo molecular pumps in red and ion getter pumps in green.

2.4.3 In-situ cerium oxide and platinum growth

The growth of cerium oxide on the clean Cu crystals is done in-situ, observed in real-time with LEEM. Therefore, the Cu crystal is positioned in front of the LEEM/PEEM extractor during the growth. The used sample potential is -6 kV, and the sample is heated to 450 - 500 °C by electron-beam heating implemented in the sample holder. A gas inlet system with a leak valve and an O_2 minican provides the oxygen ambience for the growth. The low sample potential of -6 kV (compared to the standard potential of -15 kV) is used due to the presence of an oxygen pressure of 5×10^{-7} mbar in the microscope chamber. A higher sample potential could lead to discharges between extractor and sample in this pressure range. In the oxygen ambience, cerium is deposited onto the Cu crystal at a shallow incidence angle with a deposition rate of ~ 0.2 Å/min. The deposition rate was determined by the thickness of grown ceria islands in dependence of the deposition time, with consideration of their surface coverage. The cerium is evaporated from a Focus EFM 3T evaporator using a tungsten crucible, filled with parts of a cerium wire. A schematic for the used growth arrangement is shown in Fig. 2.11. A different cell of the Focus triple evaporator is used for the evaporation of platinum from a Pt rod.

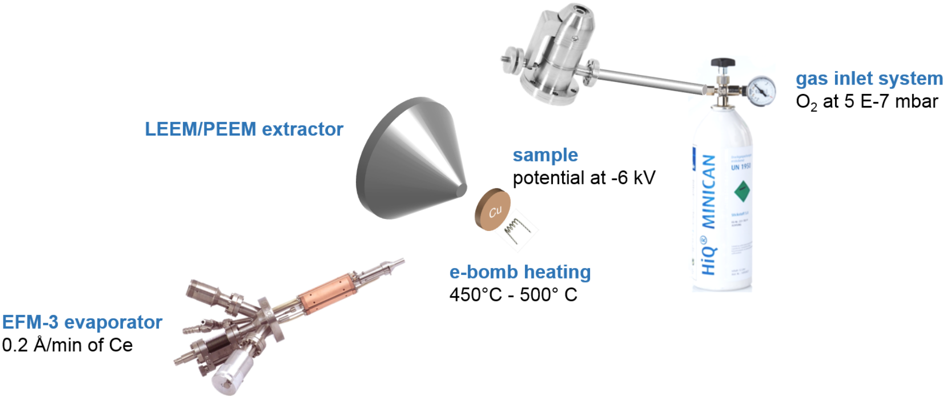

Fig. 2.11: Setup for cerium oxide growth, in-situ in the LEEM/PEEM instrument.

3 Cerium oxide islands on copper single crystals

The preparation of microscopic ceria islands on Cu (111) and Cu (100) single crystalline substrates will be described in this chapter. This includes the substrate preparation, the growth process of the ceria islands and the characterization of their properties.

3.1 Preparation of (111) and (100) cerium oxide islands on copper (111)

CeO_2 islands with (111) and (100) surface orientations are prepared simultaneously on Cu (111), so that islands of both surface orientations can be observed within a field of view (FOV) of 10 μm. These CeO_2 islands are then used for observations of the reduction behavior of ceria surfaces with different orientations, discussed in the chapters 4 and 5.

3.1.1 Copper (111) substrate preparation

The copper (111) single crystals are prepared by several cycles of argon ion sputtering, annealing at 600 °C and annealing at 600 °C in an oxygen partial pressure of 5×10^{-7} mbar. This procedure removes crystal impurities, among which carbon and sulfur are the most common for copper crystals [86].

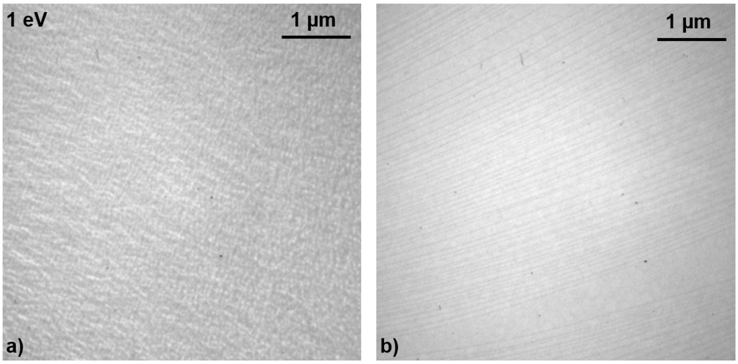

Fig. 3.1: LEEM images (1 eV start energy) of a clean Cu (111) substrate: a) directly after Ar^+-sputtering, b) after annealing at 600 °C in 5×10^{-7} mbar of oxygen.

In order to completely clean a crystal, 4 to 5 cycles of sputtering and annealing are needed. The sputtering time for each cycle is 2 h and the used Ar^+ pressure is 6×10^{-6} mbar. For a new crystal, an ion-beam incidence angle of 85° and an energy of 1.3 kV is used, with a typical ion current of $\sim 5\,\mu A/cm^2$. When a crystal is reused and an old ceria layer has to be removed, it has proven to be effective to alternate 85° and more shallow 45° incident angles for successive cycles. When the 45° incidence angle is used, the sputtering energy is increased to 1.5 kV (typical ion current of $\sim 3\,\mu A/cm^2$). Each sputtering is followed by annealing to heal the crystal surface after extended time of sputtering. Moreover, annealing brings crystal contamination to the surface. The crystal contamination is only gradually removed by repeated sputtering and annealing.

The preparation process is observed with live LEEM imaging. A LEEM start energy of 1 eV is used to image the surface roughness and crystal terraces. Fig. 3.1 shows LEEM images of a clean Cu (111) crystal surface before and after annealing. After sputtering, the copper surface has a rough texture, as can be seen in Fig. 3.1 a) and 3.2 a). During the heating process (up to 600 °C), terrace step boundaries become visible and become more pronounced as the temperature increases (Fig. 3.2 b)). When oxygen is introduced, the step boundaries become blurred. After some minutes, the step boundaries reappear and are then straighter, smoother and closer to being parallel than before (Fig. 3.2 c) and 3.1 b)). These observations indicate the oxygen adsorption on the substrate, followed by a migration of the step boundaries due to the enhanced mobility of atoms on the surface [87]. The step boundary migration combined with the removal of crystal impurities (in this case primarily the burning of carbon impurities) leads to more evenly shaped terraces. The mean width of the terraces is tens to hundreds of nm and no visible defects or imperfections are present. This shows that the substrate is a clean, very flat and well-defined support for the consequent growth.

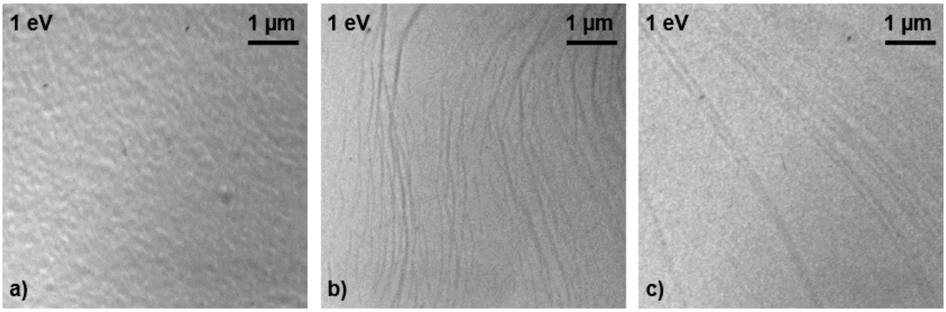

Fig. 3.2: LEEM images of a clean Cu (111) substrate during annealing: a) at room temperature after sputtering, b) at 600 °C in vacuum, c) at 600 °C in 5×10^{-7} mbar of O_2.

Although the oxygen ambience has a positive effect on the substrate terrace shapes, this is not the main reason for the annealing in oxygen. Most importantly, annealing in oxygen prepares the copper substrate for the growth of CeO_2 by covering the copper surface with an adsorbed oxygen over-layer.

Several types of ordered copper oxide structures have been reported in literature for Cu (111) substrates upon oxygen exposure [88, 89, 90]. After cooling the substrate down to temperatures below 300 °C, LEEM contrasts and LEED reconstruction patterns corresponding to the "44" and "29" structures, which are related to Cu_2O, were observed. At temperatures in the range of 300 °C to 600 °C, these structures were not observed at all with LEEM, LEED or µ-LEED. It follows that, under these conditions, the oxygen on the Cu (111) surface is highly mobile and adsorbs in an disordered manner without the formation of a periodic arrangement of copper and oxygen atoms. This behavior of the Cu (111) substrate in an oxygen atmosphere of 5×10^{-7} mbar is in agreement with the observations in [30, 91] for temperatures above and below 300 °C.

Over the course of time, the copper crystals were reused for growth with subsequent crystal cleaning multiple times, with one crystal being used for up to ~20 growths. Any cerium oxide leftover on the crystal due to incomplete cleaning can influence the next growth. Therefore, achieving the same substrate surface quality for each growth is necessary.

Incompletely cleaned crystals can be easily recognized by terraces, which are already visible directly after the sputtering and have typical shapes. Three examples of Cu (111) substrates with remaining cerium oxide from the growth before can be seen in Fig. 3.3. Small cerium oxide particles on the surface cause terrace patterns with corners forming at the locations of particles. The amount of remaining cerium oxide increases from Fig. 3.3 a) to c), as can be seen by the increasing number of bends and corners in the terraces.

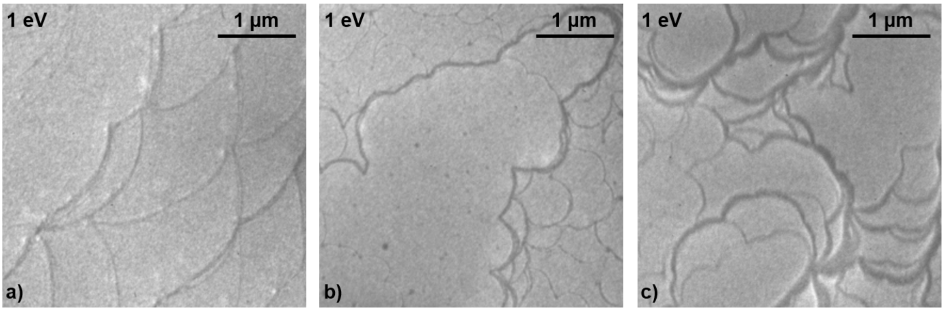

Fig. 3.3: LEEM images of incompletely cleaned Cu (111) substrate after several cycles of Ar-sputtering and annealing. The remaining cerium oxide amount increases from a) to c).

Besides remaining on the surface, cerium oxide can also accumulate inside the Cu crystal. During annealing in oxygen, this leftover material segregates to the surface and becomes visible. An incompletely cleaned Cu (111) substrate is shown in Fig. 3.4 a) during annealing, but before oxygen exposure. Fig. 3.4 b), c) and d) show the emergence of ceria particles to the surface after an oxygen pressure of 5×10^{-7} mbar is introduced at 600 °C.

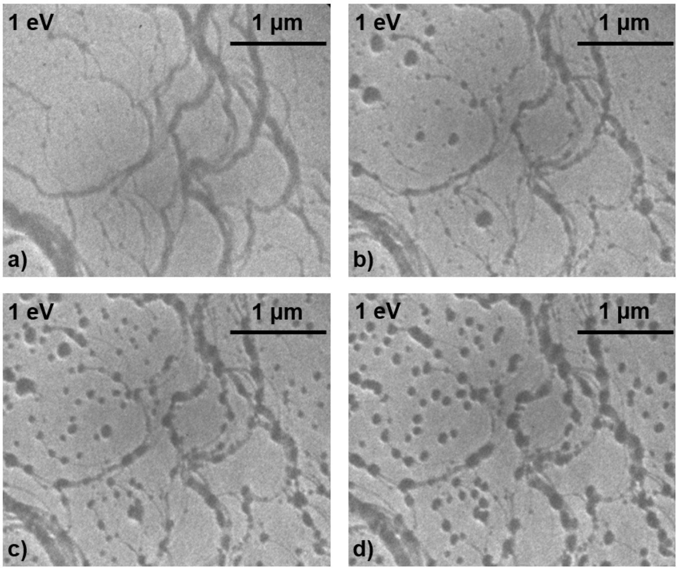

Fig. 3.4: LEEM: Incompletely cleaned Cu (111) substrate during annealing and exposure to oxygen: a) before oxygen exposure, no change occurs during heating, b) - d) after 1 min, 2 min and 3 min in 5×10^{-7} mbar of oxygen.

Even if the Cu surface is seemingly clean after sputtering as depicted in Fig. 3.5 a), it is possible that cerium oxide is still stored inside the crystal and segregates to the surface during annealing in oxygen. Fig. 3.5 b) and c) give two examples for this effect imaged at LEEM start energies of 1 eV and 9 eV. At 1 eV, emerging cerium oxide can be seen to decorate terraces that appeared during the annealing before oxygen exposure. At 9 eV, the cerium oxide is imaged with a bright contrast. It becomes visible that the cerium oxide from the crystal bulk can form small islands on the surface. Repeated cycles of sputtering and annealing in oxygen are necessary to gradually deplete the cerium oxide stored in the crystal bulk and to obtain the required clean surface.

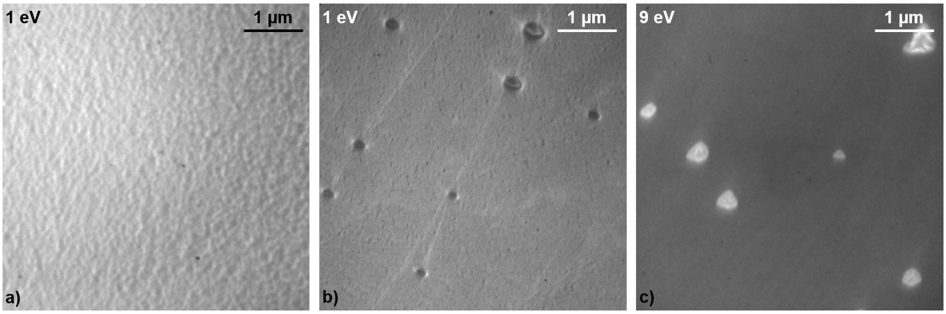

Fig. 3.5: LEEM: Ceria segregating to the surface from the bulk of the seemingly clean crystal: a) after sputtering, b) and c) after oxygen exposure during annealing.

3.1.2 Simultaneous growth of (111) and (100) cerium oxide islands

In order to directly compare the reduction behavior of the (111) and (100) surfaces of ceria, micrometer sized islands of both orientations are grown in parallel and in the immediate vicinity of each other. This allows for both surface orientations to be observed under the same conditions. The simultaneous growth of CeO_2 (111) and (100) islands on Cu (111) can be achieved by adjusting the Ce to oxygen ratio used for the growth, which is a method only recently discovered [30]. The Ce to oxygen ratio can be controlled by the used oxygen pressure and the Ce evaporation flux. With a Ce deposition rate of 0.2 Å per minute at an oxygen pressure of 5×10^{-7} mbar, the growth produces a mixture of (111) and (100) islands. Using a lower deposition rate or a higher oxygen pressure increases the ratio of (100) islands to (111) islands. The other way around, the ratio of (111) islands increases. Hence, it is also possible to grow exclusively (100) or (111) surface islands [30].

An example of a growth process can be seen in Fig. 3.6, starting with a copper surface, which was cleaned as described in subsection 3.1.1. Immediately after the Ce deposition begins, CeO_2 islands start to nucleate. During the next few minutes, the islands grow laterally and the substrate terraces bend in shape, adapting to the presence of the islands. After about 10 minutes, the islands grow only very little laterally and mainly increase in thickness.

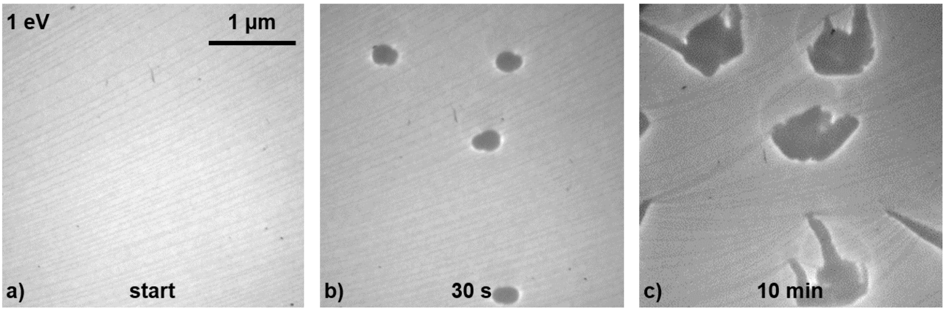

Fig. 3.6: LEEM (1 eV): CeO_2 (100) islands growing on Cu (111): a) clean substrate, b) ceria islands nucleate directly after the Ce deposition begins, c) progress in lateral island growth after 10 minutes. a), b) and c) have the same scaling indicted in a).

The islands grown in Fig. 3.6 are (100) islands, while Fig. 3.7 shows different combinations of (111) and (100) islands. The LEEM imaging of the two CeO_2 orientations is done by adjusting the LEEM start energy in order to obtain the optimal contrast. Fig. 3.7 demonstrates, that (111) and (100) oriented islands have a distinctly different brightness at the same start energy, and that they are each imaged more clearly at different respective start energies.

Methods to precisely and unambiguously identify the island's surface orientation will be discussed in section 3.2.1.

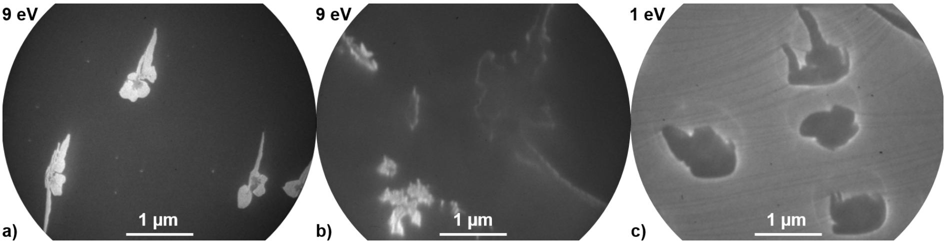

Fig. 3.7: LEEM: CeO_2 islands Cu (111), a) (111) oriented islands, b) islands with (111) and (100) orientation, bright: (111), dark with bright rim: (100), c) islands with (100) orientation.

3.2 Characterization of cerium oxide islands on copper (111)

3.2.1 Surface orientation determination with LEEM and micro-LEED

As shown in Fig. 3.7, the CeO_2 islands' contrast in LEEM images is an option to distinguish their surface orientation. Depending on the LEEM start energy, the two surface orientations show different intensities according to their respective low-energy electron reflectivity. One (111) island surrounded by several (100) islands is depicted in Fig. 3.8 a). With imaging at a LEEM start energy of 9 eV, the (111) island appears clearly brighter than the (100) ones, because the reflectivity in LEEM at a specific electron energy is strongly dependent on the surface orientation. This dependence is caused by the different interplanar distances of the respective surface orientations.

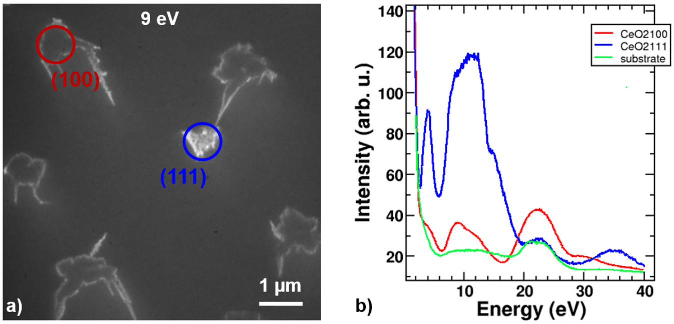

Fig. 3.8: Ceria island reflectivity in LEEM: a) LEEM image of (111) and (100) ceria islands showing a difference in contrast, b) IV-LEEM curves: Intensities of the Cu (111) substrate, the ceria (111) and (100) surfaces over the LEEM start energy, from [87].

The graph in Fig. 3.8 b) depicts so called IV-LEEM curves for which the LEEM images intensities are recorded as a function of the LEEM start energy. The shown curves are the intensities of the Cu (111) substrate and the CeO_2 (111) and (100) surfaces over the LEEM start energy. These different intensities show that the start energy of 9 eV is very suitable to observe and recognize the (111) and (100) islands, because the difference in their brightness is very large and both orientations are brighter than the substrate.

While the contrast in LEEM images is a good indication to identify (111) and (100) islands, the definite determination of their surface orientation is performed with μ-LEED.

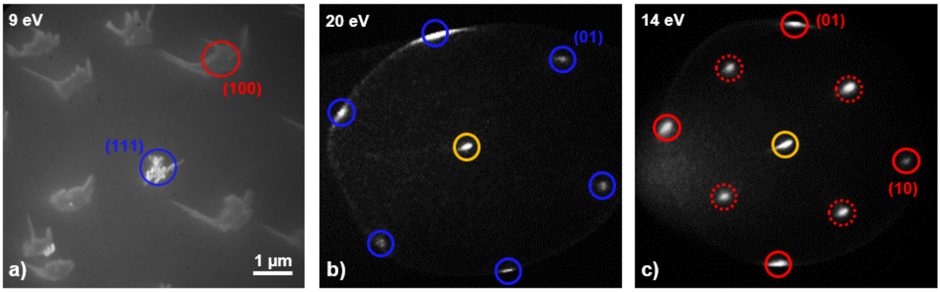

Fig. 3.9: Surface orientation determination by μ-LEED: a) LEEM image of (111) and (100) ceria islands, b) LEED pattern of (111) orientation, obtained from blue marked island in a), c) LEED pattern of (100) orientation, featuring $(\sqrt{2} \times \sqrt{2})$ R45° reconstruction, obtained from red marked island in a). Also in publication [92].

In Fig. 3.9 a), one (111) and one (100) ceria island is marked. Fig. 3.9 b) and c) show the μ-LEED patterns obtained from the islands marked in a), with a hexagonal pattern for the (111) surface and a square pattern with a $(\sqrt{2} \times \sqrt{2})$ R45° reconstruction for the (100) surface. The ceria (100) surface is polar, which leads to surface reconstructions [7]. There are many possible types of reconstructions for the (100) surface. One of the parameters influencing the type of reconstruction is the thickness of the ceria islands, which will be discussed in section 3.2.4.

3.2.2 Effect of growth temperature

While the oxygen pressure and the evaporation rate during the ceria growth determine the ratio of grown (111) and (100) islands (see subsection 3.1.2), the temperature during the growth influences the shape of the islands. The growth process of the ceria islands is limited by the diffusion rate of cerium and oxygen on the Cu surface [93]. Therefore, the ordering of the islands is determined by the kinetics and thus the growth temperature. An increase in the growth temperature brings the islands closer to their shape at thermal equilibrium [94]. Fig. 3.10 a) and b) show LEEM images of two sets of ceria (111) and (100) islands. The used growth temperatures were 450 °C and 500 °C, respectively. The islands grown at 450 °C are irregularly shaped and have rough edges. At 500 °C, the higher mobility of atoms on the surface leads to the formation of islands with much better defined shapes and sharper edges. The island shapes are then either triangular with 60° inner angles in the case of (111) ceria islands, or rectangular with several 90° angles for (100) islands. Their boundaries are thereby following either the three-fold, or four-fold symmetry of the crystal planes of the two types of islands.

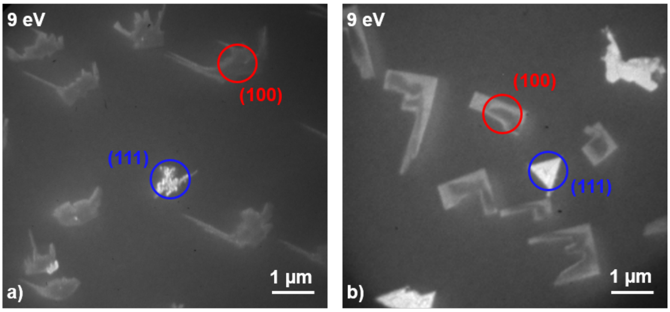

Fig. 3.10: Effect of growth temperature on the island shapes: a) Growth at 450 °C, b) Growth at 500 °C. Also in publication [92].

3.2.3 Oxidation state of grown cerium oxide islands

The oxidation state of the grown ceria islands is probed with X-ray absorption spectroscopy (XAS) at the Ce $M_{4,5}$ edge, which reflects electron transitions of $3d \rightarrow 4f$ levels. Fig. 3.11 a) shows an X-PEEM image of freshly grown ceria (111) and (100) islands taken at the characteristic photon energy of the Ce M_5 peak and Fig. 3.11 b) shows the $M_{4,5}$ spectra of both orientations. The features of the graphs in Fig. 3.11 b) are clearly distinctive for CeO_2 and the Ce^{4+} oxidation state, showing that the islands are fully oxidized and contain almost exclusively Ce^{4+} [95].

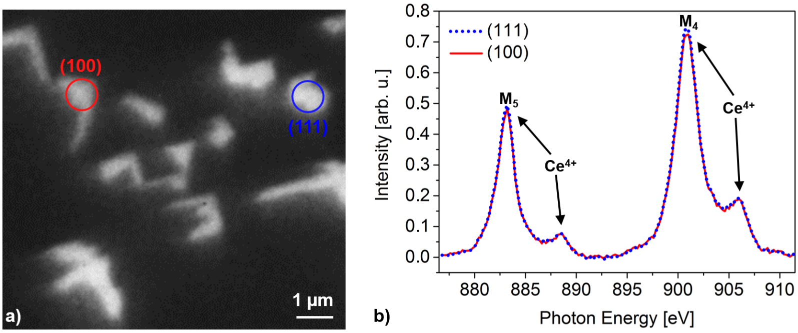

Fig. 3.11: X-Ray absorption at Ce $M_{4,5}$ edge: a) X-PEEM image at Ce M_5 peak (883.4 eV photon energy), b) X-Ray absorption spectra of (111) and (100) CeO_2 islands at Ce $M_{4,5}$ edge.

Due to spin orbit coupling, the CeO_2 spectra have two main peaks at 883.4 eV (M_5 from the $3d_{5/2}$ level) and 900.8 eV (M_4 from the $3d_{3/2}$ level). The main peaks arise from a $4f_0$ initial and $4f_1$ final state of the transition [96]. On the higher energy side of both main peaks, there are satellite peaks with lower intensity which are characteristic for Ce^{4+}. These satellite peaks originate from transitions to $4f$ states in the conduction band and their intensities are related to the delocalization of the $4f$ electrons due to a hybridization between O $2p$ and Ce $4f$ orbitals [97], [98].

3.2.4 Determination of island thickness

The thickness of the prepared ceria islands is estimated by XAS at the Cu L_3 edge ($2p_{3/2} \rightarrow 3d$ transition) which has its peak at a photon energy of 932 eV. By comparing the Cu L_3 edge spectra obtained from the uncovered copper substrate and the substrate underneath the ceria islands, the attenuation of the copper signal is determined. The Cu signal attenuation in combination with the electron inelastic mean free path (IMFP) can serve to calculate the CeO_2 layer thickness. It needs to be considered though that the measured signal (which is close to TEY) includes secondary electrons. This makes the information depth and the use of the IMFP ambiguous.
Frazer et al. determined an 1/e attenuation length (material thickness with signal attenuation by a factor of 1/e) of 21 Å for TEY measurements at the Cu L_3 peak through an overlayer of Cr [72]. The densities of Cr and ceria are very similar with 7.190 g/cm^3 for Cr and 7.215 g/cm^3 for ceria. The TPP2M method used for IMFP calculations for inelastically scattered electrons gives similar results of 16.3 Å for Cr and 18.5 Å for ceria [70, 99, 100]. The calculation with the TPP2M method includes 6 valence electrons and a band gap energy of 0 eV for metallic Cr and 11 valence electrons and a band gap energy of 3.2 eV for CeO_2.

Due to these findings, it can be assumed that the 1/e length obtained for the TEY signal of the Cu L_3 edge for Cr is also valid for ceria.
With the 1/e length of $\lambda = 21$ Å, the island thickness is calculated using:

$$I(d) = I_0 \cdot \mathrm{e}^{-d/\lambda} \tag{3.1}$$

Here, d is the CeO_2 layer thickness, $I(d)$ is the intensity of the attenuated Cu L_3 signal from underneath the islands and I_0 is the Cu L_3 signal from the uncovered substrate. In Fig. 3.12, 3.13 and 3.14, LEEM images and Cu L_3 spectra of three sets of CeO_2 islands with different thicknesses are shown. In each case the island thickness of both the (111) and (100) oriented islands is determined, showing that there is almost no difference in thickness between the two orientations. For the islands in Fig. 3.12, the thickness is 3.4 Å $\pm$ 0.3 Å or ~1 monolayer, with a monolayer thickness of 3.12 Å for the (111) and 2.71 Å for the (100) orientation [7]; A side-view of the stacking can be seen in Fig. 1.3 in subsection 1.3.1. In Fig. 3.13 the island thickness is 9.0 Å $\pm$ 0.3 Å or ~3 monolayers and in Fig. 3.14 the thickness is 13.3 Å $\pm$ 0.2 Å or ~4 and ~5 monolayers.

For the Cu substrate covered and uncovered by ceria, the character of the Cu L_3 spectrum is identical in shape and mostly of metallic character [101]. The Cu XAS being unaffected by the presence of the ceria islands additionally shows that the interaction between Cu and ceria is not influencing the ceria islands strongly. A very different behavior will be shown in chapter 7, where the formation of crystal-defect induced cerium oxide structures is discussed.

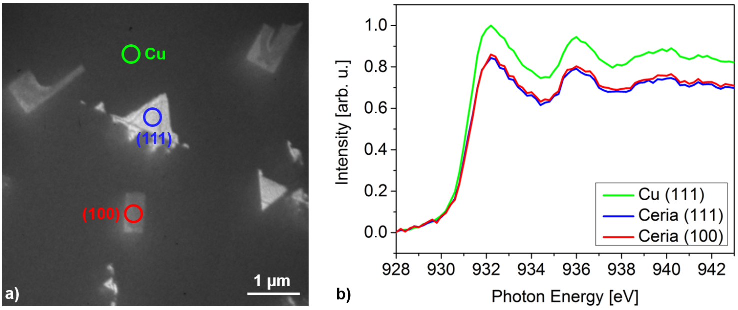

Fig. 3.12: Islands with thickness of 3.5 Å or ~1 ML: a) LEEM image, b) Cu L_3 edge.

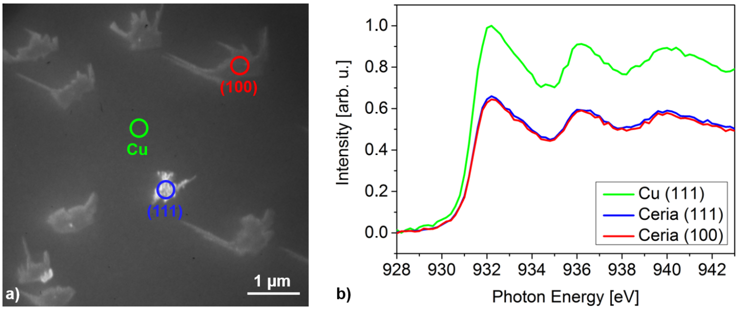

Fig. 3.13: Islands with thickness of 9 Å or ~3 ML: a) LEEM image, b) Cu L_3 edge.

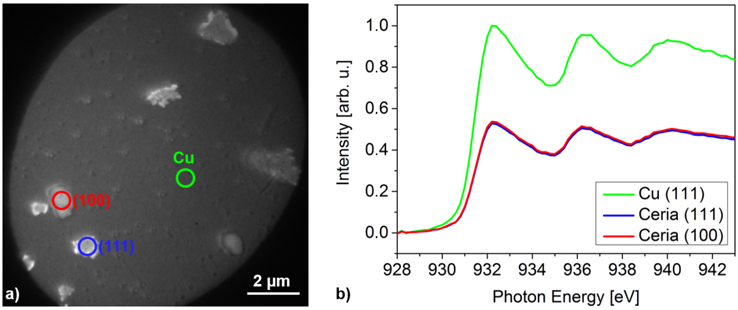

Fig. 3.14: Islands with thickness of 13 Å or 4-5 ML: a) LEEM image, b) Cu L_3 edge.

The difference in island thicknesses has no influence on the LEED pattern of the (111) islands. Independently of their thickness, they show a hexagonal LEED pattern as in Fig. 3.9. On the other hand, the LEED pattern of the (100) islands drastically changes with the thickness, by exhibiting different reconstructions. These changes can be seen in Fig. 3.15: For a thickness of 1 monolayer there is a (1×1) LEED pattern, for 3 monolayers there is a $(\sqrt{2} \times \sqrt{2})$ R45° reconstruction and for 5 monolayers there is a (2 × 2) reconstruction. These three types of reconstructions have already been reported for CeO_2 (100) islands on Cu (111) for island thicknesses of 1, 3 and 10 monolayers [54]. This is in agreement with the island thickness determination, discussed earlier using the attenuation of the Cu L_3 XAS.

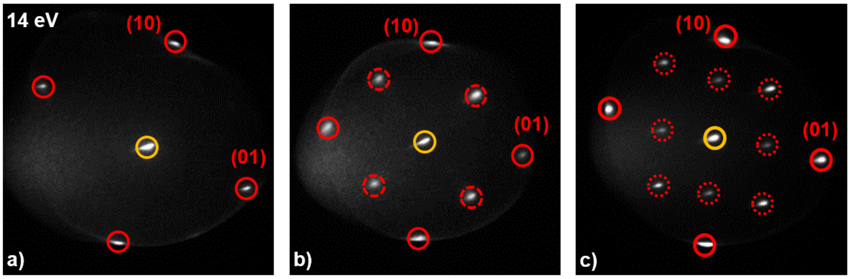

Fig. 3.15: Micro-LEED patterns of ceria (100) islands depending on island thickness: a) (1 × 1) LEED for 1 ML, b) $(\sqrt{2} \times \sqrt{2})$ R45° reconstruction for 3 ML, c) (2 × 2) reconstruction for 5 ML.

3.3 Cerium oxide growth on copper (100)

3.3.1 Copper (100) substrate preparation

Although the preparation procedure for the Cu (100) and (111) substrates is identical (described in subsection 3.1.1), the behavior of the Cu (100) and (111) substrates during annealing in oxygen is different. For the Cu (111), terraces become visible during the heating up to 600 °C and they become smooth and straight during the annealing in oxygen (see Fig. 3.2). For the Cu (100) substrate, terraces also appear during the heating to 600 °C, but upon introduction of 5×10^{-7} mbar of O_2, the terrace boundaries rotate by an angle of 45°. During annealing in oxygen, the terraces also increase in size (from ~50 nm before oxygen to ~500 nm after oxygen exposure), but they do not become fully straight. This development can be seen in Fig. 3.16. Afterwards at temperatures above 400 °C, the step boundary rotation of 45 °Can be observed repeatedly when the oxygen ambient is removed or reintroduced.

The reason for this reorientation lies in the preferred step boundary orientations of the metallic Cu (100) surface and the oxidized surface. For the metallic Cu (100) surface, the prevalent orientation for step boundaries is along the crystalline [011] direction [102]. The exposure of Cu (100) to oxygen at elevated temperatures leads to the formation of Cu_2O and CuO on the surface [103], with a preferred formation of step boundaries along the [001] direction (which is at a 45° angle to the [011] direction) [104]. Studies examining the Cu (100) oxidation, found that for temperatures in the range of 400 °C to 600 °C, as used for this experiment, Cu_2O and CuO become reduced in vacuum [105, 106]. Therefore, the repeatable step boundary rotation of 45° is an indication of the oxidation and reduction of the Cu (100) surface.

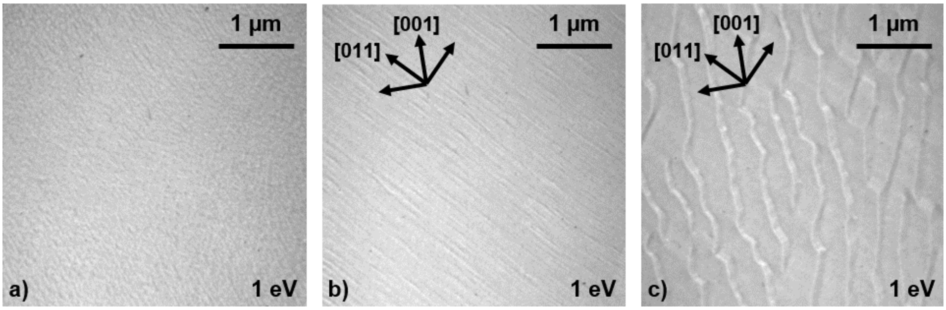

Fig. 3.16: LEEM images of Cu (100) substrate preparation: a) after Ar^+-sputtering, b) heated to 600 °C, c) at 600 °C and in 5×10^{-7} mbar O_2.

3.3.2 Growth of cerium oxide islands on copper (100)

In order to study the temperature dependence of the ceria growth on Cu (100), as done for Cu (111) (subsection 3.2.2), three different growth temperatures were used: 450 °C, 530 °C and 580 °C. All growths were done in an oxygen pressure of 1×10^{-6} mbar. The used Ce deposition rate is similar to the one used for the Cu (111). For each growth, the deposition time was 15 min.

At 450 °C during and after the ceria growth, no visible changes on the Cu (100) surface were observable with LEEM. After the growth, XAS measurements at the Ce M_5 edge showed a uniform distribution of CeO_2 over the surface. Therefore, at this temperature, any grown ceria particles or islands must be too small to be resolved with LEEM or PEEM. The growth process at 530 °C observed with LEEM can be seen in Fig. 3.17.

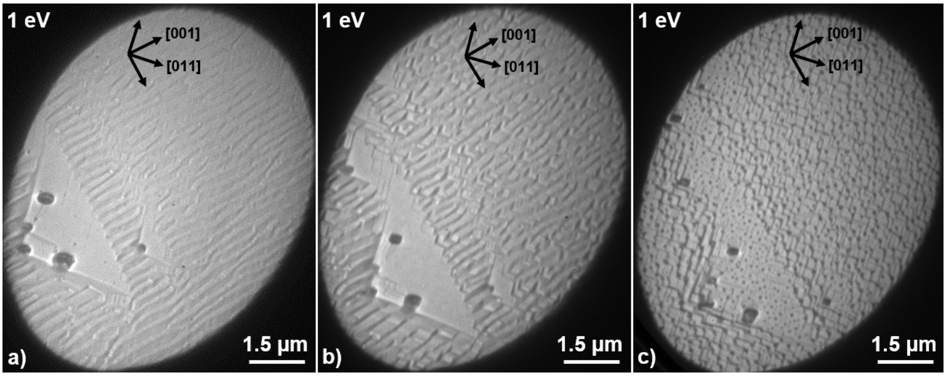

Fig. 3.17: Ceria growth at 530 °C on Cu (100) observed with LEEM: a) start, b) after 5 min, c) after 15 min.

Fig. 3.17 a) shows the Cu (100) substrate before the growth starts. The terraces edges are mostly parallel to each other and oriented along the crystalline [001] direction due to the oxygen ambience of 1×10^{-6} mbar, but some larger terraces (up to some µm in size) are formed by defects on the substrate. These terraces are triangular with a 90° angle and edges along the [011] directions at the corners formed by the defect. Presumably, these terraces were fixated by the presence of the crystal defects, despite the surface oxidation.

In Fig. 3.17 b) one can see the growth proceeding after 5 min. While the ceria islands themselves cannot be directly observed yet, the effect of the ceria island nucleation on the terrace steps is visible. At each nucleation point, the step boundaries split up symmetrically into two new ones forming a 90° angle between them and from then on follow the crystalline [011] direction. Either the presence of the ceria particles induces this step boundary reorientation or, more likely, it is induced by a reduction of the copper surface due to the oxygen uptake of the ceria growth. After 15 min of growth (Fig. 3.17 c) and Fig. 3.18 a)), the terraces have shaped into rectangles with side lengths of a few 100 nm. At one corner of each rectangle there is a small ceria island with an average size of 50 nm.

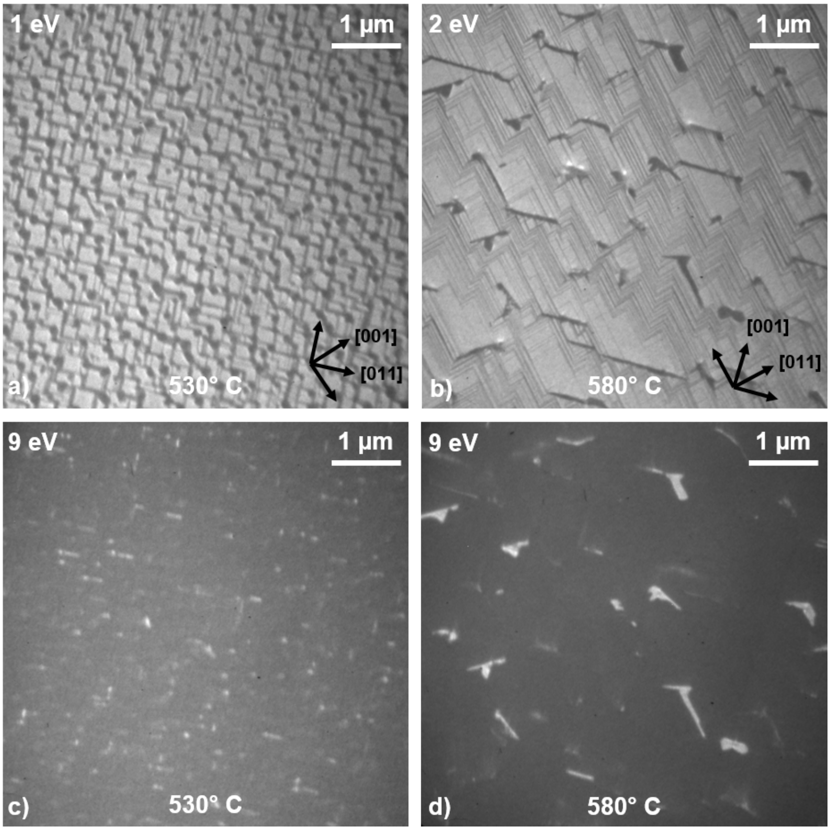

Fig. 3.18: Ceria islands grown at different temperatures: a) islands grown at 530 °C, imaged with LEEM at 1 eV, b) islands grown at 580 °C, imaged with LEEM at 2 eV, c) islands in a) imaged at 9 eV start energy, d) islands in b) imaged at 9 eV start energy.

Growth at an even higher temperature of 580 °C leads to the formation of larger islands, due to the higher diffusion lengths of the oxygen and cerium atoms on the copper surface. A comparison between the islands grown at 530 °C and 580 °C can be seen in Fig. 3.18. For the growth temperature of 580 °C, the substrate terraces also form rectangles, but in this case the boundaries of the ceria islands align either parallel to the rectangular terraces or at a 45° angle with respect to the terrace boundaries (Fig. 3.18 b)) and therefore align either to the [011] or the [001] crystalline directions of the copper substrate.
A closer observation shows that the islands with boundaries oriented in parallel to the copper terraces occur mostly in areas with many step boundaries, while the islands with boundaries oriented at 45° to the copper terraces stretch across larger terraces. This indicates that if step boundaries are present, the ceria islands will adapt their boundaries to them, but on their own they preferably grow along the [001] direction of the copper substrate, which is parallel to the CeO_2 [011] direction. A possible explanation for this could be an effort of the ceria islands to reduce the areas with energetically unfavorable (100) side walls and rather grow along more preferred <110> directions, forming (110) edges.
In Fig. 3.18 c) and d), the islands for both growth temperatures are imaged with a LEEM start energy of 9 eV. This makes the ceria islands themselves visible more clearly, because they show a bright contrast while the substrate becomes dark, due to their respective reflectivities in LEEM (as explained in subsection 3.2.1).

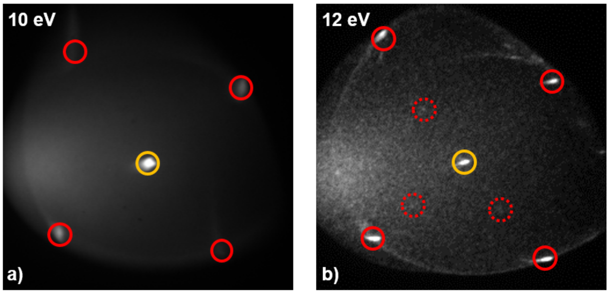

Fig. 3.19: a) LEED pattern of Cu (100) substrate before growth, b) μ-LEED pattern of ceria island grown at 580 °C.

The LEED pattern of the Cu (100) substrate and the μ-LEED pattern of the ceria islands grown at 580 °C are shown in Fig. 3.19 a) and b). The Cu (100) substrate, as expected, shows a square LEED pattern. Because the adsorbed oxygen on the Cu substrate is very mobile at temperatures above 400 °C, the LEED spots are not sharp. The ceria islands also have a square LEED pattern, which is indicated by the additional reconstruction spots in Fig. 3.19 b). This shows that the grown ceria islands have a (100) surface orientation. The LEED spots from the Cu (100) substrate are also visible in the μ-LEED image of the ceria islands, because the islands are to small to be selected exclusively by the smallest available μ-LEED aperture (200 nm).

XAS measurements at the Ce M_5 edge confirm that the islands are fully oxidized CeO_2 for both growth temperatures. Fig. 3.20 a) shows an X-PEEM image of the islands grown at 580 °C, taken at the Ce M_5 peak with a photon energy of 883.4 eV. The curve in Fig. 3.20 b) is a Ce M_5 spectrum of one of the islands in a), showing a Ce^{4+} oxidation state [107].

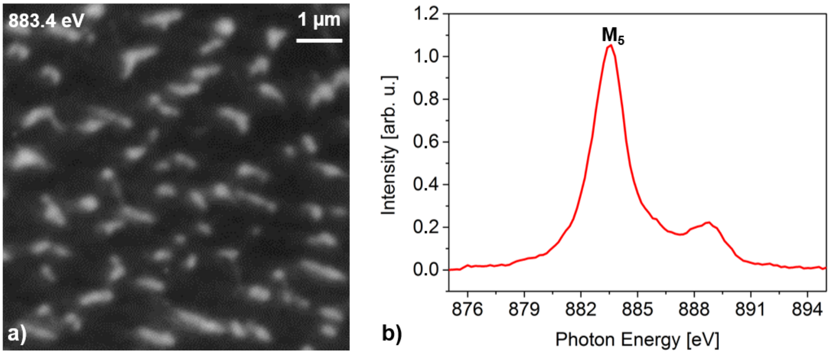

Fig. 3.20: X-Ray absorption at Ce M_5 edge: a) X-PEEM image of CeO_2 islands grown at 580 °C at Ce M_5 peak (883.4 eV photon energy), b) X-Ray absorption spectrum of CeO_2 islands at Ce M_5 edge.

Spectra of the Ce M_5 edge on its own are sufficient to determine the oxidation state of cerium, making it unnecessary to additionally measure the Ce M_4 edge [107]. Consequently, only the Ce M_5 edge will be shown in the following chapters. The photon energy of 883.4 eV will be referred to as the characteristic energy of Ce^{4+} from now on.

4 Cerium oxide island reduction in hydrogen

As explained in chapter 1, the oxygen vacancy formation of ceria is strongly correlated with its catalytic activity for reactions like CO oxidation or NO_x reduction [34]. DFT calculations predict that the oxygen vacancy formation energies for CeO_2 depend on the exposed surface orientation. According to the calculations, the oxygen vacancy formation energy on (100) ceria surfaces is lower than on (111) surfaces [22, 35, 37]. Ceria nanoparticles, structured to expose predominantly (100) surfaces, have shown increased oxygen storage capacity performance and CO oxidation activity [41, 45].

In this chapter, results on the reduction of ceria (111) and (100) islands in a hydrogen atmosphere are presented. The results in sections 4.1 and 4.2 were also submitted for publication in [92]. A mechanism consisting of two steps describes the ceria reduction with hydrogen [108]. First an H_2 molecule interacts with the ceria surface and forms a surface hydroxyl by transferring an electron to the Ce^{4+}, which is thereby reduced to Ce^{3+}. After that an H_2O molecule leaves the ceria surface, which creates an oxygen vacancy (see equation 4.1). A schematic of this process is shown in Fig. 4.1.

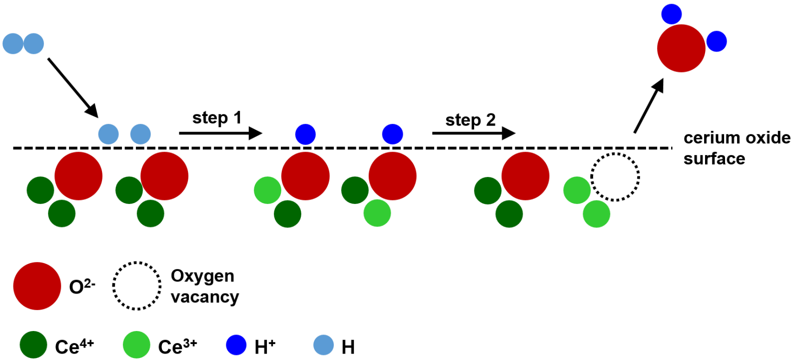

Fig. 4.1: An H_2 molecule adsorbs on the cerium oxide surface, dissociates, forms hydroxyls on the surface and reduces Ce^{4+} to Ce^{3+}. The surface hydroxyls diffuse on the cerium oxide surface and interact to produce H_2O, which desorbs and leaves behind an oxygen vacancy. The figure follows the example in [108].

Because the (111) and (100) islands are prepared directly next to each other, their behavior can be observed at the same time, under identical conditions. An influence of the ceria surface orientation on the reduction behavior is anticipated, due to the calculations by DFT and the promising results shown for nanostructures.

4.1 X-ray absorption measurements of cerium oxide reduction in hydrogen

After the growth of CeO_2 (111) and (100) islands on Cu (111) (described in section 3.1), the oxygen atmosphere was pumped down to 1×10^{-9} mbar and the sample temperature was kept at 430° C. In order to reduce the CeO_2 islands, the sample was then exposed to an atmosphere of 1.5×10^{-6} mbar of H_2 for a prolonged time. The reduction process of the sample was observed with X-PEEM imaging and µ-XAS of the Ce M_5 edge. The characterization of the (111) and (100) islands in Fig. 4.2 is described in section 3.2. Their thickness was found to be ~3 ML. The FOV in Fig. 4.2 a) contains one (111) island in the center, surrounded by several (100) islands. Fig. 4.2 b) and c) show the islands, imaged with X-PEEM at the characteristic energy of Ce^{4+}. After growth (Fig. 4.2 b)), all islands consist of uniformly oxidized Ce^{4+}, which is why all islands in the image have the same brightness. Fig. 4.2 c) shows the same islands after 18 h in hydrogen. The (111) island in the center is visibly brighter than the (100) islands, which indicates a lower Ce^{4+} content of the (100) islands and thereby a stronger reduction of the (100) islands. During the exposure to hydrogen, the ceria islands were partly reduced from Ce^{4+} to Ce^{3+} or from CeO_2 to CeO_{2-x}.

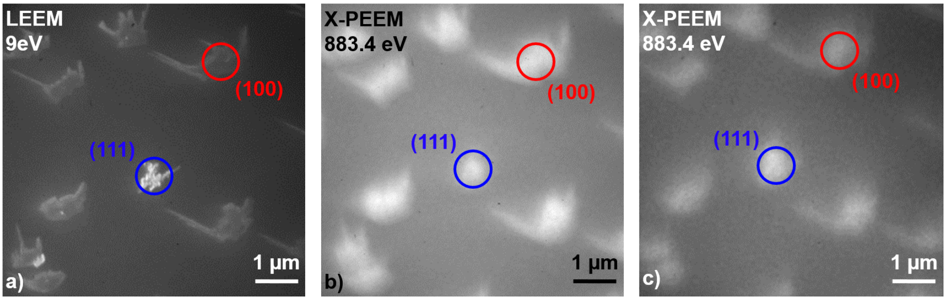

Fig. 4.2: a) LEEM image of ceria (111) and (100) islands after growth, b) X-PEEM image of islands in a) imaged at the characteristic energy of Ce^{4+}, c) X-PEEM image of islands in a) after 18 h in 1.5×10^{-6} mbar H_2 also imaged at the characteristic energy of Ce^{4+}. Also in publication [92].

These changes can be seen very clearly in the Ce M_5 absorption spectra (Fig. 4.3), which are µ-XAS spectra collected from the (111) and (100) islands marked in Fig. 4.2. The spectra in Fig. 4.3 a) to d) were measured after growth and over time in hydrogen. In the initial state shown in Fig. 4.3 a), the (111) and (100) islands are both fully oxidized and their µ-XAS spectra have the shape of Ce^{4+} absorption spectra. The features of the graph were already explained in subsection 3.2.3 and are distinctive for Ce^{4+}. For the spectra measured after hours of hydrogen exposure, an additional shoulder can be seen on the lower energy side of the Ce M_5 edge. This shoulder is resolved into two peaks at 881.2 and 882 eV, which become more pronounced over time, as can be seen in Fig. 4.3 b), c) and d). These additional peaks are distinctive for the formation of Ce^{3+} and thereby distinctive for the reduction of ceria [95, 109]. The Ce^{3+} spectrum features originate from a transition with a $4f^1$ initial and $4f^2$ final state and are resolved into two peaks due to the multiplet structure [95]. From here on, the photon energy of 882 eV will be referred to as the characteristic energy of Ce^{3+}.

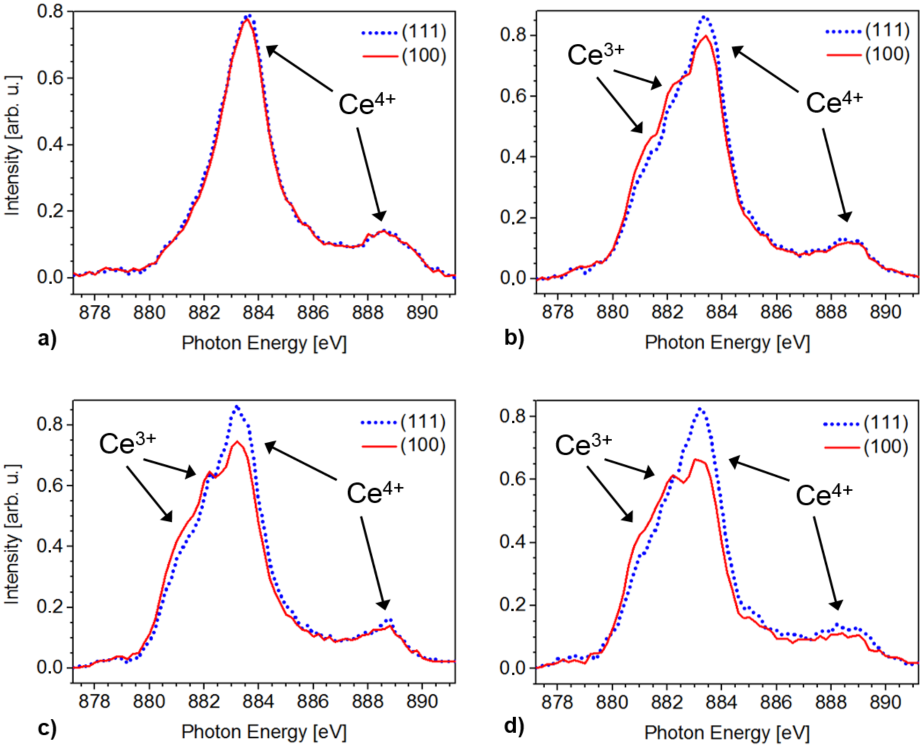

Fig. 4.3: X-ray absoption spectra of ceria islands marked in Fig. 4.2 over time in 1.5×10^{-6} mbar H_2 at 430 °C: a) initial CeO_2 in vacuum, b) after 14.5 h in H_2, c) after 18.5 h, d) after 21.5 h.

Over the whole reduction process, the spectra obtained from the (100) island (red solid lines) reveal a greater degree of reduction than the spectra belonging to the (111) island (blue dotted lines).
Reference spectra for Ce^{4+} and Ce^{3+} XAS, which are shown in Fig. 4.4, were measured on separately prepared samples. The Ce^{4+} reference was obtained from CeO_2 grown on Cu (111) at 500° C in 1.5×10^{-6} mbar O_2 and the Ce^{3+} reference from Ce_2O_3 grown on Nb-doped $SrTiO_3$ (Nb-STO) at 450° C and in 1×10^{-7} mbar O_2. The XAS for Ce_2O_3, indicated by the dotted line in Fig. 4.4, shows exclusively the features of Ce^{3+} [110]. Procedures for the growth of Ce_2O_3 on Nb-STO are not common in literature, but stable Ce_2O_3 layers have been prepared on TiO_2 [111].

The Ce^{4+} to Ce^{3+} ratios of the Ce M_5 edge spectra, measured during the reduction, were determined by using the reference spectra. The experimental XAS data was fitted to a linear combination of the Ce^{4+} and Ce^{3+} reference spectra and the results are the Ce^{4+} and Ce^{3+} contents of the ceria islands. After 23 h in hydrogen the remaining Ce^{4+} contents of the (111) and the (100) islands were 73 % and 62 %, which translates to stoichiometries of $CeO_{1.865}$ and $CeO_{1.81}$, respectively. The difference in reduction, which is visible in the X-PEEM image in Fig. 4.2 c), corresponds to these different remaining Ce^{4+} contents.

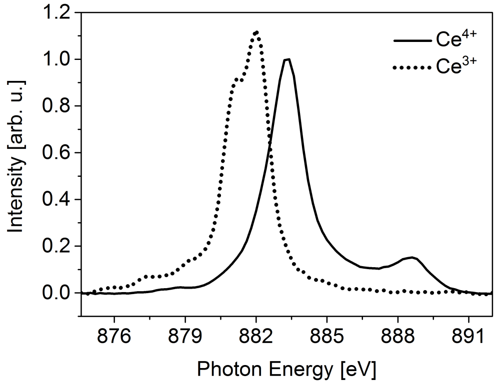

Fig. 4.4: Reference spectra for Ce^{4+} (obtained from CeO_2 grown on Cu (111) at 500 °C in 1.5×10^{-6} mbar O_2) and Ce^{3+} (obtained from Ce_2O_3 grown on Nb-STO at 450 °C and in 1×10^{-7} mbar O_2). Also in publication [92].

4.2 Reduction kinetics of cerium oxide islands in hydrogen

The results of the stoichiometry determination described in section 4.1 are shown in Fig. 4.5. The time evolution of the cerium oxide islands' Ce^{4+} content has a decreasing tendency. As a qualitative evaluation of the reduction process the Ce^{4+} content in the (100) islands (data in red squares) is lower than in the (111) islands (data in blue triangles) at all times. In both cases, the Ce^{4+} content decreases towards an equilibrium, far from the complete reduction of the islands from CeO_2 to Ce_2O_3. In the case of a full reduction to Ce_2O_3, a phase transformation into a cubic bixbyite structure would take place and would lead to significant changes in the µ-LEED patterns [30, 49]. In the case discussed here, these changes in the µ-LEED patterns were not observed. The equilibrium state, which limits the cerium oxide reduction in hydrogen, can be expressed the following way:

$$H_2 + 2\,Ce_{Ce}^{\times} + O_{O}^{\times} \rightleftharpoons 2\,Ce_{Ce}' + H_2O + V_{O}^{\bullet\bullet} \tag{4.1}$$

The partial reduction, limited to an equilibrium between Ce^{4+} and Ce^{3+} content, is in agreement with the findings of Sayle et al. [112], who performed molecular dynamics simulations of cerium oxide nanostructures. In these simulations it becomes energetically more and more difficult to extract further oxygen as the cerium oxide nanocatalyst becomes gradually oxygen depleted. Furthermore, they assert an accordance between the maximal thermodynamically allowed oxygen depletion or reduction and the oxygen storage capacity of ceria.

Having information on the step-wise change of the Ce^{4+} and Ce^{3+} contents over time, makes it possible to evaluate the kinetics of the reduction process for both surface orientations. The cerium oxide reduction rate is limited by the electron transfer between H_2 and cerium oxide [113], and can be described by first order kinetics [114].

Generally (with first order kinetics), the equilibrium between two species A and B with the two respective concentrations [A] and [B], connected by a forwards and a backwards reaction with the respective kinetic rates k_f and k_b, is expressed by:

$$\mathrm{A} \rightleftharpoons \mathrm{B} \tag{4.2}$$

In the following, $[\mathrm{A}]_t$ and $[\mathrm{B}]_t$ are the concentrations of [A] and [B] at a time t, $[\mathrm{A}]_0$ and $[\mathrm{B}]_0$ are the concentrations at $t = 0$ and the concentrations at equilibrium are $[\mathrm{A}]_\infty$ and $[\mathrm{B}]_\infty$.

The rate equation for the concentration [A] is given by:

$$-\frac{d[\mathrm{A}]}{dt} = k_\mathrm{f}\,[\mathrm{A}]_t - k_\mathrm{b}\,[\mathrm{B}]_t \tag{4.3}$$

The solution of the rate equations for [A] and [B] leads to the following expressions:

$$[\mathrm{A}]_t = [\mathrm{A}]_0\,\frac{1}{k_\mathrm{f}+k_\mathrm{b}}\,\left(k_\mathrm{b} + k_\mathrm{f}\,\mathrm{e}^{-(k_\mathrm{f}+k_\mathrm{b})t}\right) + [\mathrm{B}]_0\,\frac{k_\mathrm{b}}{k_\mathrm{f}+k_\mathrm{b}}\,\left(1 - \mathrm{e}^{-(k_\mathrm{f}+k_\mathrm{b})t}\right) \tag{4.4}$$

$$[\mathrm{B}]_t = [\mathrm{A}]_0\,\frac{k_\mathrm{f}}{k_\mathrm{f}+k_\mathrm{b}}\,\left(1 - \mathrm{e}^{-(k_\mathrm{f}+k_\mathrm{b})t}\right) + [\mathrm{B}]_0\,\frac{1}{k_\mathrm{f}+k_\mathrm{b}}\,\left(k_\mathrm{f} + k_\mathrm{b}\,\mathrm{e}^{-(k_\mathrm{f}+k_\mathrm{b})t}\right) \tag{4.5}$$

These expressions can be applied for the Ce^{4+} and Ce^{3+} concentrations with:

$$[\mathrm{Ce}^{4+}]_t = [\mathrm{A}]_t \;\text{ and }\; [\mathrm{Ce}^{3+}]_t = [\mathrm{B}]_t \tag{4.6}$$

and with the following boundary condition, which is valid due to the applied normalization of the Ce^{4+} and Ce^{3+} concentrations:

$$[\mathrm{Ce}^{4+}]_t + [\mathrm{Ce}^{3+}]_t = [\mathrm{A}]_t + [\mathrm{B}]_t = 1 \tag{4.7}$$

In the following $C(t) = [\mathrm{Ce}^{4+}]_t$ is the time dependence of the Ce^{4+} concentration. $C_0 = [\mathrm{Ce}^{4+}]_0$ and $C_\infty = [\mathrm{Ce}^{4+}]_\infty$ are the Ce^{4+} concentrations at the the beginning of the reduction process and at the end in the equilibrium state. As a consequence of equation 4.3 at equilibrium $\left(\frac{d[\mathrm{A}]}{dt} = 0\right)$, C_∞ is given by:

$$C_\infty = \frac{k_\mathrm{b}}{k_\mathrm{f}+k_\mathrm{b}} \tag{4.8}$$

The total rate constant is defined as $k = k_\mathrm{f} + k_\mathrm{b}$ (with the forwards and backwards reactions as reduction: $Ce^{4+} \rightarrow Ce^{3+}$ and oxidation: $Ce^{3+} \rightarrow Ce^{4+}$).

The time dependence $C(t) = [\mathrm{Ce}^{4+}]_t$ of the Ce^{4+} concentration is thereby given as follows:

$$C(t) = (1 - \mathrm{e}^{-kt})(C_\infty - C_0) + C_0 \tag{4.9}$$

Repeated reduction experiments consistently led to the observation of a ~2h delay between the hydrogen exposure start and the onset of the reduction process. This delay can be seen in Fig. 4.5 and also later in Fig. 4.8 in section 4.3. The reason for this delay is a cerium oxide reoxidation by oxygen spillover from the adsorbed oxygen over-layer on the Cu (111) substrate. An effect like this has been observed before for ceria grown on a Rh (111) substrate [52]. In that case, very thin (0.5 ML) ceria (111) islands were reduced by extended exposure to high intensity X-rays (120.8 eV). At an elevated temperature of 475 K the ceria islands could be completely reoxidized twice by the oxygen over-layer from the substrate. This means that only after the oxygen over-layer on the substrate is depleted, the ceria reduction becomes visible.

For this reason, an incubation time t_i between the introduction of the hydrogen atmosphere and the start of the ceria reduction is introduced, which changes equation 4.9 to:

$$C(t) = (1 - \mathrm{e}^{-k(t-t_i)})(C_\infty - C_0) + C_0 \tag{4.10}$$

The model described by equation 4.10 is then fitted to the data of the Ce^{4+} concentrations over time. Two different fitting options are used: The first option assumes an immediate begin of the ceria reduction in hydrogen ambience (incubation time $t_i = 0$) and the second option includes the incubation time of 2 hours ($t_i = 2h$). It is possible to gain kinetic (rate constant k) and thermodynamic (Ce^{4+} content in equilibrium C_∞) information by this fitting. The corresponding fitting curves for both options are shown as solid lines in Fig. 4.5 a) and b) together with the data points. The resulting parameters are displayed in Tab. 4.1. It is not surprising that, considering the fitting results and errors, the second model, which includes the incubation time, describes the system much more accurately and realistically. Therefore the following discussion focuses on the results including $t_i = 2\mathrm{h}$ in the calculations.

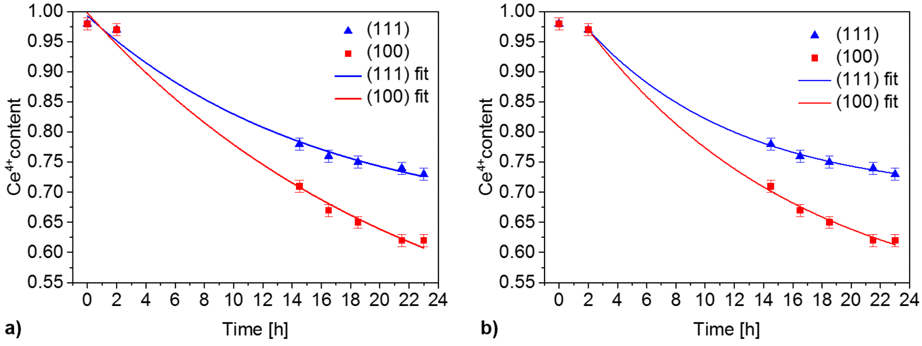

Fig. 4.5: Ce^{4+} content of ceria islands over time in hydrogen and fit functions for (111) and (100) islands, a) fit for immediate reduction, b) fit for delayed reduction onset, also in publication [92]. Results for both in Tab. 4.1.

Kinetic information: The obtained rate constant values for the (111) and (100) islands are $k_{111} = 0.096 \pm 0.008\,\mathrm{h}^{-1}$ ($2.67\,\mathrm{x}\,10^{-5}\,\mathrm{s}^{-1} \pm 2.2\,\mathrm{x}\,10^{-6}\,\mathrm{s}^{-1}$) and $k_{100} = 0.067 \pm 0.012\,\mathrm{h}^{-1}$ ($1.86\,\mathrm{x}\,10^{-5}\,\mathrm{s}^{-1} \pm 3.3\,\mathrm{x}\,10^{-6}\,\mathrm{s}^{-1}$), respectively. For polycrystalline ceria samples a value of $k = 1.5\,\mathrm{x}\,10^{-5}\,\mathrm{s}^{-1}$ has been found [115], which is not far from the values determined here. The rate constant can also be converted to the characteristic time constant $t = 1/k$ with $t_{111} = 10.42\,\mathrm{h} \pm 0.87\,\mathrm{h}$ and $t_{100} = 14.93\,\mathrm{h} \pm 2.67\,\mathrm{h}$. In both cases the time scale for the reduction process is tens of hours, and the (111) surface reaches the equilibrium reduction state earlier than the (100) surface. The rate constant for both the (111) and (100) surfaces are therefore similar to the value for an ill-defined surface composed of a mixture of surface orientations [115]. These facts reveal that for the reduction reaction, the surface exchange rate is not the reason for the stronger reduction of the ceria (100) islands.

Thermodynamic information: Unlike for the kinetic rates, there is a notable difference between the C_∞ parameters for the two surface orientations. The two types of islands have equilibrium values of $C_\infty^{111} = 0.695 \pm 0.009$ for the (111) islands and $C_\infty^{100} = 0.497 \pm 0.044$ for the (100) islands. The Ce^{4+} concentrations for the two equilibrium values show a reasonable degree of reduction compared to surface Ce^{4+} concentrations reported before [108, 116]. The clear difference between the two equilibrium values shows that there is a remarkable difference in reducibility for the (111) and (100) surface. Temperature dependent data of the ceria reduction unfortunately could not be collected due to the very limited temperature range for the reduction experiment. At temperatures lower than 430° C, the ceria reduction cannot be initiated, due to the activation energy barrier for the necessary formation of surface hydroxyls [50, 117], and at higher temperatures, the ceria islands become structurally unstable. Without the thermochemical data, a precise quantification of the reduction energetics is not possible. Instead, an approximate assessment of the difference in energetics for the two surface orientations can still further the understanding of the underlying thermodynamics. For the reduction reaction in equation 4.1, the equilibrium constant K is composed of the respective concentrations:

$$K = \frac{\mathrm{pH_2O}\,[\mathrm{Ce}'_{\mathrm{Ce}}]^2\,[\mathrm{V}_{\mathrm{O}}^{\bullet\bullet}]}{\mathrm{pH_2}\,[\mathrm{Ce}_{\mathrm{Ce}}^{\times}]^2\,[\mathrm{O}_{\mathrm{O}}^{\times}]} \tag{4.11}$$

The equilibrium constant K is related to the Gibbs free energies ΔG as follows:

$$\Delta G = -k_B\,T\ln(K) \tag{4.12}$$

The cation and anion lattices are presumed to be charge neutral and the H_2O and H_2 partial pressures are each considered constant in time and equal for both islands' populations. This makes the Ce^{4+} concentration equilibrium values C_∞ for the two surface terminations the only independent variables.

With the Ce^{4+} concentration:

$$C_\infty = [\mathrm{Ce}^{4+}] = [\mathrm{Ce}_{\mathrm{Ce}}^{\times}] = 2\,[\mathrm{O}_{\mathrm{O}}^{\times}] \tag{4.13}$$

the Ce^{3+} concentration:

$$[\mathrm{Ce}^{3+}] = [\mathrm{Ce}'_{\mathrm{Ce}}] = 2\,[\mathrm{V}_{\mathrm{O}}^{\bullet\bullet}] \tag{4.14}$$

and with:

$$[\mathrm{Ce}^{4+}] + [\mathrm{Ce}^{3+}] = [\mathrm{Ce}_{\mathrm{Ce}}^{\times}] + [\mathrm{Ce}'_{\mathrm{Ce}}] = 1 \tag{4.15}$$

the equilibrium constant K becomes simplified to:

$$K = \frac{\frac{1}{2}(1 - [\mathrm{Ce}^{4+}])^3}{\frac{1}{2}\,[\mathrm{Ce}^{4+}]^{\,3}} \tag{4.16}$$

When the equations 4.11 and 4.12 are used with the obtained C_∞ values for the (111) and (100) surfaces, the difference of the free Gibbs energies can be calculated as $\Delta G_{111} - \Delta G_{100} = 0.15$ eV. Nolan et al. determined oxygen vacancy formation energies by DFT for the ceria (111) and (100) surfaces [37]. In this theoretical work the resulting difference is 0.33 eV. Thus, the values obtained experimentally and from theory are adequately close to each other. This comparison serves as a guideline to confirm the reasonability of the determined values, even though entropy, surface reconstructions or space charge layer formations, as well as the finite probing depth and thickness are not considered.

The results show that the surface orientation does have an impact on the reduction behavior of the ceria islands, as the (100) islands become more reduced than the (111) islands, in accordance with the initial proposition in 1.3.2. Remarkably, the kinetics of the ceria reduction for the (111) and (100) surfaces are found to be almost the same. Instead, the greater reduction of the (100) oriented islands is caused by the overall higher reducibility of the ceria (100) surface. This shows that the essential difference between the two surface terminations originates from the thermodynamics and not the kinetics. The ceria islands' reducibility is limited by the energetics, which are responsible for the Ce^{4+} equilibrium levels. This limited reducibility supports the concept that the gradual oxygen depletion increases the energy needed to continue extracting oxygen from ceria, and that the consequence is a lower activity towards oxidative catalysis [112].

Fit option 1: Immediate reduction			**Fit option 2: Delayed reduction**		
	(111)	**(100)**		**(111)**	**(100)**
k [1/h]	0.063 ± 0.024	0.044 ± 0.021	k [1/h]	0.096 ± 0.008	0.067 ± 0.012
C_0	0.993 ± 0.011	0.998 ± 0.014	C_0	0.970 ± 0.003	0.970 ± 0.008
C_∞	0.645 ± 0.066	0.386 ± 0.175	C_∞	0.695 ± 0.009	0.497 ± 0.044

Tab. 4.1: Results for fitting curves in Fig. 4.5.

4.3 Reduction of cerium oxide islands with higher thickness

The reduction experiment discussed in section 4.1 and 4.2 was done with ~3 ML thick islands. The same experiment was also performed for islands with a thickness of 4 - 5 ML. In Fig. 4.6 a) and b), a group of (111) and (100) CeO_2 islands is imaged with LEEM, and with X-PEEM at the characteristic energy for Ce^{4+}. The surface orientations of the two types of islands were again determined by μ-LEED. The thickness of these islands was determined in subsection 3.2.4.

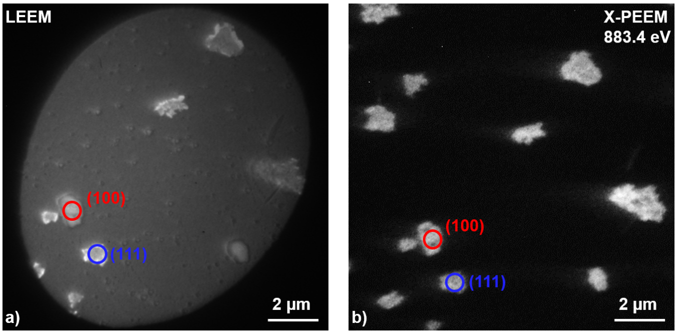

Fig. 4.6: a) LEEM image of ceria (111) and (100) islands after growth, b) X-PEEM image of islands in a) imaged at characteristic energy for Ce^{4+}.

The parameters used for the reduction experiment were again a temperature of 430 °C and a hydrogen pressure of 1.5×10^{-6} mbar. Fig. 4.7 shows Ce M_5 X-ray absorption spectra of the (111) and (100) islands marked in Fig. 4.6 before and during the time in hydrogen. Immediately after growth, the ceria islands are almost fully oxidized, as can be seen in Fig. 4.7 a). Over time in hydrogen, the XAS spectra develop the distinctive shoulders on the lower energy side, which are indicative for Ce^{3+}, as was discussed in section 4.1. Because the Ce^{3+} shoulders are more pronounced for the (100) island, the spectra in Fig. 4.7 b) to d) directly show, that also in this case the (100) islands become more reduced than the (111) islands.

The procedure described in section 4.1 was used again to determine the stoichiometry of the cerium oxide islands during their reduction. The results for the Ce^{4+} content of the (111) and (100) islands as a function of time in hydrogen are shown in Fig. 4.8. Once more, it is noticeable that there is an incubation time of ~2 h before the onset of the ceria reduction. A remarkable common feature in behavior for the thinner and the thicker sets of islands is the limitation of the reduction process by arriving at an equilibrium Ce^{4+} concentration after extended time in hydrogen. The model in equation 4.9, which describes the Ce^{4+} concentration $C(t)$ in dependence of time in hydrogen by first order kinetics, is also applied here to obtain the rate constant k and the equilibrium level C_∞ for the two ceria orientations. As it has been already shown in section 4.2 that the model including the incubation time t_i =2 h gives more accurate results, only this approach is used this time.

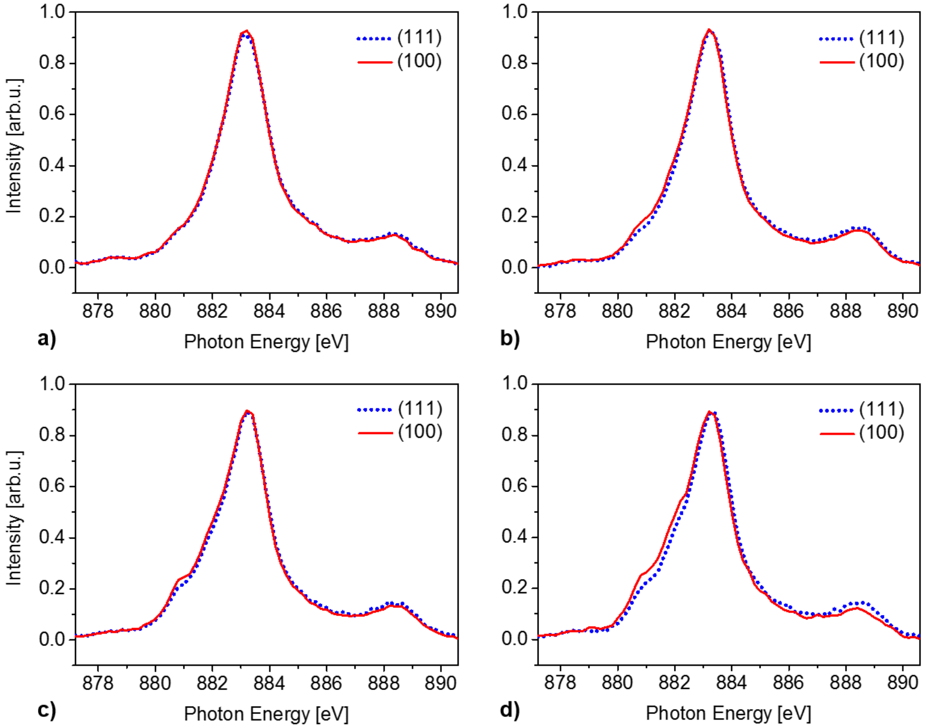

Fig. 4.7: X-ray absoption spectra of ceria islands marked in Fig. 4.6 over time in 1.5×10^{-6} mbar H_2 at 430 °C: a) initial CeO_2 in vacuum, b) after 4 h, c) after 6 h, d) after 8 h in hydrogen.

The fitting curves belonging to the (111) and (100) islands are shown in Fig. 4.8 in addition to the data points, and the corresponding values are displayed in Tab. 4.2. This time the obtained rate constant values for the (111) and (100) islands are $k_{111} = 0.334 \pm 0.208\,\mathrm{h}^{-1}$ $(9.28\,\mathrm{x}\,10^{-5}\,\mathrm{s}^{-1} \pm 5.78\,\mathrm{x}\,10^{-5}\,\mathrm{s}^{-1})$ and $k_{100} = 0.353 \pm 0.112\,\mathrm{h}^{-1}$ $(9.81\,\mathrm{x}\,10^{-5}\,\mathrm{s}^{-1} \pm 3.11\,\mathrm{x}\,10^{-5}\,\mathrm{s}^{-1})$. These results show that in this case the rate constants for both surface orientations are the same within the margin of error.

For both surface orientations of the thicker islands, the rate constants are higher than for the thinner islands. However, considering the large margin of error for the kinetic rates of the thicker islands, the values for both sets of islands are still relatively close to each other. An in depth analysis in order to determine the reason for the different kinetic rates for the two sets of islands would be beyond the scope of this thesis.

The equilibrium Ce^{4+} contents for the thicker islands are $C_{\infty}^{111} = 0.860$ for the (111) islands and $C_{\infty}^{100} = 0.810$ for the (100) islands. These equilibrium values confirm the higher reducibility of the (100) terminated islands also for the thicker islands. Here the difference of the free Gibbs energies for the two surface orientations is $\Delta G_{111} - \Delta G_{100} = 0.07$ eV. Moving on to comparing the equilibrium levels C_{∞} of the thicker and the thinner islands shows that the reducibility of the (111) and (100) islands is lower for the thicker islands (for (111): C_∞ values of 0.860 versus 0.695, for (100): C_∞ values of 0.810 versus 0.479).

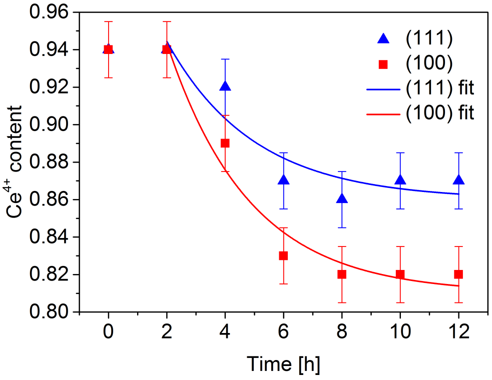

Fig. 4.8: Ce^{4+} content of ceria islands over time in hydrogen and fit functions for (111) and (100) islands for delayed reduction onset, results in Tab. 4.2.

Fitting: **Delayed reduction**		
	(111)	**(100)**
k [1/h]	0.334 ± 0.208	0.353 ± 0.112
C_0	0.944 ± 0.014	0.943 ± 0.012
C_∞	0.860 ± 0.016	0.810 ± 0.013

Tab. 4.2: Results for fitting curves in Fig. 4.8.

One option to explain the lower reducibility of the thicker islands could be that the reduction mainly takes place on the topmost layers of the ceria islands. In that case a higher ceria thickness means a larger number of buried layers which stay oxidized. For the reduction in this experiment a temperature of 430 °C was used. During the reduction oxygen vacancies are created on the ceria surface and the diffusion of oxygen vacancies into lower layers, leading to a bulk reduction, generally only happens at higher temperatures around 830 °C [118]. However, since the thicker islands of 4-5 ML are still very thin, their reduction cannot be compared to a ceria bulk reduction, therefore this is very likely not the sole reason for the different reducibilities of the two sets of ceria islands.

Another plausible explanation are the different shapes of the two sets of islands. As can be seen in Fig. 4.2, the thinner islands have very irregular shapes with dendrite like structures at their edges. The thicker islands shown in Fig. 4.6 are still irregularly shaped, as they do not show the triangular and rectangular shapes of well ordered islands, but their shape is much more compact than the thinner islands' shapes. They do not have dendrite like structures at their edges and their edges are overall more rounded, which makes their perimeter to area ratio smaller. Since the size of the exposed surface area has a large effect on the creation of oxygen vacancies, this explanation for the different levels of reduction for the two sets of ceria islands is also reasonable.

To sum up, for both island thicknesses (~3 ML and 4-5 ML) cerium oxide is reduced in hydrogen until the equilibrium level, which limits the reduction process, is reached. For both island thicknesses, the Ce^{4+} contents at the equilibrium levels are lower for the (100) islands, attesting the higher reducibility of the (100) ceria. Also, in both cases the rate constant shows little to no dependence on the surface orientation. This confirms the conclusions of the first reduction experiment in section 4.2, that the essential difference between the (111) and (100) surface terminations lies not in the kinetcs but in the thermodynamics and in the overall reducibility.

The results of the performed reduction experiments show that more oxygen can leave the (100) oriented ceria surface before it arrives at its reduction limit, which at the same time limits oxidation reactions. At least for very thin ceria films with a thickness of some mono-layers, as used in these experiments, it can be concluded that exposing the ceria (100) surface increases the oxygen storage capacity.

5 Reduction by cerium growth in vacuum

A different method for the ceria island reduction will be presented in this chapter. The prepared CeO_2 islands were reduced by the deposition of metallic cerium in vacuum on top of the original layer. Two different approaches were used for this. In the first one, the sample was kept at elevated temperature after the ceria growth while Ce was evaporated in vacuum. For the second approach, the sample was cooled down to room temperature after the ceria growth and Ce was evaporated in vacuum at room temperature. After the Ce deposition the sample was annealed at 600 °C.

5.1 Reduction by cerium growth in vacuum at elevated temperature

The CeO_2 (111) and (100) islands, shown in Fig. 5.1 a), were grown on Cu (111) at 450 °C and in 5×10^{-7} mbar O_2 with a growth time of 10 min, which is the equivalent to a 2 Å ceria layer on the sample. The identification of the surface orientations was again done with μ-LEED, as described in subsection 3.2.1. Then the oxygen atmosphere was removed by pumping the chamber down to a pressure of 1×10^{-9} mbar while the sample was kept at 450 °C. Using the same deposition rate as for the CeO_2 growth, Ce was evaporated in vacuum on top of the original layer for 105 min, which is equivalent to a layer thickness of 21 Å. In Fig. 5.1 a) the ceria (111) and (100) islands are imaged with LEEM after growth and Fig. 5.1 b) shows the same area of the sample after 105 minutes of Ce deposition in vacuum. Not only do the islands increase in size, Ce deposition between the islands also leads to the formation of new structures, which makes it difficult to recognize the original islands.

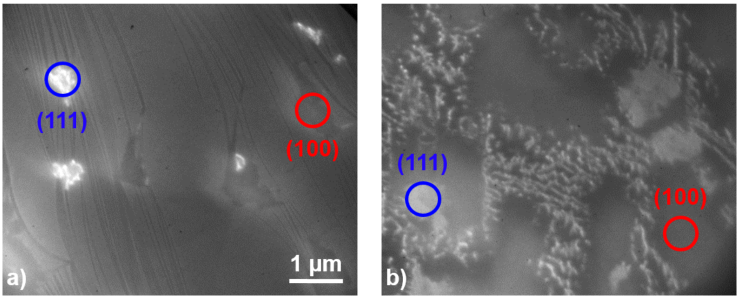

Fig. 5.1: LEEM images (3 eV start energy) of ceria (111) and (100) islands: a) after ceria island growth, b) after 105 min Ce growth in vacuum at 450 °C. a) and b) have the same scale, indicated in a).

During the Ce evaporation a selected ceria (100) island was observed in real-time using µ-LEED. Fig. 5.2 shows the time evolution of the µ-LEED pattern as additional Ce is deposited. At the beginning the µ-LEED pattern shows a $(\sqrt{2} \times \sqrt{2})$ R45° reconstruction. Over the course of 60 minutes, the LEED spots vanish completely. After 100 min a (1 × 1) pattern without reconstructions reappears. This shows, that there are changes in the surface structure, but the cerium oxide island maintains a cubic crystal structure.

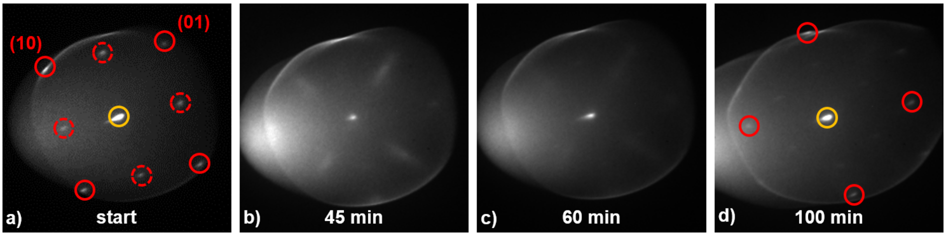

Fig. 5.2: LEED time-lapse sequence recorded at 14 eV start energy during Ce deposition, observed by µ-LEED of one ceria (100) island: a) µ-LEED pattern of ceria (100) island after growth, b) after 45 min Ce growth in vacuum at 450 °C, c) after 60 min, d) after 100 min.

This means, that the cerium oxide island was not fully reduced to Ce_2O_3. While the bixbyte structure for c-Ce_2O_3 is also cubic, its LEED pattern shows destinctive reconstruction spots [30], not visible in Fig. 5.2 d). The loss of the reconstruction spots was observed before for a (100) ceria island on Cu (111) in a similar experiment, after a Ce deposition in vacuum for 124 min [30].

It is also noticeable, that the final LEED pattern is rotated by 45°. This can be explained by a structural change of the island, or by a small drift movement (< 500 nm) of the sample over time caused by a not completely stable sample temperature. Such a drift could lead to the recording of an adjacent facet of the same island. Facets of cerium oxide (100) islands have the same LEED pattern, but it can be oriented at a different angle.

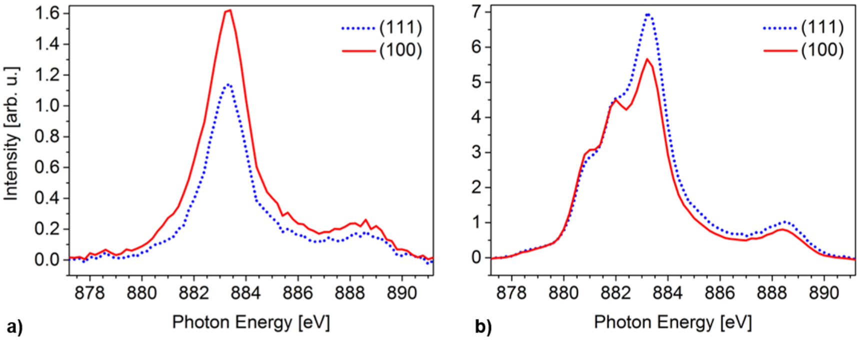

Fig. 5.3: XAS of ceria (111) and (100) islands marked in 5.1 a) after growth, b) after 105 min Ce growth in vacuum at 450 °C.

The reduction occurring on the ceria islands due to the Ce deposition is determined with μ-XAS. Fig. 5.3 shows μ-XAS spectra of the Ce M_5 edge for the (111) and (100) islands marked in 5.1. In the beginning the islands of both orientations are close to fully oxidized with Ce^{4+} contents of 96 % (Fig. 5.3 a)). After 105 minutes of Ce evaporation in vacuum, the (111) island has a Ce^{4+} content of 74 % and the (100) island has a Ce^{4+} content of 69 %.

So also in this case, like for the reduction in hydrogen discussed in chapter 4, the ceria with (100) surface orientation becomes more reduced than the (111) ceria. This difference can be seen in the Ce M_5 spectra in Fig. 5.3 b) by comparing the spectral shapes and the more pronounced Ce^{3+} shoulders at 882 eV and 881.2 eV for the case of (100).

5.2 Reduction by cerium growth in vacuum at room temperature

At the elevated temperature, both the Ce atoms on the sample surface and the oxygen adsorbed on the copper surface are very mobile and seem to have a tendency to build cerium oxide structures anywhere on the sample with only part of it attaching to the already existing ceria islands. This helps to explain why the ceria islands were not completely reduced to Ce^{3+} even though a multitude of the required amount of Ce was added. A second approach for the ceria reduction by Ce growth in vacuum is described here.

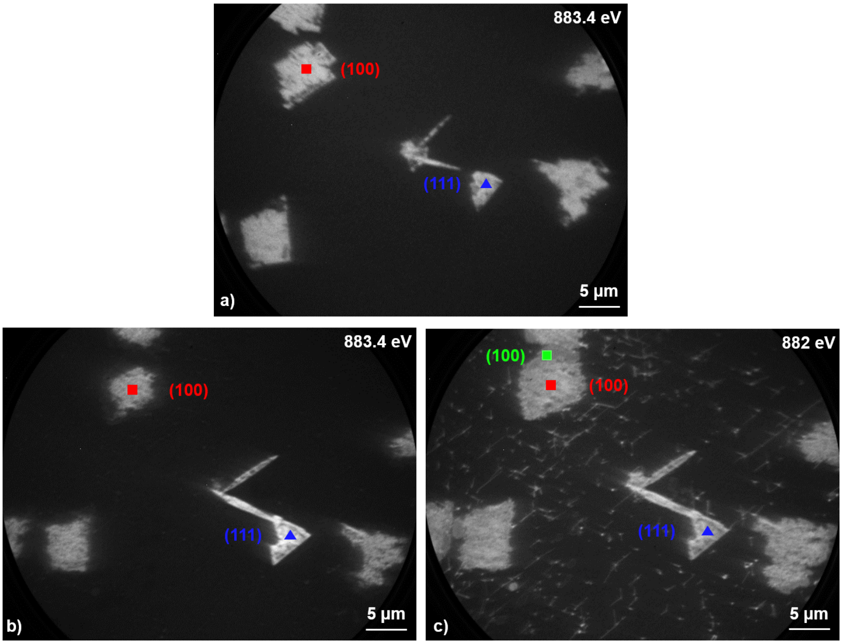

Fig. 5.4: X-PEEM images of ceria (111) and (100) islands at Ce M_5 edge: a) After growth at Ce^{4+} characteristic energy, b) After Ce evaporation in vacuum at room temperature, followed by annealing 600 °C, at Ce^{4+} characteristic energy, c) at Ce^{3+} characteristic energy.

The prepared CeO_2 islands were grown at 500 °C and in 1×10^{-6} mbar partial pressure of O_2, with a growth time of 15 min, equivalent to a ceria layer of 3 Å. The selected field of view in Fig. 5.4 a) contains one (111) oriented island and several (100) oriented islands. The surface orientations were confirmed again by both LEEM at 9 eV starting energy and µ-LEED. In Fig. 5.5 a) µ-XAS attests that the islands are almost fully oxidized CeO_2, with a Ce^{4+} content of 97 %.
After the characterization measurements, the sample was cooled down to room temperature and 2/3 of the initial amount of Ce was evaporated in vacuum (10 min growth time), which is twice the amount ideally necessary to reduce the initial ceria from CeO_2 to Ce_2O_3. Due to the expected oxidation of part of the evaporated Ce by the oxygen adsorbed on the Cu substrate, twice the ideally needed amount of Ce was used to compensate for this effect.
The Ce evaporation was followed by annealing at 600 °C for 30 min and subsequent cool-down to room temperature. Right after the evaporation, the Ce atoms are expected to be distributed randomly over the substrate and the ceria islands. During the annealing the mobility of the Ce increases and the atoms attach to the already existing ceria islands.

The combination of the X-PEEM images taken at the Ce^{4+} and Ce^{3+} characteristic photon energies in Fig. 5.4 b) and c) and the µ-XAS spectra in Fig. 5.5 b) shows the distribution of the reduction:
The (111) island is reduced homogeneously over its surface and retains a Ce^{4+} content of 80 %. The (100) islands become more reduced and show a huge difference in reduction levels between the inside and the border parts of the islands. The insides of the islands have a Ce^{4+} content of 68 % and are surrounded by a rim with a Ce^{4+} content of only 25 %.

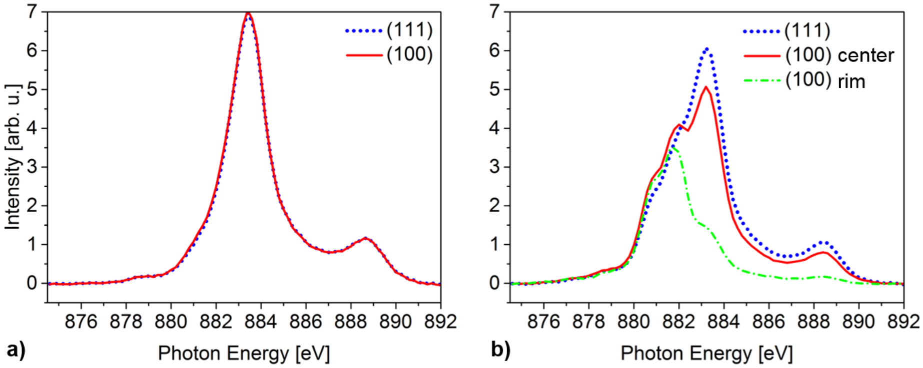

Fig. 5.5: Ce M_5 XAS of (111) and (100) islands market in 5.4 a) after growth, b) After Ce evaporation in vacuum at room temperature, followed by annealing 600 °C.

The UV-PEEM image in Fig. 5.6, shows a dark contrast for the reduced areas of the (100) islands. This dark contrast gives further details of the reduced rims' morphology and reveals a significantly higher work function of the reduced ares, due to one of contrast mechanisms of UV-PEEM, as discussed in section 2.2.3.

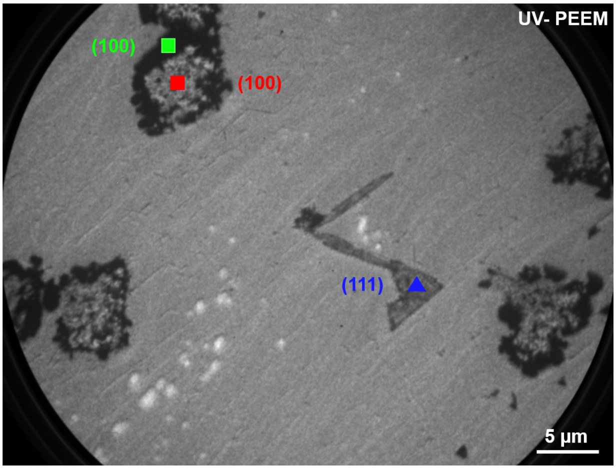

Fig. 5.6: UV-PEEM image after Ce evaporation in vacuum at room temperature, followed by annealing at 600 °C.

It seems plausible that the homogeneous reduction of the (111) island happens due to the Ce deposited on top during the evaporation, when the Ce is still randomly spread. During the subsequent annealing, the mobile Ce preferentially attaches to the (100) islands, making them grow in size laterally and reducing them from the outside. An illustration of this process is depicted in Fig. 5.7. Deposited Ce also begins to accumulate on originally uncovered areas of the substrate between the islands, forming highly reduced objects of a much smaller size (<100 nm) visible in Fig. 5.4 c). However, the amount of cerium oxide structures formed between the original islands is much lower than before, when the Ce was deposited at elevated temperature. Generally, the second method described in this section is more effective at reducing the ceria islands, since for the high temperature deposition more than ten times the amount of Ce was used to achieve a comparable degree of reduction.

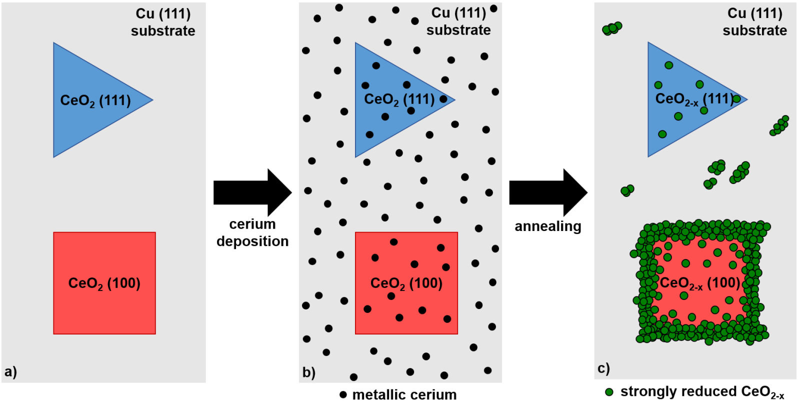

Fig. 5.7: Reduction by deposition of metallic cerium: a) ceria (111) and (100) island after growth, b) Ce deposition in vacuum at room temperature, c) after annealing at 600 °C.

Surprisingly, even for the second method, it appears to be difficult to achieve a higher than the presented degree of reduction. Changes in the reduction by additional Ce evaporation in vacuum and the following annealing were lower than the detection limit. It seems like, after the achieved level of ceria island reduction, additionally evaporated Ce preferentially deposits between the islands or diffuses into the Cu substrate during the annealing. This method was used successfully in another work to transform CeO_2 (111) on Cu (111) to c-C_2O_3 [49], but in that case a continuous CeO_2 (111) was used, which prevents Ce deposition on the substrate. Another possible reason preventing a full reduction to Ce_2O_3, could be a sufficiently high remaining oxygen partial pressure in the chamber, which during the experiment could only be pumped down to $> 1 \times 10^{-9}$ mbar.

To conclude, for both approaches, the interfacial reaction of metallic Ce with ceria yields the same results, which are in agreement with the results of ceria reduction by hydrogen: The (100) islands are reduced more than the (111) islands under the same reaction conditions.

6 Platinum - cerium oxide combination

For many applications of ceria as a catalyst, ceria is used in combination with noble metals, among which platinum is a very common choice [8]. After examining two different methods of ceria island reduction, namely the reduction in hydrogen and the reduction by deposition of metallic Ce discussed in the chapters 4 and 5, the reduction in hydrogen was used for a platinum-ceria combination.

6.1 Preparation and characterization of platinum - cerium oxide combination

CeO_2 islands were prepared at 500 °C and in 1×10^{-6} mbar partial pressure of O_2, with a deposition time of 15 min. The surface orientations of the different islands were again confirmed by the LEEM contrast at 9 eV starting energy and μ-LEED. The sample was cooled down to room temperature and the oxygen atmosphere was removed. Subsequently, a small amount of Pt was deposited on top. Fig. 6.1 a) and b) show two groups of CeO_2 (111) and (100) islands distinguishable by their respective contrasts in LEEM. Interestingly, the ceria islands' surface orientations are also recognizable with UV-PEEM imaging at room temperature.

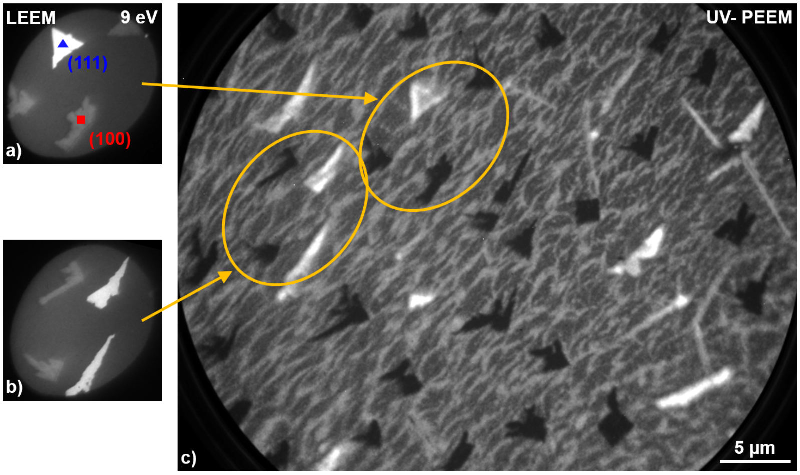

Fig. 6.1: CeO_2 islands with (111) and (100) orientations: Different contrasts for both orientations with LEEM and UV-PEEM. a) and b) LEEM images at 9 eV start energy of two regions, UV-PEEM image including the areas in a) and b). The scale for the LEEM and UV-PEEM images is the same.

In the UV-PEEM image in Fig. 6.1 c) the ceria islands previously imaged by LEEM in a) and b) are marked. One can see that the (111) islands are white, the (100) oriented islands are black and the Cu (111) substrate is grey. For both LEEM and UV-PEEM imaging, the Pt deposition was invisible and the observed contrasts remained unchanged.

These different contrasts in the UV-PEEM image can be linked to different work functions of the ceria (111) and (100) and the Cu (111) surfaces. The work function contrast mechanism for UV-PEEM imaging was explained in subsection 2.2.3. For the same material, different crystal surface orientations can lead to a work function variation of a few 0.1 eV [73]. Only if the excitation photon energy is larger than the work function of the sample, electrons are emitted from the sample and cause image intensity in UV-PEEM. Since the ceria (100) islands appear black in the UV-PEEM image, their work function is too large to be overcome by excitation with the ~4.9 eV of the mercury lamp. Consequently the ceria (100) surface has a higher work function than the ceria (111) surface, which appears white in the UV-PEEM image. The various grey contrasts of the Cu (111) substrate most likely arise from step edges and domains of "29" and "44" oxygen reconstructions that are present on the surface of Cu (111) at room temperature after exposure to oxygen at elevated temperatures [91].

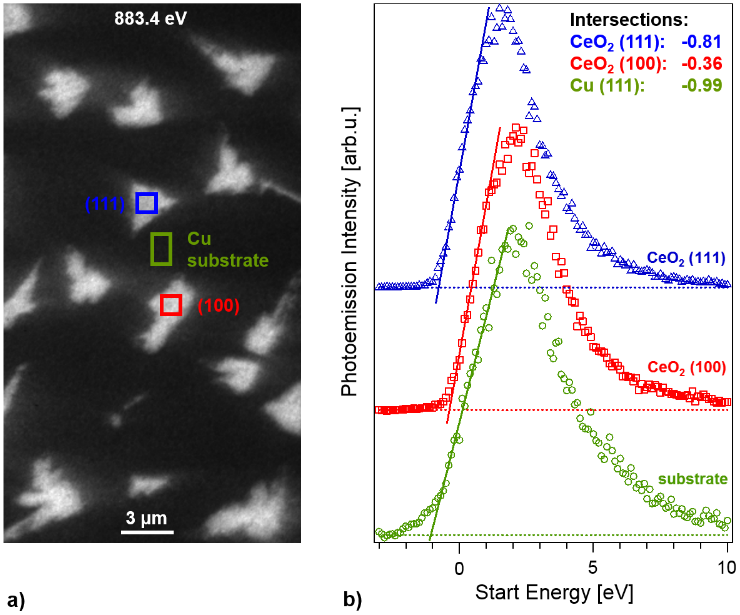

Fig. 6.2: a) CeO_2 (111) and (100) islands imaged with X-PEEM at characteristic energy of Ce^{4+}, b) secondary electron energy distribution for CeO_2 (111) and (100) islands and Cu (111) substrate from positions marked in a).

The differences in work function for ceria (111) and (100) and Cu (111) were determined with X-PEEM (at the characteristic photon energy of Ce^{4+}), by the method introduced in subsection 2.2.4, which uses the energy position of the low kinetic energy cutoff of the secondary electrons. The electron energy distributions measured for the sample regions marked in Fig. 6.2 a), with a variation of the sample potential from -3 to +10 eV, are displayed by the respective curves in Fig. 6.2 b). All three spectra were analyzed by fitting straight lines into their low kinetic energy cutoff, and determining the fitted lines' intersection with the base line of the spectra. The intersection positions are: -0.81 eV for CeO_2 (111), -0.36 eV for CeO_2 (100) and -0.99 eV for the Cu (111) substrate. As already discussed in subsection 2.2.4, these values are not direct determinations of the work functions, but rather determinations of their relative differences. The results show that the work function for the ceria (100) surface is 0.45 eV higher than for the ceria (111) surface. The copper substrate has a lower work function than both ceria orientations.

Because there is no strong X-ray absorption edge of platinum within the available energy range, XAS could not be used to prove the presence of the platinum on the sample. Therefore, Auger electron spectroscopy was employed. The disadvantage of this technique is that the signal is averaged over a large part of the sample, making it impossible to obtain information on the spacial distribution of Pt, but it is sufficient to confirm the presence of Pt on the sample. The first derivative of the Auger spectrum of this sample is shown in Fig. 6.3. A noticeable Pt_{MNN} signal is visible in 6.3 a), while Fig. 6.3 b) and c) show the O_{KLL} and Cu_{LMM} features for comparison. The element specific features of the Auger spectrum were confirmed with reference [85]. The Auger measurements were performed after the reduction and reoxidation experiment discussed in the following section 6.2.

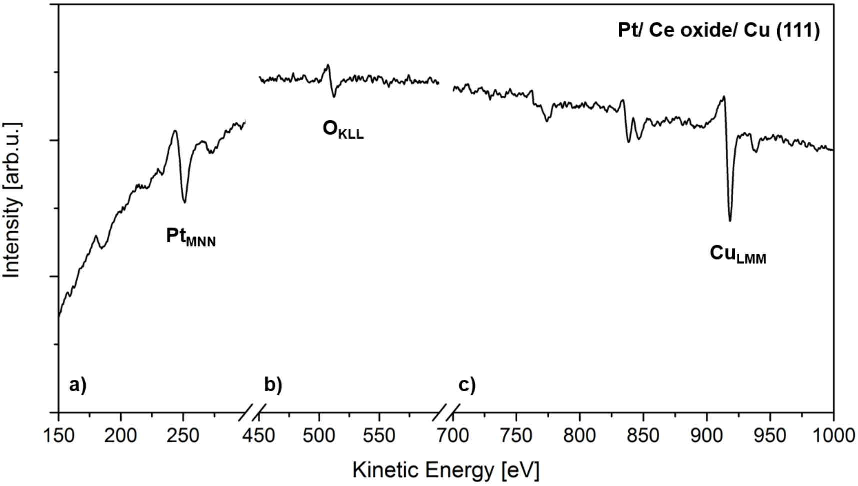

Fig. 6.3: First derivative of Auger electron spectrum for the Cu (111) crystal with the prepared platinum - cerium oxide combination on top: The energy ranges are selected for the identification of features belonging to a) platinum, b) oxygen and c) copper.

6.2 Reduction of platinum - cerium oxide combination in hydrogen

After the Pt deposition at room temperature the sample was heated up to 430 °C and exposed to a hydrogen ambience of 1.5×10^{-6} mbar for 20 h. Fig. 6.4 a) shows ceria islands also depicted in Fig. 6.1, imaged with X-PEEM at the Ce^{4+} characteristic energy, at the start of the hydrogen exposure. µ-XAS at the Ce M_5 edge shown in Fig. 6.6 a), confirms that the ceria islands were close to completely oxidized, with a Ce^{4+} content of 98 %.

In Fig. 6.4 b) and c), the same islands are imaged at the Ce^{4+} and Ce^{3+} characteristic energies after 20 h in hydrogen. Here, there are several observations to be made: Imaging at the Ce^{3+} characteristic energy shows that new, strongly reduced cerium oxide structures have formed, which are decorating the original islands of both orientations. These new decorations can also be seen at the Ce^{4+} characteristic energy, but with very low intensity. Imaging at the Ce^{4+} characteristic energy shows that the original (111) islands stayed the same in shape and size, while the (100) islands became smaller and seem to have lost some of their original area to the decoration structures. A simplified depiction of these two different types of interaction between the decoration structures and the cerium oxide islands can be seen in Fig. 6.5.

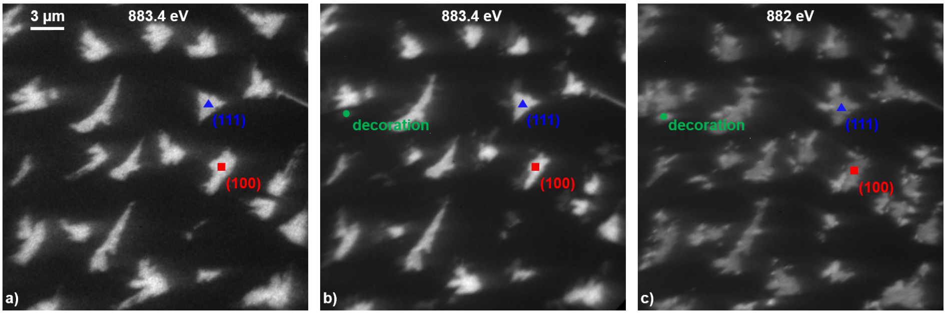

Fig. 6.4: X-PEEM images of cerium oxide islands also shown in Fig. 6.1: a) after CeO_2 island growth and Pt deposition at Ce^{4+} characteristic energy, b) after 20 h in H_2 at Ce^{4+} characteristic energy, c) after 20 h in H_2 at Ce^{3+} characteristic energy. All three images have the same scale, indicated in a).

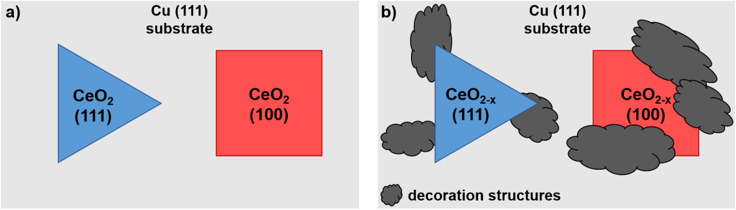

Fig. 6.5: Schematic of decoration structure and cerium oxide island interaction: a) original cerium oxide island, b) islands with decoration structures.

The graph in Fig. 6.6 b) shows µ-XAS curves of the cerium oxide (111) and (100) islands and of the new decoration structures after the reduction in hydrogen. For the (100) islands only the area not covered by the decoration structures was used for µ-XAS. The (100) islands seem to be more affected by the decoration structures, which cover part of their surface. Despite this fact, the reduction levels are very similar for both surface orientations. The remaining Ce^{4+} contents of the (111) and (100) oriented islands are 75 % and 74 %, respectively. The decoration structures are almost completely reduced Ce^{3+} with a remaining Ce^{4+} content of only 5 %. After the reduction experiment in hydrogen, the reoxidation of the cerium oxide islands in an oxygen atmosphere was tested. The spectra in Fig. 6.6 c) show the oxidation effect of 30 min in 1.5×10^{-6} mbar O_2 at 430 °C on the (111) and (100) islands and the decoration structures. The (111) and (100) islands became almost completely reoxidized with Ce^{4+} contents of 92 % and 90 % respectively. Extending the time in oxygen to 3 h did not result in further changes. Most likely, a higher oxygen pressure and different thermal conditions are necessary for further reoxidation. The decoration structures remained in their strongly reduced state, even after the combined 210 min exposure to O_2.

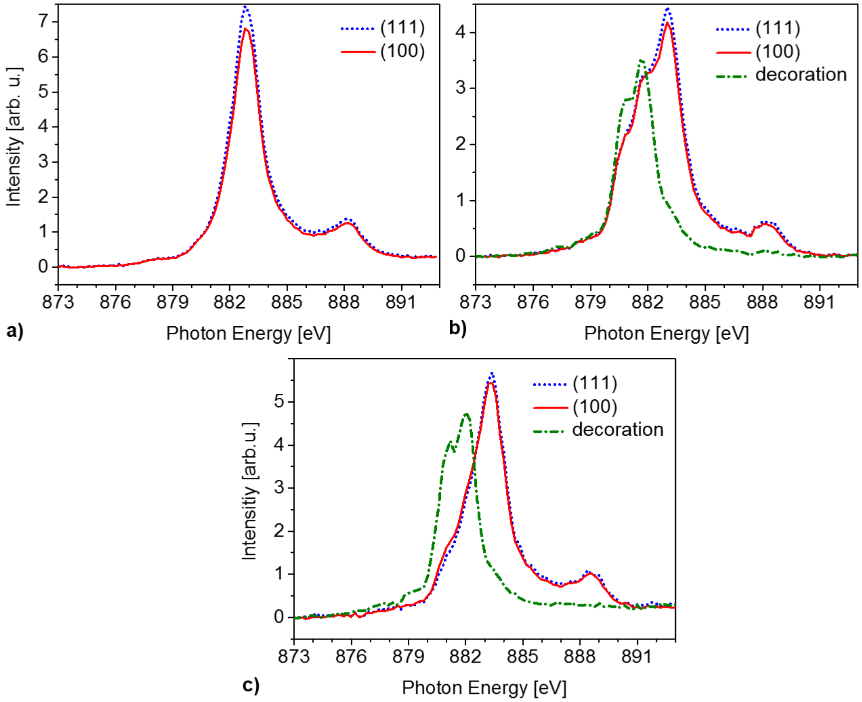

Fig. 6.6: Ce M_5 XAS of ceria islands marked in Fig. 6.4: a) after ceria island growth and Pt deposition, b) after 20 h in $1.5x10^{-6}$ mbar H_2, c) after reoxidation in $1x10^{-6}$ mbar O_2.

In summary, the achieved reduction levels were not significantly different for the (111) and (100) surface orientations upon the reduction of the platinum-ceria combination in hydrogen. New structures, almost exclusively comprising of fully

reduced Ce^{3+} species formed, and decorated the outside borders of the (111) and the (100) islands. Interestingly, only the latter lost part of their original area to the new structures. Even though, the spatial Pt distribution is not obtainable with the present experimental setup, one can propose that the Pt was accumulated in the new structures surrounding the original islands and that the Pt was very likely responsible for the strong reduction of these structures and prohibited their reoxidation.
An STM study examining Pt nanoparticles on CeO_2 (111) thin films on Cu(111) has shown that Pt nanoparticles preferentially attach to CeO_2 terrace edges and to CeO_2 nanoparticles on top of CeO_2 terraces [119]. In the same study, RPES (resonant photoelectron spectroscopy) was used to determine the cerium oxidation state. This showed that at temperatures above 330 °C, a direct contact between Pt and CeO_2 nanostructes leads to a reduction of CeO_2 by oxygen transfer to Pt and the formation of Ce^{3+}. In another work, Pt nanoparticles were prepared on a CeO_2 (111) film [120] and findings for STM/XPS revealed that Ce^{3+} was formed due to charge transfer at the interface of the Pt metal with the cerium oxide support, even without an exchange of oxygen. Yet another STM study on Ag nanoparticles on a CeO_2(111)/ Pt(111) system has demonstrated a preference of Ag nanoparticles to decorate CeO_2 terraces [121].

An evaporation of Pt on top of CeO_2 islands on Cu (111) is therefore very likely to result in Pt decorating the CeO_2 island edges. Presumably in the case of the experiment presented here, the elevated sample temperature enabled part of the cerium oxide to mix with the Pt in the decoration structures over time. This mixing with Pt lead to a much stronger reduction of the cerium oxide, compared to the pure cerium oxide islands' reduction in hydrogen. The observation that the cerium oxide in the decoration structures remained reduced (while the rest of the cerium oxide islands became reoxidized) during the oxygen exposure at the end of the experiment, further points towards a Pt-cerium oxide mixture in the decoration structures. The cerium oxide in the Pt-cerium oxide mixture could be fully oxidized, with respect to its oxygen content, and be only reduced electronically by the charge transfer to Pt, as discussed before. Considering the well-known excellent catalytic properties of Pt, it follows that the decoration structures, consisting of a Pt-cerium oxide combination, form active centers for catalysis on this type of sample.

These results show the importance of microscopic information for the understanding of the concerned Pt-cerium oxide model system. Without the combination of microscopic and chemical information, it would be impossible to detect the formation of the decoration structures and the different cerium oxidation state, exhibited exclusively by these structures. Furthermore, one can observe that the pure cerium oxide (111) islands remained unchanged in their shape, while the (100) islands shrunk and lost parts of their original area to the Pt-cerium oxide mixture. This proves a stronger interaction between Pt and the cerium oxide surface with (100) termination and the edge boundaries of the (100) islands. This also agrees with DFT calculations that predicted the CeO_2 (100) surface to provide adsorption sites for the stable anchoring of atomically dispersed Pt^{2+} ions [122].

7 Effects of substrate defects on cerium oxide growth

In this chapter, the impact of surface defects of copper single crystals will be discussed. The presence of such irregularities induces the growth of large cerium oxide structures with diameters up to several tens of µm and a completely different chemical composition. The growth of theses structures occurred repeatedly alongside the regular, much smaller (111) and (100) ceria islands. With Ce evaporation in an oxygen pressure of 5×10^{-7} mbar, the growth conditions leading to the formation of these structures were the same as described in subsection 3.1.2. The observations on these structures are also published in reference [123].

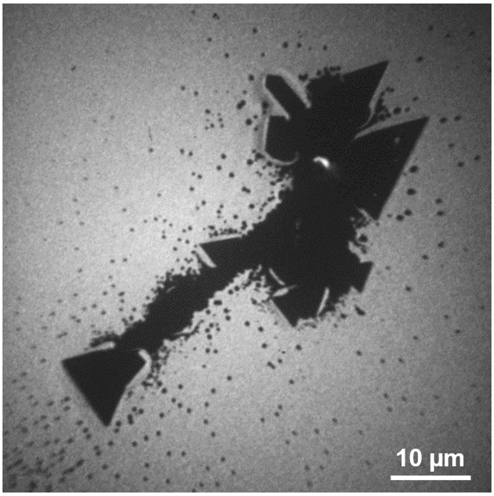

Fig. 7.1: UV-PEEM image of ceria structures, grown induced by copper crystal defects.

An accumulation of triangular structures, nucleated at a Cu (111) crystal defect, can be seen in Fig. 7.1, imaged with UV-PEEM. Similar cerium oxide structures can be seen in the UV-PEEM images in Fig. 7.2 a) and b), grown inside a large crystal defect and between two defects. Another observed configuration is a triangular ceria structure with a defect at the center, as shown in Fig. 7.2 c) and d). The blue arrows in Fig. 7.2 indicate the positions of the crystal defects. Since these objects are relatively large, imaging with UV-PEEM is suitable, because the illumination spots with LEEM and X-Rays are too small to image an entire object of this size. Another advantage of imaging these structures with UV-PEEM is the strong work function contrast of the defect induced structures.

The triangular shape of the structures follows the lattice symmetry of the Cu (111) substrate. The smaller structures surrounding the large triangles are ceria (100) islands, which also cover the rest of the sample. Several Cu (111) single crystals produced by MaTecK, including new crystals and crystals already in use for a few years, were examined for the large, triangular, defect induced structures. The comparison showed that the density of defect induced structures after a ceria growth strongly depends on the quality of the single crystal surface before the growth. Depending on the sample history and the polishing quality, about 0.02 % to 2 % of the sample surface is covered by the defect structures.

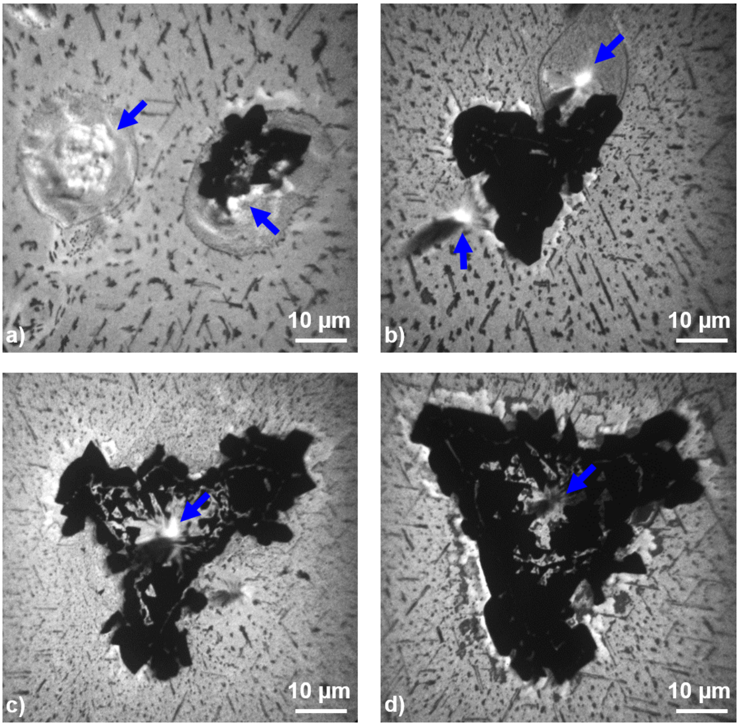

Fig. 7.2: UV-PEEM images of ceria structures, grown induced by copper crystal defects. Blue arrows show the defect positions. Images also in publication [123].

µ-XAS and X-PEEM were used to analyze the chemical composition of the triangular structure in Fig. 7.2 d). Several distinctive regions of this structure are marked in Fig. 7.3. These are: Region A, at the defect site in the center of the structure, region B, in the bright area surrounding the defect, region C, in the dark area filling most of the triangle, region D, a ceria island outside the triangle structure, and region E, at the bright rim separating the triangle structure from the outside area.

The µ-XAS spectra of the Ce M_5 and Cu L_3 edges of these regions are shown in Fig. 7.4 a) and b). The spectra of the Ce M_5 edge reveal that all of these areas are composed of a mixture of Ce^{4+} and Ce^{3+}. The Ce^{4+} content values determined for the five regions are: 89 %, 76 %, 90 %, 91 %, and 57 %. This shows clearly that the cerium oxide stoichiometry of the defect mediated structure is very inhomogeneous, and that it maintains considerable degrees of reduction even in an oxygen ambient of 5 × 10^{-7} mbar. Usually freshly grown ceria in an oxygen ambient like this are very close to completely oxidized Ce^{4+}, as shown in the previous chapters.

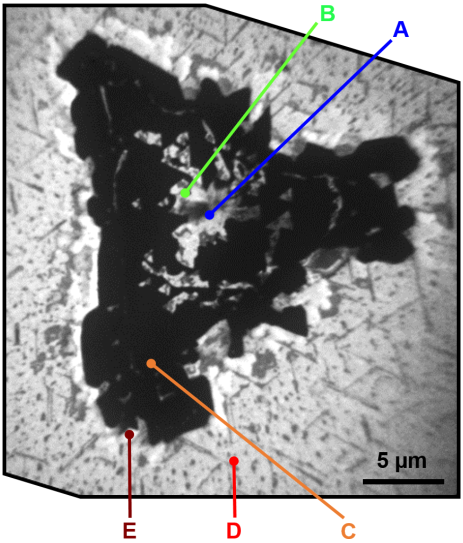

Fig. 7.3: a) UV-PEEM image of ceria triangle structure, indicating the regions for the µ-XAS spectra in Fig. 7.4.

The spectra of the Cu L_3 edge for the regions A, B, D, and E show two peaks within the measured energy range, characteristic for metallic copper and comparable to the metallic Cu L_3 spectra in subsection 3.2.4. For region C, the second peak of the Cu spectrum is noticeably lower, which indicates a stronger white-line peak and copper oxidation [101]. This can be interpreted as the formation of an oxide mixture of copper and ceria.

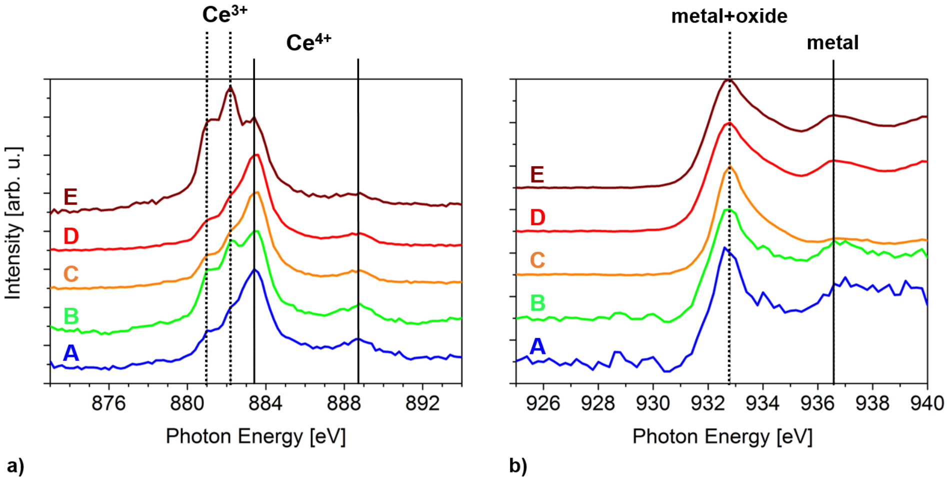

Fig. 7.4: µ-XAS of the regions indicated in Fig. 7.3: a) Ce M_5 edge, b) Cu L_3 edge.

A map of the spatial distribution of Ce^{4+} and Ce^{3+} is shown in Fig. 7.5 a). The map was obtained by a division of two X-PEEM images recorded at the characteristic energy of Ce^{4+} and the spectral energy of the second Ce^{3+} shoulder. In the map, blue and red areas indicate more reduced areas with Ce^{3+} and more oxidized areas with Ce^{4+} respectively. This shows that the cerium oxide reduction is correlated with the defect mediated structure, while the ceria islands outside the defect structure are oxidized as expected. The spatial distribution of the intensity loss at the second Cu peak is mapped in Fig. 7.5 b) by a division of two X-PEEM images recorded at the two Cu peaks at 932.8 eV and 936.8 eV. The blue areas in the map have the lowest relative intensity of the second Cu peak and thereby reveal the areas with copper oxidation, red areas are more metallic. Therefore, the map shows that the distribution of the oxidized state of copper matches in large areas with the distribution of Ce^{3+}.

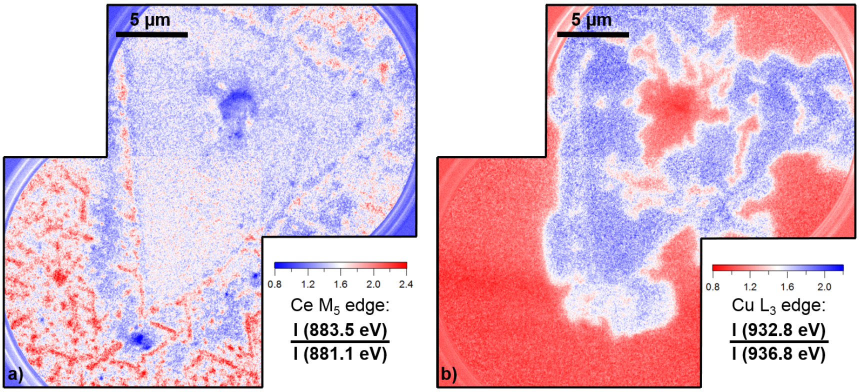

Fig. 7.5: a)Division of X-PEEM images recorded at the Ce M_5 peaks at 883.5 eV and 881.1 eV, b) Division of X-PEEM images recorded at the Cu L_3 peaks at 932.8 eV and 936.8 eV, also in publication [123].

Below, and in the vicinity of regular ceria (111) and (100) islands, no oxidized copper is observed, as discussed in subsection 3.2.4, even though oxygen is adsorbed on the copper surface. This supports the suggestion, that copper and ceria form a mixed oxide inside the defect induced structures. The high degree of reduction, found for Ce M_5 spectra belonging to the defect structure, is in agreement with the properties of a copper–ceria solid solution [124]. For a copper-ceria solid solution, cerium atoms can persist in the Ce^{3+} state easily, even in an oxygen atmosphere, which is not possible for pure ceria. The Ce^{3+} state is maintained by an electronic exchange with Cu, such as: $Ce^{4+} + Cu^{1+} \rightarrow Ce^{3+} + Cu^{2+}$.

Copper-ceria mixed oxides on the surface of a ceria/Cu(111) model system can influence the chemical reactions taking place on it enormously. Copper-ceria combinations are well known catalysts used for several industrial applications. The use of CuO/CeO_2 catalysts for the water-gas shift reaction was already introduced in subsection 1.2.3. Other applications of copper-ceria are the preferential CO oxidation [125], or methanol synthesis [126].

The existence of microscopic, defect mediated structures with such large variations in stoichiometry, oxidation states and expected chemistry, compared to areas of the sample not influenced by defects, needs to be considered for the use of a model system. If techniques averaging over a large area of the sample, or the whole sample, such as XPS or activity measurements obtained from a reactor, are used, the results can be strongly influenced by defect structures. For area averaging techniques, the defect structures are small enough in size to be overlooked, but their surface coverage of up to 2 % is large enough to have an impact on the surface chemistry. On the other hand, the defect structures are also unlikely to be found by techniques working at the nanoscale or with atomic level resolutions, such as STM, which are commonly used for the structural analysis of model systems. Therefore, using comparable and appropriate length-scales is important, when the chemistry of explicit structural features, like specific surface terminations, is examined.

A microscopic approach, using a combination of LEEM, PEEM and μ-LEED, has the advantage of providing chemical and structural information at the same length scale. Then defect structures, as the ones discussed here, can be detected and a defect free area of the sample can be selected for the analysis. While doing so, it is also secured that the obtained chemical information is actually attributed to the correct structural features.

Summary and outlook

The focus of this thesis was the direct comparison of the (111) and (100) cerium oxide surface orientations in terms of their redox properties. This was done with the aim to better understand the influence of different cerium oxide crystal surface terminations on the oxygen storage capacity and consequently on catalytic oxidation and reduction reactions. For this purpose, a model system consisting of microscopic, ulta-thin (111) and (100) oriented ceria islands prepared on a Cu (111) single crystal was employed. Experiments using UV-PEEM, X-PEEM and LEEM imaging combined with µ-LEED and µ-XAS were performed to observe the (111) and (100) cerium oxide terminations in-situ, in real-time and under identical thermal and chemical conditions simultaneously. To our knowledge, this is a first–of-a-kind study reaching this level of detail and suppressing unambiguities arising from performing equivalent experiments on different surface terminations separately.

The most important results and their conclusions can be summarized in these points:

- The reduction behavior of ceria (111) and (100) islands of two different thicknesses in a hydrogen atmosphere was examined. It was found that (100) oriented islands become more reduced than the (111) islands.
- An analysis of the reduction kinetics showed that the cerium oxide islands are not fully reduced from Ce^{4+} to Ce^{3+}. Instead, an equilibrium between the Ce^{4+} and Ce^{3+} contents of the islands is formed.
- The determined kinetic rates of the reduction process were shown to be very similar for both surface orientations. It follows, that the kinetics are not the reason for the stronger reduction of the (100) ceria islands.
- In contrast to the kinetic rates, the reduction equilibrium levels are very different for the two surface orientations. The remaining Ce^{4+} content at equilibrium is considerably lower for the (100) cerium oxide islands. For the first set of reduced cerium oxide islands the equilibrium Ce^{4+} contents were: 70 % for (111) and only 50 % for (100) cerium oxide.
- The difference in the Gibbs free energies for the (111) and (100) surfaces were determined and showed an agreement with values from density functional theory calculations, predicting a lower oxygen vacancy creation energy for the ceria (100) surface.

- Apart from reduction in hydrogen, a second mechanism - the deposition of metallic cerium in vacuum on top of the original layers - was used for the reduction of ceria (111) and (100) islands. In agreement with the results for the reduction in hydrogen, the (100) islands again showed a higher reducibillity than the (111) islands.

- The reduction in hydrogen was also used for a Pt/CeO_2 system, which was prepared by the deposition of Pt on top of cerium oxide (111) and (100) islands. During the experiment, the formation of highly reduced cerium oxide structures decorating the original islands was observed. It was concluded that these decoration structures are the areas where Pt and cerium oxide form a mixture and form active centers for catalysis. For the (100) islands the formation of the presumed Pt-cerium oxide mixture was observed to a greater degree.

- The advantages of using a microscopic approach for model catalysts was demonstrated by observations on the formation of crystal defect induced cerium oxide structures. The strikingly different stoichiometry of these structures combined with their observed interaction with the copper substrate imply an influence of these structures on chemical reactions. With microscopic information these defect structures can be detected and a defect free area of the sample can be selected for the analysis.

In summary, for the results of the performed experiments, a strong influence of the ceria surface termination on the reduction behavior was found, with ceria (100) being more reducible than ceria (111) in all of our case studies. The resulting conclusion is that the thermodynamics and not the kinetics are the main difference between the two surfaces and the cause for the overall higher reducibility of ceria (100). At least for very thin ceria films with a thickness of some Å, exposing the ceria (100) surface increases the oxygen storage capacity, which is a valuable information in order to better understand the role of different ceria crystal surfaces in catalysis.

Due to the widespread and well established use of platinum-cerium oxide combinations in heterogeneous catalysis, the results obtained for this system are of high significance for many key industries. The conclusion to the experimental results is that the Pt-cerium oxide mixture forms predominantly on the edges of the cerium oxide islands, while also partly covering the surface of (100) islands. This shows a stronger interaction between Pt and the (100) cerium oxide surface resulting in a better dispersion and anchoring of Pt on the (100) surface. Therefore, using cerium oxide structures with (100) surface orientations for the production of Pt-cerium oxide catalysts could improve their catalytic efficiency and also lower their costs by reducing the necessary amount of Pt.

For the future, there are still many experiments building on the experiments performed for this thesis that can yield interesting results. Particularly the experiment using the platinum-cerium oxide combination leaves open questions, which could be solved by repeating the experiment in a setup that allows the direct observation of the spatial Pt distribution. These experiments are already scheduled at the

NanoESCA facility at the synchrotron Elettra in Trieste, Italy, which is capable of chemically-resolved imaging using core-level photoelectrons.

Another interesting aspect, which will be studied in nearest future, is the preparation of ceria islands with (110) termination. During the most recent experiments at the LEEM/PEEM endstation at BESSY-II, the growth of ceria islands with this surface termination on Cu (111) was observed. However, the growth process and the needed growth parameters are not yet fully optimized, leaving room for further investigations. If this growth mechanism could be understood it would be possible to compare all three low-index ceria surfaces: the (111), (100) and (110) at the same time in a similar manner to the experiments described in this thesis.
In addition to the cerium oxide reduction in hydrogen, investigating reactions in carbon monoxide and methanol would move the experiments further on the path towards real–life catalytic reactions.

Bibliography

[1] S. H. Jensen, P. H. Larsen, and M. Mogensen, *Hydrogen and synthetic fuel production from renewable energy sources*, International Journal of Hydrogen Energy **32** (2007), 3253–3257.

[2] Z. Jiang, T. Xiao, V. L. Kuznetsov, and P. P. Edwards, *Turning carbon dioxide into fuel*, Philosophical Transactions of the Royal Society A **368** (2010), 3343–3364.

[3] R. Schlögl and F. Schüth, *Transport- und Speicherformen für Energie - Die Zukunft der Energie. Die Antwort der Wissenschaft*, pp. 246–281, C. H. Beck, 2008.

[4] R. Schlögl, *Heterogeneous Catalysis*, Angewandte Chemie International Edition **54** (2015), 3465–3520.

[5] H. J. Freund, *Model Studies in Heterogeneous Catalysis*, Chemistry a European Journal **16** (2010), 9384–9397.

[6] A. Trovarelli, *Catalysis by Ceria and related Materials*, Catalytic Science Series, Imperial College Press, 2002.

[7] D. R. Mullins, *The surface chemistry of cerium oxide*, Surface Science Reports **70** (2015), 42–85.

[8] T. Montini, M. Melchionna, M. Monai, and P. Fornasiero, *Fundamentals and Catalytic Applications of* CeO_2 *Based Materials*, Chemical Reviews **116** (2016), 10, 5987–6041.

[9] W. C. Chueh, C. Falter, M. Abbott, D. Scipio, P. Furler, S. M. Haile, and A. Steinfeld, *High-Flux Solar-Driven Thermochemical Dissociation of* CO_2 *and* H_2O *Using Nonstoichiometric Ceria*, Science **330** (2010), 6012, 1797–1801.

[10] J. Kašpar, P. Fornasiero, and N. Hickey, *Automotive catalytic converters: current status and some perspectives*, Catalysis Today **77** (2003), 419–449.

[11] A. Bueno-López, *Diesel soot combustion ceria catalysts*, Applied Catalysis B: Environmental **146** (2014), 1–11.

[12] L. Fan, C. Wang, Chen. M., and B. Zhu, *Recent development of ceria-based (nano)composite materials for low temperature ceramic fuel cells and electrolyte-free fuel cells*, Journal of Power Sources **234** (2013), 154–174.

[13] H. Inaba and H. Tagawa, *Ceria-based solid electrolytes*, Solid State Ionics **83** (1996), 1–16.

[14] O. A. Marina, C. Bagger, S. Primdal, and M. Mogensen, *A solid oxide fuel cell with a gadolinia-doped ceria anode: preparation and performance*, Solid State Ionics **123** (1999), 199–208.

[15] A. Faur Ghenciu, *Review of fuel processing catalysts for hydrogen production in PEM fuel cell systems*, Current Opinion in Solid State and Materials Science **6** (2002), 389–399.

[16] H. Xu and X. Hou, *Synergistic effect of* CeO_2 *modified Pt/C electrocatalysts on the performance of PEM fuel cells*, International Journal of Hydrogen Energy **32** (2007), 4397–4401.

[17] J. Paier, C. Penschke, and J. Sauer, *Oxygen Defects and Surface Chemistry of Ceria: Quantum Chemical Studies Compared to Experiment*, Chemical Reviews **113** (2013), 3949–3985.

[18] J. A. Rodriguez, S. Ma, P. Liu, J. Hrbek, J. Evans, and M. Pérez, *Activity of* CeO_x *and* TiO_x *Nanoparticles Grown on Au(111) in the Water-Gas Shift Reaction*, Science **318** (2007), 1757–1760.

[19] L. Li, Y. Zhan, Q. Zheng, C. Chen, Y. She, X. Lin, and K. Wei, *Water-Gas Shift Reaction over CuO/*CeO_2 *Catalysts: Effect of the Thermal Stability and Oxygen Vacancies of* CeO_2 *Supports Previously Prepared by Different Methods*, Catalysis Letters **130** (2009), 532–540.

[20] J. L. F. Da Silva, *Stability of the* Ce_2O_3 *phases: A DFT+U investigation*, Physical Review B **76** (2007), 193108.

[21] P. W. Tasker, *The stabilty of ionic crystal surfaces*, Journal of Physics C: Solid State Pysics **12** (1979), 4977–4984.

[22] J. C. Conesa, *Computer modeling of surfaces and defects on cerium dioxide*, Surface Science **339** (1995), 337–352.

[23] M Baudin, M. Wójcik, and K. Hermansson, *Dynamics, structure and energetics of the (111), (011) and (001) surfaces of ceria*, Surface Science **468** (2000), 51–61.

[24] N. V. Skorodumova, M. Baudin, and K. Hermansson, *Surface properties of* CeO_2 *from first principles*, Physikal Review B **69** (2004), 075401.

[25] A. Siokou and R. M. Nix, *Interaction of Methanol with Well-Defined Ceria Surfaces: Reflection/Absorption Infrared Spectroscopy, X-ray Photoelectron Spectroscopy, and Temperature-Programmed Desorption Study*, Journal of Physical Chemistry B **103** (1999), 33, 6984–6997.

[26] F. Esch, Fabris S., L. Zhou, T. Montini, P. Fornasiero, G. Comelli, and R. Rosei, *Electron Localization Determines Defect Formation on Ceria Substrates*, Science **309** (2005), 752–755.

[27] D. R. Mullins, P. V. Radulovic, and S. H. Overbury, *Ordered cerium oxide thin films grown on Ru (0001) and Ni (111)*, Surface Science **429** (1999), 186–198.

[28] S. Torbrügge, M. Cranney, and M. Reichling, *Morphology of step structures on* CeO_2 *(111)*, Applied Physics Letters **93** (2008), 073112.

[29] H. Nörenberg and G. A. D. Briggs, *The surface structure of* CeO_2 *(110) single crystals studied by STM and RHEED*, Surface Science **433–435** (1999), 127–130.

[30] J. Höcker, T. Duchoň, K. Veltruská, V. Matolíń, J. Falta, S. D. Senanayake, and J. I. Flege, *Controlling Heteroepitaxy by Oxygen Chemical Potential: Exclusive Growth of (100) Oriented Ceria Nanostructures on Cu(111)*, The Journal of Physical Chemistry C **120** (2016), 4895–4901.

[31] Y. Pan, N. Nilius, C. Stiehler, H.-J. Freund, J. Goniakowski, and C. Noguera, *Ceria Nanocrystals Exposing Wide (100) Facets: Structure and Polarity Compensation*, Advanced Material Interfaces **1** (2014), 1400404.

[32] Y. Lin, Z. Wu, J. Wen, K. R. Poeppelmeier, and L. D. Marks, *Imaging the Atomic Surface Structures of* CeO_2 *Nanoparticles*, Nano Letters **14** (2014), 191–196.

[33] N. V. Skorodumova, S. I. Simak, B. I. Lundqvist, and B. Abrikosov, I.A. Johansson, *Quantum Origin of the Oxygen Storage Capability of Ceria*, Physical Review Letters **89** (2002), 16, 166601.

[34] M. Aryanpour, A. Khetan, and H. Pitsch, *Activity Descriptor for Catalytic Reactions on Doped Cerium Oxide*, ACS Catalysis **3** (2013), 1253–1262.

[35] M. Nolan, S. C. Parker, and G. W. Watson, *The electronic structure of oxygen vacancy defects at the low index surfaces of ceria*, Surface Science **595** (2005), 223–232.

[36] F. A. Kröger and H. J. Vink, *Relations between the Concentrations of Imperfections in Crystalline Solids*, Solid State Physics **3** (1956), 307–435.

[37] M. Nolan, J. E. Fearon, and G. W. Watson, *Oxygen vacany formation and migration in ceria*, Solid State Ionics **177** (2006), 3069–3074.

[38] Wu, *Probing Defect Sites on* CeO_2 *Nanocrystals with well-defined Surface Planes by Raman Spectroskopy and* O_2, Langmuir **26** (2010), 16595–16606.

[39] M. Capdevila-Cortada, G. Vilé, D. Teschner, J. Pérez-Ramírez, and N. Lopéz, *Reactivity descriptors for ceria in catalysis*, Applied Catalysis B: Environmental **197** (2016), 299–312.

[40] K. Zhou, X. Wang, X. Sun, Q. Peng, and Y. Li, *Enhanced catalytic activity of ceria nanorods from well-defined reactive crystal planes*, Journal of Catalysis **229** (2005), 206–212.

[41] G. Vilé, S. Colussi, F. Krumeich, A. Trovarelli, and J. Pérez-Ramirez, *Opposite Face Sensitivity of* CeO_2 *in Hydrogenation and Oxidation Catalysis*, Angewandte Chemie International Edition **53** (2014), 12069–12072.

[42] M. García-Melchor and N. López, *Homolytic Products from Heterolytic Paths in* H_2 *Dissociation on Metal Oxides: The Example of* CeO_2, The Journal of Physical Chemistry C **118** (2014), 10921–10926.

[43] H.-X. Mai, L.-D. Sun, Y.W. Zhang, W. Si, R. Feng, H.-P. Zhang, H.-C. Liu, and C.-H. Yan, *Shape-Selective Synthesis and Oxygen Storage Behavior of Ceria Nanopolyhedra, Nanorods, and Nanocubes*, The Journal of Physical Chemistry B **109** (2005), 24380–24385.

[44] J. Zhang, H. Kumagai, K. Yamamura, S. Ohara, S. Takami, A. Morikawa, H. Shinjoh, K. Kaneko, T. Adschiri, and A. Suda, *Extra-Low-Temperature Oxygen Storage Capacity od* CeO_2 *Nanocrystals with Cubic Facets*, Nano Letters **11** (2011), 361–364.

[45] T. S. Sreeremya, A. Krishnan, K. C. Remani, K. R. Patil, D. F. Brougham, and S. Ghosh, *Shape-Selective Oriented Cerium Oxide Nanocrystals Permit Assessment of the Effect of the Exposed Facets on Catalytic Activity and Oxygen Storage Capacity*, Applied Materials and Interfaces **7** (2015), 8545–8555.

[46] J.-L. Lu, H.-J. Gao, S. Shaikhutdinov, and H. J. Freund, *Gold supported on well-ordered ceria films: nucleation, growth and morphology in CO oxidation reaction*, Catalysis Letters **114** (2007), 8–16.

[47] E. L. Wilson, Q. Chen, W. A. Brown, and G. Thornton, *CO Adsorption on the Model Catalyst* $Pd/CeO_{2-x}(111)/Rh(111)$, The Journal of Physical Chemistry C **111** (2007), 14215–14222.

[48] V. Matolín, J. Libra, I. Matolínová, V. Nehasil, L. Sedláček, and F. Šutara, *Growth of ultra-thin cerium oxide layers on Cu(111)*, Applied Surface Science **254** (2007), 153–155.

[49] O. Stetsovych, F. Pagliuca, F. Dvořák, T. Duchoň, M. Vorokhta, and V. Matolín, *Epitaxial Cubic* Ce_2O_3 *Films via Ce-*CeO_2 *Interfacial Reaction*, The Journal of Physical Chemistry Letters **4** (20013), 866–871.

[50] J. Höcker, T. O. Menteş, A. Sala, A. Locatelli, T. Schmidt, J. Falta, S. D. Senanayake, and J. I. Flege, *Unraveling the Dynamic Nanoscale Reducibility (*$Ce^{4+} \rightarrow Ce^{3+}$ *of* CeO_x*–Ru in Hydrogen Activation*, Advanced Material Interfaces **2** (2015), 1500314.

[51] D. C. Grinter, S. D. Sananayake, and J. I. Flege, *In Situ Growth, Structure, and Real-Time Chemical Reactivity of Well-Defined CeO$_x$-Ru(0001) Model Surfaces*, Applied Caralysis B Enviromental **197** (2016), 286–298.

[52] D. C. Grinter, C. Muryn, A. Sala, C.-M. Yim, C. L. Pang, T. O. Menteş, A. Locatelli, and G. Thornton, *Spillover Reoxidation of Ceria Nanoparticles*, The Journal of Physical Chemistry C **120** (2016), 11037–11044.

[53] J. I. Flege, J. Höcker, B. Kaemena, T. O. Menteş, A. Sala, A. Locatelli, S. Gangopadhyay, J. T. Sadowski, S. D. Senanayake, and J. Falta, *Growth and Characterization of Epitaxially Stabilized Ceria(001) Nanostructures on Ru(0001)*, Nanoscale **8** (2016), 10849–10856.

[54] O. Stetsovych, J. Beran, F. Dvořák, K. Mašek, J. Mysliveček, and V. Matolín, *Polarity driven morphology of CeO$_2$ (100) islands on Cu(111)*, Applied Surface Science **285** (2013), Part B, 766–771.

[55] D. M. Gottlob, *Spin-reorientation transition in epitaxial Ni$_x$Pd$_{1-x}$ films on Cu(001): a microscopic analysis*, Doctoral Thesis, Universität Duisburg-Essen, 2015.

[56] R. M. Tromp, J. B. Hannon, A. W. Ellis, W. Wan, A. Berghaus, and O. Schaff, *A new aberration-corrected, energy filtered LEEM/PEEM instrument. I. Principles and design*, Ultramicroscopy **110** (2010), 852–861.

[57] R. M. Tromp, J. B. Hannon, W. Wan, and O. Schaff, *A new aberration-corrected, energy filtered LEEM/PEEM instrument. II. Operation and results*, Ultramicroscopy **127** (2013), 25.

[58] E. Brüche, *Elektronenmikroskopische Abbildung mit lichtelektrischen Elektronen*, Zeitschrift für Physik **86** (1933), 448–450.

[59] E. Brüche and W. Knecht, *Bemerkung über die Erreichung hoher Auflösungen mit dem elektronenoptischen Immersionsobjektiv*, Zeitschrift für Physik **92** (1934), 462–466.

[60] W. Telieps and E. Bauer, *An analytical reflection and emission UHV surface election microscope*, Ultramicriscopy **17** (1985), 57–66.

[61] L. H. Veneklasen, *The continuing development of low-energy electron microscopy for characterizing surfaces*, Review of Scientific Instruments **63** (1992), 5513.

[62] O. L. Krivanek, N. Dellby, and M. F. Murfitt, *Handbook of Charged Particle Optics - Aberration correction in electron microscopy*, chap. 12, second ed., CRC Press, 2009.

[63] F. Nickel, *Aberrationskorrigierte Photoemissionsmikroskopie an magnetischen Sy-*

stemen: Von statischer Charakterisierung zu zeitaufgelöster Abbildung, Doctoral Thesis, Universität Duisburg-Essen, 2013.

[64] A. Einstein, *Über einen die Erzeugung und Verwandlung des Lichtes betreffenden heuristischen Gesichtspunkt*, Annalen der Physik **322** (1905), 132–148.

[65] P. A. M. Dirac, *The quantum theory of dispersion*, Proceedings of the Royal Society of London. Series A **114** (1927), 710.

[66] E. Fermi, *Nuclear Physics: A Course Given by Enrico Fermi at the University of Chicago*, Midway Reprints, University of Chicago Press, 1950.

[67] S. Hüfner, *Photoelectron Spectroscopy, Principles and Applications*, third ed., Springer, 2003.

[68] W. Nolting, *Quantenmechanik - Methoden und Anwendungen*, 6th ed., Springer, 2006.

[69] M. P. Seah and W.A. Dench, *Quantitative electron spectroscopy of surfaces: Astandard data base for electron inelastic mean free paths in solids*, Surface and Interface Analysis **1** (1979), 2–11.

[70] S. Tougaard, *Quases-IMFP-TPP2M Ver. 3.0*, Quases-Trougard Inc., 2000–2016.

[71] S. Tanuma, C. J. Powell, and D. R. Penn, *Calculations of electron inelastic mean free paths. IX. Data for 41 organic elemental solids over the 50 eV to 30 keV range*, Surface and Interface Analysis **43** (2011), 689.

[72] B. H. Frazer, B. Gilbert, B. R. Sonderegger, and G. De Stasio, *The probing depth of total electron yield in the sub-keV range: TEY-XAS and X-PEEM*, Surface Science **537** (2003), 161–167.

[73] C. M. Schneider, *Probing the Nanoworld - Electron Emission and Photoemission Microscopy*, IFF Spring School Lecture Notes, vol. 38, chap. C6, Forschungszentrum Jülich GmbH, 2007.

[74] C. M. Schneider and G. Schönhense, *Investigating surface magnetism by means of photoexcitation electron emission microscopy*, Reports on Progress in Physics **65** (2002), 1785–1839.

[75] M. M. Beerbom, B. Lägel, A. J. Cascio, B. V. Doran, and R. Schlaf, *Direct comparison of photoemission spectroscopy and in situ Kelvin probe work function measurements on indium tin oxide films*, Journal of Electron Spectroscopy and Related Phenomena **152** (2006), 12–17.

[76] S. Cherifi, *Probing the Nanoworld - LEEM and Spin-Polarized LEEM*, IFF Spring School Lecture Notes, vol. 38, chap. C7, Forschungszentrum Jülich GmbH, 2007.

[77] J. Schaab, I. P. Krug, H. Doğanay, J. Hackl, D. M. Gottlob, I. K. Khan, S. Nemšák, L. Maurel, E. Langenberg, P. A. Algarabel, C. M. Schneider, and D. Meier, *Contact-Free Mapping of Electronic Transport Phenomena of Polar Domains in* $SrMnO_3$ *Films*, Physical Review Applied **5** (2016), 054009.

[78] W. Święch, E. Bauer, and M. Mundschau, *A low-energy electron microscopy study of the system Si(111)-Au*, Surface Science **253** (1991), 283–296.

[79] E. Bauer, *LEEM Basics*, Surface Review Letters **05** (1998), 1275.

[80] S. Cramm, *Probing the Nanoworld - Synchrotron Radiation Sources and Beamlines: Overview*, IFF Spring School Lecture Notes, vol. 38, chap. B2, Forschungszentrum Jülich GmbH, 2007.

[81] J. D. Jackson, *Klassische Elektrodynamik*, 4th ed., de Gruyter, 2006.

[82] BESSY II website: Wie funktioniert BESSY II?, *https://www.helmholtz-berlin.de/quellen/bessy/elektronenspeicherring/wie-funktioniert-bessy_en.html*, Helmholtz-Zentrum Berlin für Materialien und Energie, 2015.

[83] BESSY II website: Undulatoren, *https://www.helmholtz-berlin.de/forschung/oe/fg/undulatoren/geraete/ue56_en.html*, Helmholtz-Zentrum Berlin für Materialien und Energie, 2015.

[84] H. Yumoto, H. Mimura, T. Koyama, K. Matsuyama, S. Tono, K. Yamauchi, and et al., *Focusing of X-ray free-electron laser pulses with reflective optics*, Nature Photonics Letters **7** (2013), 43.

[85] L. E. Davis, N. C. MacDonald, P. W. Palmberg, G. E. Riach, and R. E. Weber, *Handbook of Auger Electron Spectroscopy*, second ed., Physical Electronics Industries, 1976.

[86] R.G. Musket, W. McLean, C.A. Colmenares, D. M. Makowiecki, and W. J. Siekhaus, *Preparation of Atomically clean Surfaces of selected Elements: A Review*, Applications of Surface Science **10** (1982), 143–207.

[87] J. Höcker, *In situ-Studien zu Wachstum und Struktur seltenerdoxidbasierter inverserModellkatalysatoren*, Doctoral Thesis, Universität Bremen, 2016.

[88] F. Jensen, F. Besenbacher, E. Laesgaard, and I. Stensgaard, *Oxidation of Cu(111): two new oxygen induced reconstructions*, Surface Science Letters **259** (1991), L774–L780.

[89] F. Yang, Y. M. Choi, S. Agnoli, P. Liu, D. Stacchiola, J. Hrbek, and J. A. Rodriguez, $CeO_2 \leftrightarrow CuO_X$ *Interactions and the Controlled Assembly of* CeO_2*(111) and* CeO_2*(100) Nanoparticles on an Oxidized Cu(111) Substrate*, The Journal of Physical Chemistry C **115** (2011), 23062–23066.

[90] F. Yang, Y. M. Choi, P. Liu, D. Stacchiola, J. Hrbek, and J. A. Rodriguez, *Identification of 5–7 Defects in a Copper Oxide Surface*, Journal of the American Chemical Society **133** (2011), 11474–11477.

[91] J. Höcker, W. Cartas, A. Schaefer, M. Bäumer, J. F. Weaver, J. Falta, and J.I. Flege, *Growth, Structure, and Stability of the High-Index* TbO_x*(112) Surface on Cu(111)*, The Journal of Physical Chemistry C **119** (2015), 14175–14184.

[92] J. Hackl, T. Duchoň, D. N. Müller, C. Mouls, D. M. Gottlob, M. I. Khan, S. Cramm, K. Veltruská, V. Matolín, S. Nemšák, and C. M. Schneider, *Reduction properties of model ceria (111) and (100) nanoislands*, The Journal of Physical Chemistry Letters (2017), submitted.

[93] F. Dvořák, O. Stetsovych, E. Stegner, M. Cherradi, I. Matonlínová, N. Tsud, M. Škoda, T. Skála, J. Mysliveček, and V. Matolín, *Adjusting Morphology and Surface Reduction of* CeO_2 *(111) Thin Films on Cu(111)*, The Journal of Physical Chemistry C **115** (2011), 7496–7503.

[94] T. Michely, M. Hohage, M. Bott, and G. Comsa, *Inversion of Growth Speed Anisotropy in Two Dimensions*, Physical Review Letters **70** (1993), 3943.

[95] S. O. Kucheyev, B. J. Clapsaddle, Wang Y. M., T. van Buuren, and A. V. Hamza, *Electronic structure of nanoporous ceria from x-ray absorption spectroscopy and atomic multiplet calculations*, Physical Review B **76** (2007), 235420.

[96] C. L. Dong, A. Augustsson, C. L. Chen, C. L. Chang, Chen Y. Y., and J.-H. Guo, *Electronic structure and valence state of* $CeAl_2$ *from X-ray absorption and emission spectroscopy*, Journal of Electron Spectroscopy **144–147** (2005), 581–584.

[97] R. C. Karnatak, J.-M. Esteva, H. Dexpert, M Gasgnier, P. E. Caro, and L. Albert, *X-ray absorption studies of* $CeO_2, Pr =_2, andTbO_2$*. I. Manifestation of localized and extended f states in the 3d absorption spectra*, Physical review B **36** (1987), 3, 1746–1749.

[98] T. Duchoň, M. Aulická, E. F. Schwier, H. Iwasawa, C. Zhao, Y. Xu, K. Veltruská, K. Shimada, and V. Matolín, *Covalent versus localized nature of* $4f$ *electrons in ceria: Resonant angle-resolved photoemission spectroscopy and density functional theory*, Physical Review B **95** (2017), 165124.

[99] S. Tanuma, C. J. Powell, and D. R. Penn, *Calculations of electron inelastic mean free paths. V. Data for 14 organic compounds over the 50-2000 eV range*, Surface and Interface Analysis **21** (1994), 165–176.

[100] H. Shinotsuka, S. Tanuma, C. J. Powell, and D. R. Penn, *Calculations of electron inelastic mean free paths. X. Data for 41 elemental solids over 50 eV to 200 keV range with the relativistic full Penn algorithm*, Surface and Interface Analysis **47** (2015), 871–888.

[101] M. Grioni, J. F. van Acker, M. T. Czyžyk, and J. C. Fuggle, *Unoccupied electronic structure and core-hole effects in the x-ray absorption spectra of* Cu_2O, Physical Review B **45** (1992), 7, 3309–3318.

[102] M. Poengsen, J. F. Wolf, J. Frohn, M. Giesen, and H. Ibach, *Step dynamics on Ag(111) and Cu(100) surfaces*, Surface Science **274** (1992), 430–440.

[103] M. Lampimäki, K. Lahtonen, M. Hirsimäki, and M. Valden, *Nanoscale oxidation of Cu(100): Oxide morphology and surface reactivity*, The Journal of Chemical Physics **126** (2007), 034703.

[104] K. Lahtonen, M. Hirsimäki, M. Lampimäki, and M. Valden, *Oxygen adsorption-induced nanostructures and island formation on Cu(100): Bridging the gap between the formation of surface confined oxygen chemisorption layer and oxide formation*, The Journal of Chemical Physics **129** (2008), 124703.

[105] P. D. Kirsch and J. G. Ekerdt, *Chemical and thermal reduction of thin films of copper (II) oxide and copper (I) oxide*, Journal of Applied Physics **90** (2001), 4256.

[106] J. A. Eastman, P. H. Fuoss, L. E. Rehn, P. M. Baldo, G. W. Zhou, D. D. Fong, and L. J. Thompson, *Early-stage suppression of Cu (001) oxidation*, Applied Physics Letters **87** (2005), 051914.

[107] G. Kalkowski, G. Kaindl, G. Wortmann, D. Lentz, and S. Krause, *4f-ligand hybridization in* CeF_4 *and* TbF_4 *probed by core-level spectroscopies*, Physical Review B **37** (1988), 1376–1382.

[108] Z. Zhao, M. Uddi, N. Tsvetkov, B. Yildiz, and A. F. Ghoniem, *Redox Kinetics Study of Fuel Reduced Ceria for Chemical-Looping Water Splitting*, The Journal of Physical Chemistry C **120** (2016), 16271–16289.

[109] L. A. J. Garvie and P. R. Buseck, *Determination of* Ce^{4+}/Ce^{3+} *in electron-beam-damaged* CeO_2 *by electron energy-loss spectroscopy*, Journal of Physics and Chemistry of Soldis **60** (1999), 1943–1947.

[110] J. Sugar, W. D. Brewer, G. Kalkowski, G. Kaindl, and E. Paparazzo, *Photoabsorption by the 3d shell in CE, PR, Ho, and ER: Observations and calculations*, Physical Review A **32** (1985), 4, 2242–2248.

[111] S. Agnoli, A. E. Reeder, S. D. Senanayake, J. Hrbek, and J. A. Rodriguez, *Structure and special chemical reactivity of interface-stabilized cerium oxide nanolayers on* TiO_2*(110)*, Nanoscale **6** (2014), 800–810.

[112] T. X. T. Sayle, F. Caddeo, X. Zhang, T. Sakthivel, S. Das, S. Seal, S. Ptasinska, and D. C. Sayle, *Structure - Activity Map of Ceria Nanoparticles, Nanocubes, and Mesoporous Architectures*, Chemistry of Materials **28** (2016), 7287–7295.

[113] Z. A. Feng, F. E. Gabaly, X. Ye, Z.-X. Shen, and W. C. Chueh, *Fast vacancy-*

mediated oxygen ion incorporation across the ceria–gas electrochemical interface, Nature Communications **5** (2014), 4374, 1–9.

[114] N. Knoblauch, L. Dörrer, P. Fielitz, M. Schmücker, and G. Borchardt, *Surface controlled reduction kinetics of nominally undoped polycrystalline* CeO_2, Physical Chemistry Chemical Physics **17** (2015), 5849–5860.

[115] H. A. Al-Madfaa and M. M. Khader, *Reduction kinetics of ceria surface by hydrogen*, Materials Chemistry and Physics **86** (2004), 180–188.

[116] W. C. Chueh, A. H. McDaniel, M. E. Grass, Y. Hao, N. Jabeen, Z. Liu, S. M. Haile, K. F. McCarty, H. Bluhm, and F. E. El Gabaly, *Highly Enhanced Concentration and Stability of Reactive* Ce_{3+} *on Doped* CeO_2 *Surface Revealed In Operando*, Chemistry of Materials **24** (2012), 1876–1882.

[117] H. Chen, Y. M. Choi, M. Liu, and M. C. Lin, *A Theoretical Study of Surface Reduction Mechanisms of* CeO_2 *(111) and (110) by* H_2, ChemPhysChem **8** (2007), 849–855.

[118] M. Boaro, M. Vicerio, C. de Leitenburg, G. Dolcetti, and A. Trovarelli, *The use of temperature-programmed and dynamic/transient methods in catalysis: characterization of ceria-based, model three-way catalysts*, Catalysis Today **77** (2003), 407–417.

[119] G. N. Vayssilov, Y. Lykhach, A. Migani, T. Staudt, G. P. Petrova, N. Tsud, T. Skála, F. Illas, K. C. Prince, V. Matolín, K. M. Neyman, and J. Libuda, *Support nanostructure boosts oxygen transfer to catalytically active platinum nanoparticles*, Nature Materials **10** (2011), 310–315.

[120] Y. Lykhach, S. M. Kozlov, T. Skála, A. Tovt, V. Stetsovych, V. Matolín, K. M. Neyman, J. Libuda, and et al., *Counting electrons on supported nanoparticles*, Nature Materials **15** (2015), 284.

[121] P. Luches, F. Pagliuca, S. Valeri, F. Illas, G. Preda, and G. Pacchioni, *Nature of Ag Islands and Nanoparticles on the* CeO_2*(111) Surface*, The Journal of Plysical Chemistry C **116** (2012), 1122–1132.

[122] A. Bruix, Y. Lykhach, I. Matolínová, V. Matolín, J. Libuda, K. M. Neymann, and et. al., *Maximum Nobel-Metal Efficiency in Catalytic Materials: Atomically Dispersed Surface Platinum*, Angewandte Chemie International Edition **53** (2014), 10525–10530.

[123] T. Duchoň, J Hackl, J. Höcker, K. Veltruská, V. Matolín, J. Falta, S. Cramm, S. Nemšák, C. M. Schneider, J. I. Flege, and S. D. Senanayake, *Exploiting micro-scale structural and chemical observations in real time for understanding chemical conversion: LEEM/PEEM studies over* CeO_x*–Cu(111)*, Ultramicroscopy (2017), accepted.

[124] S. Hočevar, J. Batista, and J. Levec, *Wet Oxidation of Phenol on* $Ce_{1-x}Cu_xO_{2-\delta}$ *Catalyst*, Journal of Catalysis **184** (1999), 39–48.

[125] F. Wang, R. Büchel, A. Savitsky, M. Zalibera, D. Widmann, S. E. Pratsinis, W. Lubitz, and F. Schüth, *In Situ EPR Study of the Redox Properties of CuO-*CeO_2 *Catalysts for Preferential CO Oxidation (PROX)*, ACS Catalysis **6** (2016), 3520–3530.

[126] S. D. Senanayake, P. J. Ramirez, I. Waluyo, S. Kundu, K. Mudiyanselage, Z. Liu, Z. Liu, S. Axnanda, D. J. Stacciola, J. Evans, and J. A. Rodriguez, *Hydrogenation of* CO_2 *to Methanol on* CeO_x*/Cu(111) and ZnO/Cu(111) Catalysts: Role of the Metal–Oxide Interface and Importance of* Ce^{3+} *Sites*, The Journal of Physical Chemistry C **120** (2016), 3, 1778–1784.

Acknowledgments

First of all, I would like to thank Dr. Slavomír Nemšák for making this thesis possible by providing the project idea and for his invaluable support, advice and patience at all stages of this work.

I would like to express my gratitude towards Prof. Dr. Claus M. Schneider for giving me the opportunity to work as a member of the Forschungszentrum Jülich LEEM/PEEM group at BESSY II.

Sincere thanks go to Tomáš Duchoň for the many beamtimes at BESSY II, which became much more productive by his presence and for the extensive discussions, which promoted the understanding of unforeseen experimental observations.

I am very thankful for Dr. David N. Müller's insights as a chemist, which greatly helped me with the correct interpretation of the experimental results.

I would like to thank Dr. Daniel M. Gottlob, who over the course of time answered countless questions I had about instrumental details of the LEEM/PEEM instrument and the preparation chamber.

At the very beginning of my time at BESSY II, Hatice Doğanay taught me the proper alignment procedure of the LEEM/PEEM instrument. I am thankful for this good starting point for my experiments.

Special thanks go to Dr. Stefan Cramm for his support at the beamline, for helping me to solve various technical problems and for his spontaneous check-up calls at the beamline during nightshifts.

From the Peter-Grünberg-Institute 6, I would like to thank Jürgen Lauer and Norbert Schnitzler for their work on the beamline computer, Heinz Pfeifer for his help with electronic problems and all the colleges and fellow students, who always welcomed me with friendliness whenever I came for a visit.

Finally, I would like to thank Prof. Dr. Vladimír Matolín and Dr. Kateřina Veltruská who welcomed me for a brief, but very informative visit at the Surface Physics Group in Prague.

Curriculum Vitae

Personal Data:

Name: Johanna Maria Hackl

Date of birth: 12.11.1987

Place of birth: Aachen

Nationality: German

E-mail: Johanna.Hackl@rub.de

Education:

07/2017: Submission of Ph.D. thesis (Dr. rer. Nat.), Universität Duisburg-Essen

Title: *Reduction properties of a model ceria catalyst at the microscopic scale*

05/2014 – ongoing: Ph.D. student in Physics, Peter-Grüunberg-Institut 6, Forschungszentrum Jülich / Universität Duisburg-Essen

03/2014: Diploma in Physics, Ruhr-Universität Bochum

Title of diploma-thesis: *Rauschspektroskopie an einem Festkörpermodell-System*

10/2006 – 03/2014: Diploma student in Physics, Ruhr-Universität Bochum

06/2006: Abitur, Hildegardis-Schule, Bochum

Work experience:

05/2014 – ongoing: Research assistant and doctoral candidate, Peter-Grüunberg-Institut 6, Forschungszentrum Jülich

04/2013 – 01/2014: Research assistant, Ruhr-Universität Bochum

10/2009 – 05/2010: Teaching assistant, Ruhr-Universität Bochum

List of publications

(Listed in reversed chronological order.)

Papers

J. Hackl, T. Duchoň, D. N. Müller, C. Mouls, D. M. Gottlob, M. I. Khan, S. Cramm, K. Veltruská, V. Matolín, S. Nemšák, and C. M. Schneider, *Reduction properties of model ceria (111) and (100) nanoislands*, The Journal of Physical Chemistry Letters (2017), submitted.

S. Nemšák, E. Strelcov, T. Duchoň, H. Guo, J. Hackl, A. Yulaev, I. Vlassiouk, D. Mueller, C. M. Schneider, A. Kolmakov, *Interfacial Electrochemistry in Liquids Probed with Photoemission Electron Microscopy*, Journal of the American Chemical Society (2017), submitted.

T. Duchoň, J. Hackl, J. Höcker, K. Veltruská, V. Matolín, J. Falta, S. Cramm, S. Nemšák, C. M. Schneider, J. I. Flege, and S. D. Senanayake, *Exploiting micro-scale structural and chemical observations in real time for understanding chemical conversion: LEEM/PEEM studies over* CeO_x*–Cu(111)*, Ultramicroscopy (2017), accepted.

C. Baeumer, C. Schmitz, A. Marchewka, D. N. Mueller, R. Valenta, J. Hackl, N. Raab, S. P. Rogers, M. I. Khan, S. Nemsak, M. Shim, S. Menzel, C. M. Schneider, R. Waser and R. Dittmann, *Quantifying redox-induced Schottky barrier variations in memristive devices via in operando spectromicroscopy with graphene electrodes*, Nature Communications **7** (2016), 12398.

J. Schaab, I. P. Krug, H. Doğanay, J. Hackl, D. M. Gottlob, I. K. Khan, S. Nemšák, L. Maurel, E. Langenberg, P. A. Algarabel, C. M. Schneider, and D. Meier, *Contact-Free Mapping of Electronic Transport Phenomena of Polar Domains in* $SrMnO_3$ *Films*, Physical Review Applied **5** (2016), 054009.

Conference contributions

(Only contributions that were presented by myself are listed.)

Talks

J. Hackl, T. Duchoň, D. N. Mueller, C. Mouls, M.I. Khan, S. Cramm, S. Nemšák, C.M. Schneider, *The Impact of the Surface Orientation of* CeO_2 *on its Reduction Behavior*, 21st International Conference of Solid State Ionics, Padua, Italy, 18.-23. June 2017

J. Hackl, T. Duchoň, D. N. Müller, D. M. Gottlob, I. Khan, S. Cramm, S. Nemšák, and C. M. Schneider, *On the reduction behavior of* CeO_2 *(100) and (111) surfaces*, Frühjahrstagung der DPG, Dresden, Germany, 19.-24. March 2017

Posters

Hackl, Duchoň, Müller, Mouls, Gottlob, Khan, Cramm, Nemšák, Schneider, *On the reduction behavior of* CeO_2 *(100) and (111) surfaces*, 8th BESSY II User Meeting, Berlin, Germany, 07.-09. December 2016

J. Hackl, T. Duchoň, D. M. Gottlob, C. Mouls, I. Khan, S. Cramm, S. Nemšák, C. M. Schneider, *On the reduction behavior of* CeO_2 *(100) and (111) surfaces*, LEEM/PEEM-10, Monterey, California, USA, 11.-15. September 2016

Schaab J, Hackl J, Khan I, Doğanay H, Gottlob D, Nemšák S, Krug I P, Schneider C M, and Meier D, *Investigating electronic transport properties of ferroelectric domains and domain walls by LEEM and X-PEEM*, 7th BESSY II User Meeting, Berlin, Germany, 09.-11. December 2015

Hackl J, Gottlob D, Doğanay H, Khan M I, Khalakhan I, Doering S, Matolin V, Fadley C, Cramm S, Nemšák S, Schneider C M, *A Spectromicroscopical Observation of a Nanoparticle Noble Catalyst for the Oxygen Reduction Reaction*, 6th BESSY II User Meeting, Berlin, Germany, 03.-05. December 2014

Band / Volume 394
Water vapour in the UTLS – Climatologies and Transport
P. R. Neis (2017), x, 124 pp
ISBN: 978-3-95806-269-6

Band / Volume 395
Neutronenaktivierungsanalyse mit gepulsten 14 MeV Neutronen zur Charakterisierung heterogener radioaktiver Abfälle
F. Mildenberger (2017), vi, 128 pp
ISBN: 978-3-95806-271-9

Band / Volume 396
Coupled biotic-abiotic mechanisms of nitrous oxide production in soils during nitrification involving the reactive intermediates hydroxylamine and nitrite
S. Liu (2017), xvii, 148 pp
ISBN: 978-3-95806-272-6

Band / Volume 397
Mixed-phase and ice cloud observations with NIXE-CAPS
A. Costa (2017), xviii, 117 pp
ISBN: 978-3-95806-273-3

Band / Volume 398
Deposition Mechanisms of Thermal Barrier Coatings (TBCs) Manufactured by Plasma Spray-Physical Vapor Deposition (PS-PVD)
W. He (2017), ix, 162 pp
ISBN: 978-3-95806-275-7

Band / Volume 399
Carbonyl Sulfide in the Stratosphere: airborne instrument development and satellite based data analysis
C. Kloss (2017), vi, 84, 1-14 pp
ISBN: 978-3-95806-276-4

Band / Volume 400
Lagrangian transport of trace gases in the upper troposphere and lower stratosphere (UTLS)
P. Konopka (2017), 70 pp
ISBN: 978-3-95806-279-5

Band / Volume 401
Numerical Simulation of Plasma Spray-Physical Vapor Deposition
P. Wang (2017), IX, 127 pp
ISBN: 978-3-95806-282-5

Band / Volume 402
The Selective Separation of Am(III) from Highly Radioactive PUREX Raffinate
P. Kaufholz (2017), IV, 173 pp
ISBN: 978-3-95806-284-9

Band / Volume 403
Spatio-Temporal Estimation and Validation of Remotely Sensed Vegetation and Hydrological Fluxes in the Rur Catchment, Germany
M. Ali (2018), xvi, 116 pp
ISBN: 978-3-95806-287-0

Band / Volume 404
Thermomechanical Characterization of Advanced Ceramic Membrane Materials
Y. Zou (2018), xvi, 168 pp
ISBN: 978-3-95806-288-7

Band / Volume 405
Betrachtung der Kristallinitätsentwicklung in mikrokristallinem Dünnschicht-Silizium mit in-situ Raman-Spektroskopie
T. Fink (2018), XI, 166 pp
ISBN: 978-3-95806-289-4

Band / Volume 406
Institute of Energy and Climate Research
IEK-6: Nuclear Waste Management
Report 2015 / 2016
Material Science for Nuclear Waste Management
S. Neumeier, H. Tietze-Jaensch, D. Bosbach (Eds.)
(2018), 221 pp
ISBN: 978-3-95806-293-1

Band / Volume 407
Reduction properties of a model ceria catalyst at the microscopic scale
J. Hackl (2018), VIII, 98 pp
ISBN: 978-3-95806-294-8

Weitere ***Schriften des Verlags im Forschungszentrum Jülich*** unter
http://wwwzb1.fz-juelich.de/verlagextern1/index.asp

Energie & Umwelt / Energy & Environment
Band / Volume 407
ISBN 978-3-95806-294-8

Mitglied der Helmholtz-Gemeinschaft

JÜLICH
Forschungszentrum